A067567

AFAL-TR-79-1028

ADVANCED ARCHIVAL MEMORY

M.S. Adler   C.G. Kirkpatrick
P.V. Gray   H.G. Parks
G.E. Possin

Corporate Research and Development
General Electric Company
Schenectady, New York 12301

March 1979

Sixth Interim Report   January 1, 1978-July 31, 1978

Approved for public release; distribution unlimited.

79 06 29 045

REPORT DOCUMENTATION PAGE		READ INSTRUCTIONS BEFORE COMPLETING FORM
1. REPORT NUMBER AFAL-TR-79-1028	2. GOVT ACCESSION NO.	3. RECIPIENT'S CATALOG NUMBER
4. TITLE (and Subtitle) ADVANCED ARCHIVAL MEMORY		5. TYPE OF REPORT & PERIOD COVERED Technical-Interim Jan. 1, 1978–July 1, 1978
		6. PERFORMING ORG. REPORT NUMBER SRD-78-
7. AUTHOR(s) M.S./Adler, P.V./Gray, C.G./Kirkpatrick, H.G./Parks, G.E./Possin		8. CONTRACT OR GRANT NUMBER(s) F33615-76-C-1322, ARPA Order-3194
9. PERFORMING ORGANIZATION NAME AND ADDRESS Corporate Research and Development General Electric Company Schenectady, New York 12301		10. PROGRAM ELEMENT, PROJECT, TASK AREA & WORK UNIT NUMBERS 31940101 ARPA Order No. 3194-5
11. CONTROLLING OFFICE NAME AND ADDRESS Air Force Avionics Laboratory (AFAL/DHR) Wright Patterson Air Force Base, Ohio 45433		12. REPORT DATE March 1979
		13. NUMBER OF PAGES 143
14. MONITORING AGENCY NAME & ADDRESS(if different from Controlling Office)		15. SECURITY CLASS. (of this report) Unclassified
		15a. DECLASSIFICATION DOWNGRADING SCHEDULE

16. DISTRIBUTION STATEMENT (of this Report)

Approved for public release, distribution unlimited.

17. DISTRIBUTION STATEMENT (of the abstract entered in Block 20, if different from Report)

Interim rept. no. 6, 1 Jan – 1 Jul 78,

18. SUPPLEMENTARY NOTES

*Prepared for Advanced Research Project Agency under
ARPA Order No. 3194.

19. KEY WORDS (Continue on reverse side if necessary and identify by block number)

Computer	Alloy Junction
Memory Systems	Electron Milling
Electron Optics	Thermal Modeling

20. ABSTRACT (Continue on reverse side if necessary and identify by block number)

This report covers the effort for the first eight months of
1978. The contract has been redirected from the ion damage writ-
ing concept to one based on electron beam milling of thin layers
of selenium-arsenic on silicon diode detectors. Background sur-
rounding the redirection can be found in the introduction.
Work in the reporting period has concentrated on evaluating two
all-electron beam storage concepts (alloy junction and electron

406 617   79 06 29 04

20. ABSTRACT (cont.)

beam milling). The electron beam milling approach has been cho-
sen, and an advanced high current electron probe is being pur-
chased for use in evaluating this storage concept.

Accession For

NTIS G.A&I

DDC TAB

Unannounced

Justification

By

Distribution/

Availability

Dist | Available or
      | special

A

PREFACE

The objective of this basic research program is to demonstrate the feasibility of an Advanced Archival Memory System capable of permanent storage of data on solid planar media with 0.1 micron bit spacing and 10 MHz read and write rates. The eventual goal of this program is the construction of low-cost memory systems of 10^{15}-10^{16} bit size with megabit per second data rates and fast access times. The data will be stored on semiconductor target plates by milling holes (bit-site) in a surface layer of a selenium-arsenic mixture using a high current focused electron probe. The bit pattern is read by passing a low current focused electron probe over the target. Where there is a milled hole, the electron beam will penetrate into the silicon, and the resultant current will be amplified by a diode field structure integral to the target. Where there is no hole, no signal will be picked up. The modulation of the current through this diode as the electron beam moves from one bit site to another provides the read signal.

This report covers the effort for the first eight months of 1978. It is the second report in Phase II of this program. Phase I was covered in Reports AFAL-TR-76-213, AFAL-TR-77-35, AFAL-TR-77-157, and AFAL-TR-77-202. In this reporting period, the contract has been redirected from an ion damage writing concept to the electron beam milling approach described above. Background surrounding this redirection can be found in the introduction to this report and in the first Phase II report, AFAL-TR-78-96. The work during this

iii

period has concentrated on evaluating two different all-electron beam storage concepts (alloy junction and beam milling) and choosing a preferred approach for further work. The work has shown that the alloy junction approach is not presently feasible and that the electron beam milling approach looks quite feasible. In place of the ion beam writer that was to be built, a high current electron probe is being purchased for use in evaluating the electron milling storage concept.

iv

TABLE OF CONTENTS

LIST OF ILLUSTRATIONS

LIST OF ILLUSTRATIONS (Cont'd)

LIST OF TABLES

BACKGROUND

The objective of this basic research program is to investigate the feasibility of new storage techniques for $10^{14} - 10^{15}$ bit archival memories using ion and electron beams with semiconductor targets. The current effort (Phase II) deals with 1) the demonstration of the feasibility of writing and reading at data rates of 10 megabits per second with a storage density of 0.1 μm-bit size, 2) the development of the storage medium, and 3) the initiation of system application studies.

Three candidate storage methods have been or are being evaluated. The first of these is the formation of small damaged regions on the surface of silicon diode detectors with a focused ion beam. The other two approaches are based on the use of electron beam heating of metal-silicon target structures. The first of these methods is based on forming surface diodes by heating a thin metallic coating on a silicon target above the silicon-metal eutectic temperature with a finely focused electron beam. The goal is to regrow sufficient silicon as the mixture cools down such that the silicon will then be doped by the metal specie and a microscopic diode is formed. The second approach is either to vaporize or to deform an amorphous metal layer with the electron

1

beam so that the written area will transmit an electron beam when read, while the unwritten area will not. Conceptually this is a very simple idea. The metal layer is essentially a punched card that is read by an electron beam. Unlike the previous two approaches, the silicon is not altered in the writing process and only functions as a detector for the electron beam. The goal for all three approaches is to store and retrieve bits at a 0.1 micrometer-density at a rate of 10 megabits per second.

The program has been redirected during this period of the contract. Originally the contract called for building a focused ion writing optical system and an electron beam reading system. However, these items will not be carried out. In their place a state-of-the-art high current electron writing column will be purchased for use in evaluating the preferred electron beam writing approach. The change in direction in the contract came as a result of determining that the ion writing approach would fail in the stated goal of 0.1 μm-bit density. The following is a brief description of the conclusions in this area. A complete discussion is found in the Phase II Interim Report (July 15-December 31, 1977).

In using writing fluences consistent with the write column design, the resolution appeared to be limited to 0.30 μm. The bit resolution criterion used was equal signals from isolated written and unwritten areas. This is a stringent but correct criterion. Features close to 0.1 μm in size could be easily iden-

2

tified from oscillograph readouts, but simple feature definition
is not adequate basis for a memory technology. Considerable effort
was also spent in determining the factors limiting resolution.
Two resolution limiting effects were found. These include a defect
diffusion phenomenon, in which written defects migrate beyond their
original sites and a beam focusing problem. In the case of the
latter, the focused electron beam used in the experiments has a
highly concentrated component of electron current in the beam
center which determines the ultimate resolution for secondary elec-
tron beam microscopy. It also appears to have had wide tails
which contained sufficient current to produce much poorer overall
resolution for an archival memory.

The work in the current reporting period has concentrated
on evaluating two approaches to an all electron beam based memory,
alloy junction and electron machining. Two additional tasks are
also being carried out. The first is a read systems study to an-
swer questions regarding the size of the bit field that can be
electronically accessed and the compatibility of reading and writ-
ing with the same column. The second is an ion source test that
will complete the design and specifications of the ion column be-
gun earlier in Phase II. In the case of the latter, the ion sources
obtained from the Oregon Graduate Center are being tested for angu-
lar brightness and energy spread using a test stand now completed.

Both approaches to the memory technology use below board
silicon diode detection for readout. The alloy junction work

3

is a continuation of the work in this area started in Phase I. The electron machining approach builds on work done in the Electronics Laboratory of the General Electric Company in 1968-1971 and has made maximum use of the results achieved. The efforts at the Electronics Laboratory failed due to problems with target fabrication, with the secondary readout used, and with controlling and getting sufficient current from the electron writing column. To achieve sufficient readout, the amorphous metal layer was made from a triple alloy system of selenium, arsenic, and gold. It was difficult to control the composition of these targets, and the resolution achieved was quite variable. In addition, the beam power available at the time was not sufficient to vaporize the selenium and the writing was based on melting the selenium and leaving a depression.

Now over six years of work on diode detection in the BEAMOS project and Phase I and II of this contract at General Electric Corporate Research and Development offer promise of eliminating the reading difficulties. In addition, a great deal of progress has been made in both controlling field emission electron sources and in obtaining higher overall currents. An order of magnitude of improvement has been made in the latter since 1969. As a result, it is now possible to write by vaporizing the film. High signal-to-noise ratios are achieved because of the effective machining and the inherent amplification occurring with diode readout. The target manufacture is basically simple because only a selenium arsenic mixture is used in the film and the film properties are not sensitive to the detailed composition.

4

CURRENT STATUS

An initial series of experiements on the electron beam milling of selenium arsenic target structures has been performed and analyzed. A theory has been developed which correctly explains the experimental results and has been used to predict the necessary conditions of beam current, beam voltage, spot size, and film thickness to achieve 0.1 μm-bit densities and a 10 MHz writing rate. These conditions have been shown to be consistent with the specifications for an advanced field emission electron column being purchased from ETEC Corporation. The decision to purchase this column was made after a careful build or buy studying process. Ultimately the decision was made because the predicted performance of the ETEC microscope comes very close to the optimum achievable.

Work on the alloy junction writing approach has also progressed a great deal in this reporting period. A detailed steady state model of the alloying junction writing process has been developed. The model can be used to choose the alloy system which will produce the largest writing efficiency and also to determine the conditions of temperature and metal thickness necessary to achieve the writing. The model was then applied to the specific cases of the gold-silicon and the aluminum-silicon alloy systems. In addition, a series of steady state alloying experiments have been carried out. These experiments had the desired result of confirming the correctness of the alloying model but also clearly identified problems with the alloy junction approach. One significant

5

problem is that temperature excursions of over 300 $^{\circ}$C have been theoretically and experimentally shown to be necessary for adequate writing, but the modeling of the electron beam heating effects show that excursions will be limited to under 75 $^{\circ}$C for both preferred alloy systems (Al-Si and Au—Si). These temperature excursions were calculated on the basis of 0.1 μA current in a 0.1 μm-spot. This is the upper end of the expected performance from the state-of-the-art electron column being purchased from ETEC Corporation and will not be materially improved upon in the foreseeable future. In addition to the difficulty in reaching the required temperature rises a problem of non-wetting of the metal specie on the silicon surface was discovered. When heated, the metal specie has a tendency to move away from the heat source rather than form an alloy. There is also a tendency for the metal to condense on surface faults on the silicon target.

The electron milling approach has been chosen as the preferred approach. This decision was arrived at because of the difficulties with the alloy junction, on one hand, and the successful results and optimistic predictions for the electron milling approach, on the other hand. Work will continue on furthering our understanding of the writing mechanism and in experimenting with and obtaining good quality selenium-arsenic films. Upon arrival of the ETEC column, a program will be started to demonstrate the storage capabilities of electron milling of selenium films. This will include achievable bit density and writing rate.

Construction of the ion source test stand has been completed and it is now fully operational. Energy spread and angular brightness data are being taken on the field ion sources from the Oregon Graduate Center. Results of these measurements will be included in the final report under the current contract. Work on the read systems study to investigate the limits on the size of directly addressable data blocks and on the use of matrix lens technology will be started in the last quarter of calendar 1978.

REPORT CONTENTS

In Section II of the report the steady state alloying model is presented in detail. Specific examples of the Al-Si and Au–Si alloy systems are presented. Experimental data on the corroboration of the model using an Au-Si alloy junction are also presented. Section III discusses the results of isothermal studies of the alloying process. The problems of wetting the silicon surface by the metal specie during alloying are demonstrated and discussed.

In Section IV of this report the results of the selenium-arsenic writing experiments and the theoretical analysis are presented in detail. A computer program has been developed to calculate transient heating of target structures in two dimensions with up to three distinct layers. This model is used in the electron milling and the alloy junction analysis and is fully explained in Section V of the report. The program and a user's manual are presented in the Appendix. Analysis of the ETEC microscope is

7

presented in Section VI where the predicted performance of the
electron optical column is shown to agree well with the published
specifications and data. The phenomena limiting performance are
also discussed.

INTRODUCTION

During this reporting period consideration was given to the
alloy process for binary phase systems. Based on a general binary
system phase diagram, a model was developed that explains the alloy
process from a steady state point of view. Use of the model has
aided in understanding the requirements and conditions for a good
binary archival target system. The model has also been useful
for choosing laser writing experiments. The development and use
of the alloy model during this reporting period are discussed in
this section.

THE ALLOY MODEL

Many of the metals and dopants found in silicon semiconductor
processing exhibit a binary phase with silicon. The phase dia-
gram for these materials is of the type shown in either Figure 1a

or Figure 1b. In Figure 1a the system shows a eutectic temperature (T_E) that is depressed from the melting points of either constituent and a reasonable weight percentage (W_E) of silicon in the eutectic melt. Typical materials showing this type of phase diagram are Al, Au, and Ag; and are representative of metals with moderate melting temperatures. Figure 1b shows a system where the melting point of the material interacting with silicon and the eutectic temperature are almost the same. Of *further note* for these systems the weight percent of silicon in the eutectic melt is extremely small. Materials exhibiting this behavior are typically of the low melting point metals such as Ga and In.

The alloy process can be explained by referring to the phase diagrams of Figures 1a and 1b and the material cross section of Figure 2. This figure shows a silicon substrate with a thin metal layer and a small alloy region presumably formed by heating the material at that point with localized radiation *such as an electron or laser beam*. For purpose of explanation, a metal over-layer is assumed because binary phase diagrams seem to be more typical of metal-silicon systems. However, it is acknowledged that metalloids (e.g. Sb) can have binary phase with silicon and other conventional dopants such as As, P, and B show a binary type phase over a portion of their phase diagrams. The following discussion and the resulting model apply equally well to these systems.

Referring now to the alloy region of Figure 2, the region *was formed* by raising the local temperature to a maximum value

9
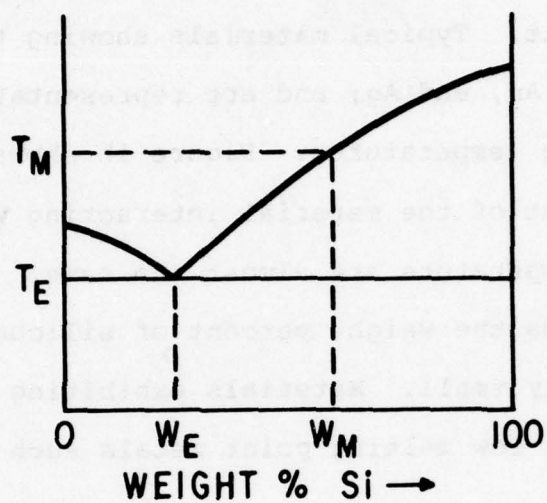
(1a)
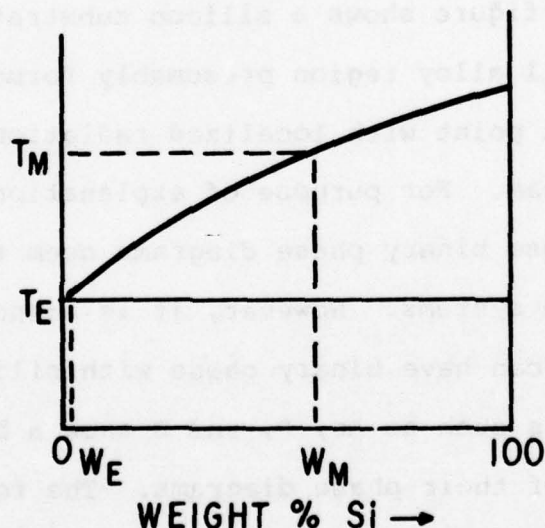
(1b)

Figure 1.   Typical Binary Phase Diagrams for Si
and materials Used in Si Processing

T_M which is greater than the eutectic temperature as indicated on Figure 1. It is assumed that this temperature is maintained and relaxed at rates so that equilibrium conditions are met. The resulting alloy structure that is formed consists of a regrown crystal region of thickness, t_R, and a homogeneous eutectic region
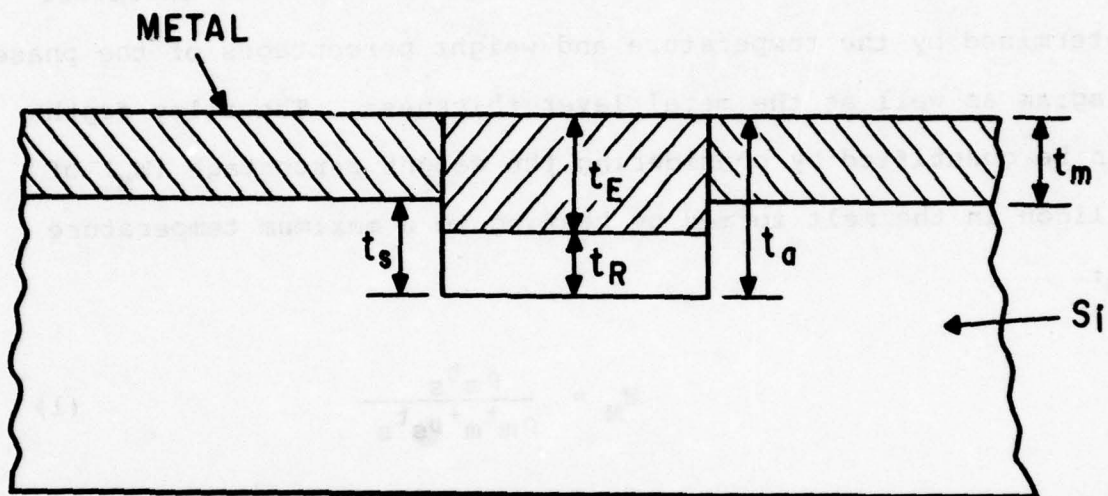
Figure 2. Localized Alloy Region for a Thin Metal Film on Silicon System

of thickness, t_E. The reason that the regrown crystal forms is that the solubility of silicon in the alloy melt is reduced as the temperature is lowered from T_M (see Figure 1). With a finite thickness of metal present, the melt region must reduce in size as the temperature is lowered, thus leaving a regrown crystal. These statements will be quantified below. The regrown crystal region is doped with metal according to the solid solubility of the metal in silicon at the temperature at which the region passes through the solidus. Solid solubilities [1] as a function of temperature of some of the typical dopants used in silicon semiconductor processing are shown in Figure 3. As indicated on the

11

phase diagram of Figure 1 the alloying process follows the phase diagram on the silicon rich side of the eutectic since there is an overabundant supply of silicon in comparison to the thin metal layer.

The depths to which the alloy regions reach are therefore determined by the temperature and weight percentages of the phase diagram as well as the metal layer thickness. The alloy depths can be quantified by considering the weight percentage (W_M) of silicon in the melt formed by heating to a maximum temperature T_M:

$$W_M = \frac{\rho_s t_s}{\rho_m t_m + \rho_s t_s} \qquad (1)$$

where

ρ_s, ρ_m = silicon and metal mass density respectively

t_m, t_s = metal layer thickness and affected semiconductor depth respectively (cf Fig. 2)

Rearranging Eq. 1 the ratio of the depth of affected semiconductor to metal layer thickness is:

$$\frac{t_s}{t_m} = \frac{W_M}{1 - W_M} \cdot \frac{\rho_m}{\rho_s} \qquad (2)$$

12

Hence the total affected depth due to the alloying process is:

$$\frac{t_a}{t_m} = 1 + \frac{W_M}{1 - W_M} \cdot \frac{\rho_m}{\rho_s} \tag{3}$$

The eutectic thickness at the eutectic temperature is determined in the same manner in accordance with the weight percent at the eutectic W_E as:

$$\frac{t_E}{t_m} = 1 + \frac{W_E}{1 - W_E} \cdot \frac{\rho_m}{\rho_s} \tag{4}$$

Therefore the regrown semiconductor is just the difference between Eqs. 3 and 4:

$$\frac{t_R}{t_m} = \frac{t_a - t_E}{t_m} = \left[\frac{W_M}{1 - W_M} - \frac{W_E}{1 - W_E} \quad \frac{\rho_m}{\rho_s} \right] \tag{5}$$

Since W_M is greater than W_E this is always greater than zero. These equations constitute the alloy model and allow calculation of the various affected depths under the given alloying conditions. Another parameter of interest is the density of the eutectic alloy. Assuming a uniform and homogeneous eutectic region conservation of mass gives the alloy density as:

$$\rho_{alloy} = \frac{1}{(1 - W_E)} \cdot \left[\frac{\rho_m}{1 + \frac{W_E}{1 - W_E} \cdot \frac{\rho_m}{\rho_s}} \right] \tag{6}$$

13
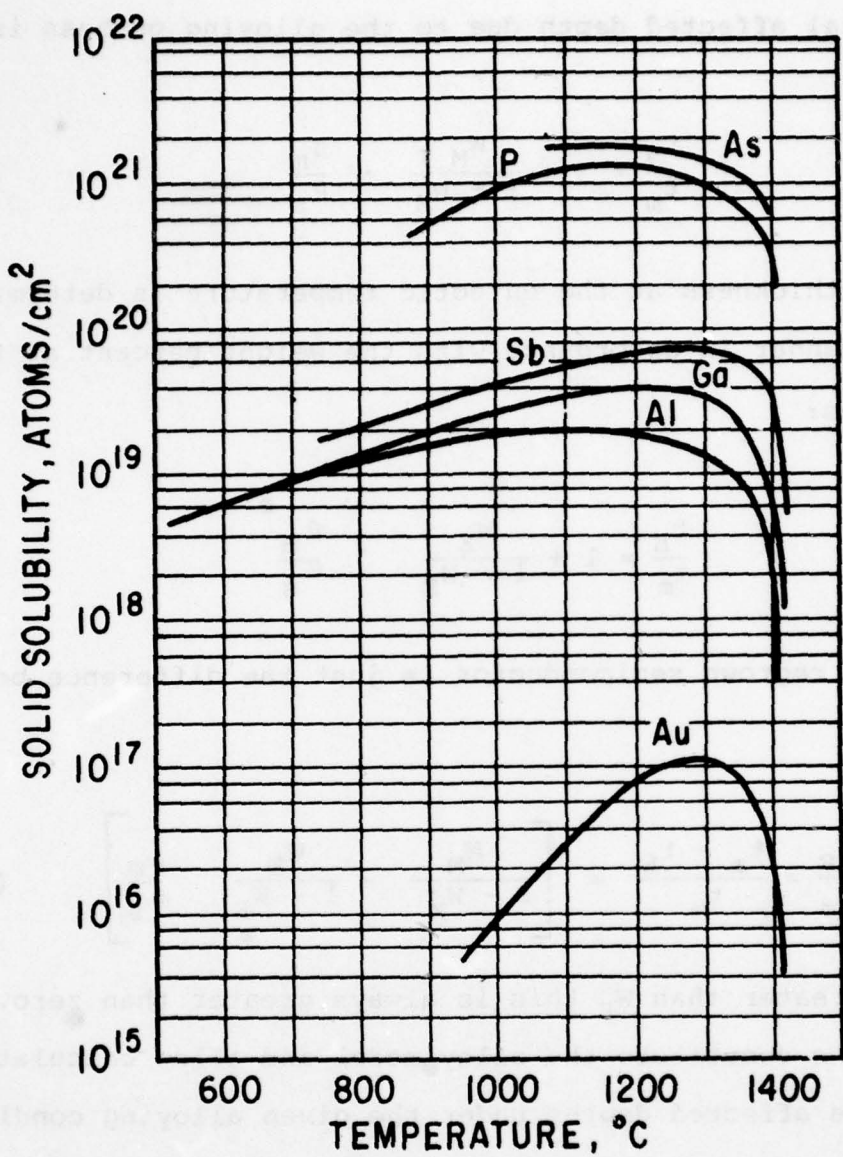
Figure 3. Solid Solubilities of Impurities
in Si (adapted from Ghandi[1])

USE OF THE ALLOY MODEL

The alloy model has been useful in considering the types of
metal semiconductor systems required for an alloy junction target.
Based on use of the model, earlier writing experiments are better

14

understood enabling us to revamp our thinking on certain target materials and allowing new experiments to be outlined.

One of the first concepts for the alloy junction target [2] was to use a gold or silver metal layer on a silicon substrate. It was recognized that these materials produced deep energy levels in the silicon band gap and therefore would not produce a conventional diode as with shallow impurities. Nevertheless, it was felt that because of the large weight percent of silicon in the eutectic sufficient penetration of the eutectic into the semiconductor would occur to produce readout modulation. Initial laser writing experiments [3] verified that writing did occur for a gold silicon system, however, readout modulation was poor when read with the metal layer on. At the time of the writing experiments it seemed that the poor modulation was a result of too thick a gold film (1000 Å) being used in the experiment as well as the grain structure thus masking the effect of reading the alloyed region.

Through the use of the alloy model it is now believed that there is a fundamental problem with systems such as Au-Si and Ag-Si that preclude their use as alloy junction targets. Based on the solid solubility data of Figure 3, it is seen that gold has an extremely small solid solubility in silicon over the whole temperature range. What this means in terms of the target is that, regardless of how high above the eutectic temperature the system is raised, there will not be enough gold introduced in the regrowth region to affect the hole capture rate. Therefore, the resulting

15

modulation for a target such as this can only come from the higher electron stopping of the eutectic region relative to the metal over layer. By consideration of the model equations this can be shown to produce relatively weak modulation. For a constant beam energy (as in the case of the read beam) the mass range of electron penetration is constant [4] and, therefore:

$$\rho R = \text{const} = C \tag{7}$$

where ρ is the mass density and R is the electron range.

Hence for the read beam scanning just the metal layer, the range to metal layer ratio is given by:

$$\frac{R_m}{t_m} = \frac{C}{\rho_m t_m} \tag{8}$$

Now from Eqs. 6 and 4 it is seen that the factor that increases the eutectic thickness over the metal layer thickness shows up as a reduction in the alloy density and therefore the range to eutectic layer thickness is:

$$\frac{R_E}{t_E} = (1 - W_E) \ \frac{C}{\rho_m t_m} \tag{9}$$

or in view of Eq. 8

$$\frac{R_E}{t_E} = (1 - W_E) \ \frac{R_m}{T_m} \tag{10}$$

16

Therefore the reduction in modulation due to the eutectic is only $(1 - W_E)$ which is insignificant unless W_E becomes greater than 20% or so.

In view of this result it is now believed that Au (W_E = 6%) and Ag (W_E = 3%) would only be useful if they were loaded with a dopant material such as Ga or Sb. This would allow the regrowth region to be doped to the opposite polarity of the top layer of the planar diode substrate thus forming a surface diode with its depletion field to enhance the dead layer (or hole capture) in the written area. The reason gold might be used as a carrier for the Ga or Sb rather than just using the dopants themselves can also be understood from the model and the phase diagrams. Figure 4 shows the phase diagrams for Ga - Si and Au - Si. The Ga - Si system not only has a very low eutectic temperature (≈30 ^{o}C), but also the slope of the phase diagram is very steep. This means very high temperatures must be reached in order to achieve a deep regrown region. In contrast the Au - Si system has a moderately high eutectic temperature (370 ^{o}C) with a much lower slope of the phase diagram above the eutectic. The net result is that much deeper doped regions can be achieved at lower temperatures using gold as a carrier for the low solubility dopants than by using the dopants themselves. This is illustrated in Figure 5 which shows the regrowth to metal layer ratio, t_R/t_m Eq. 5, as a function of temperature.

Experimental data are available that not only verifies the use of gold as a dopant carrier but also verifies the alloy model.

17
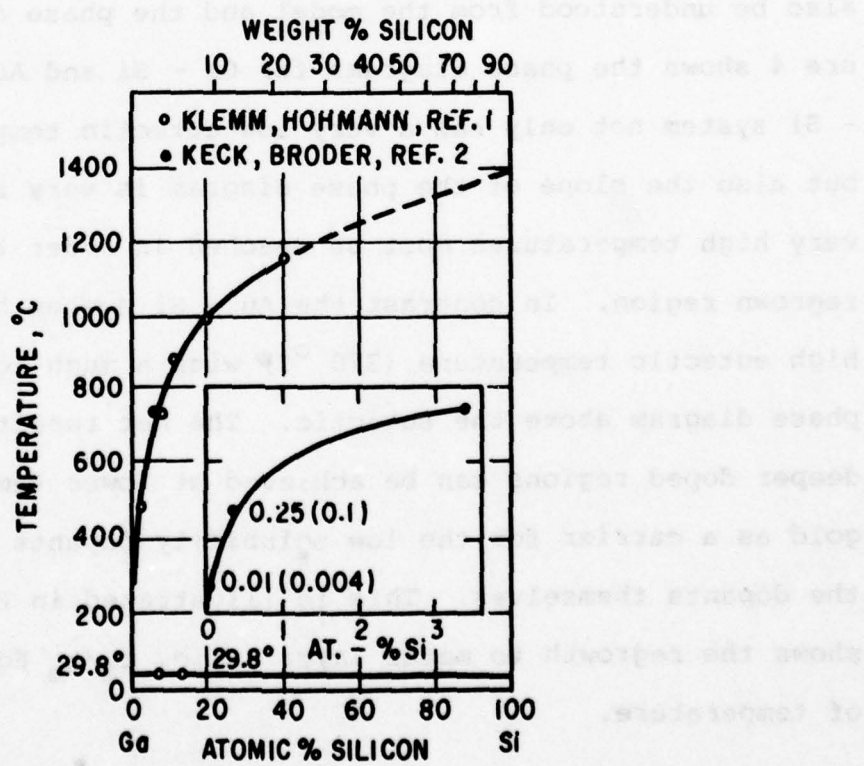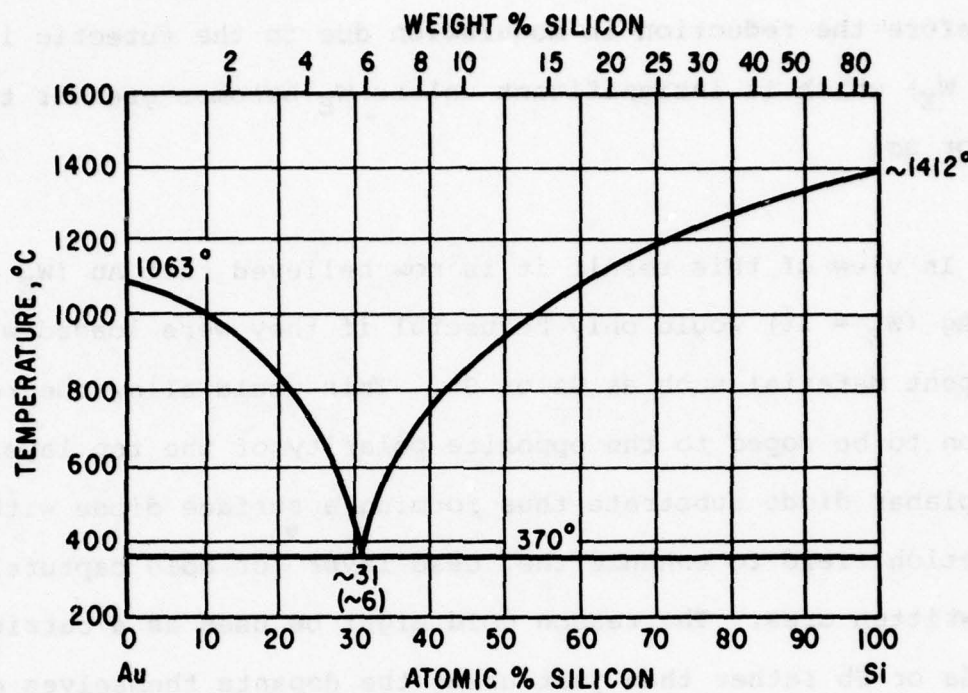
Figure 4. The Gold-Silicon and Gallium Silicon Systems
(From M. Hansen and A. Anderko, Constitution
of Binary Alloys, McGraw Hill, New York, 1958)
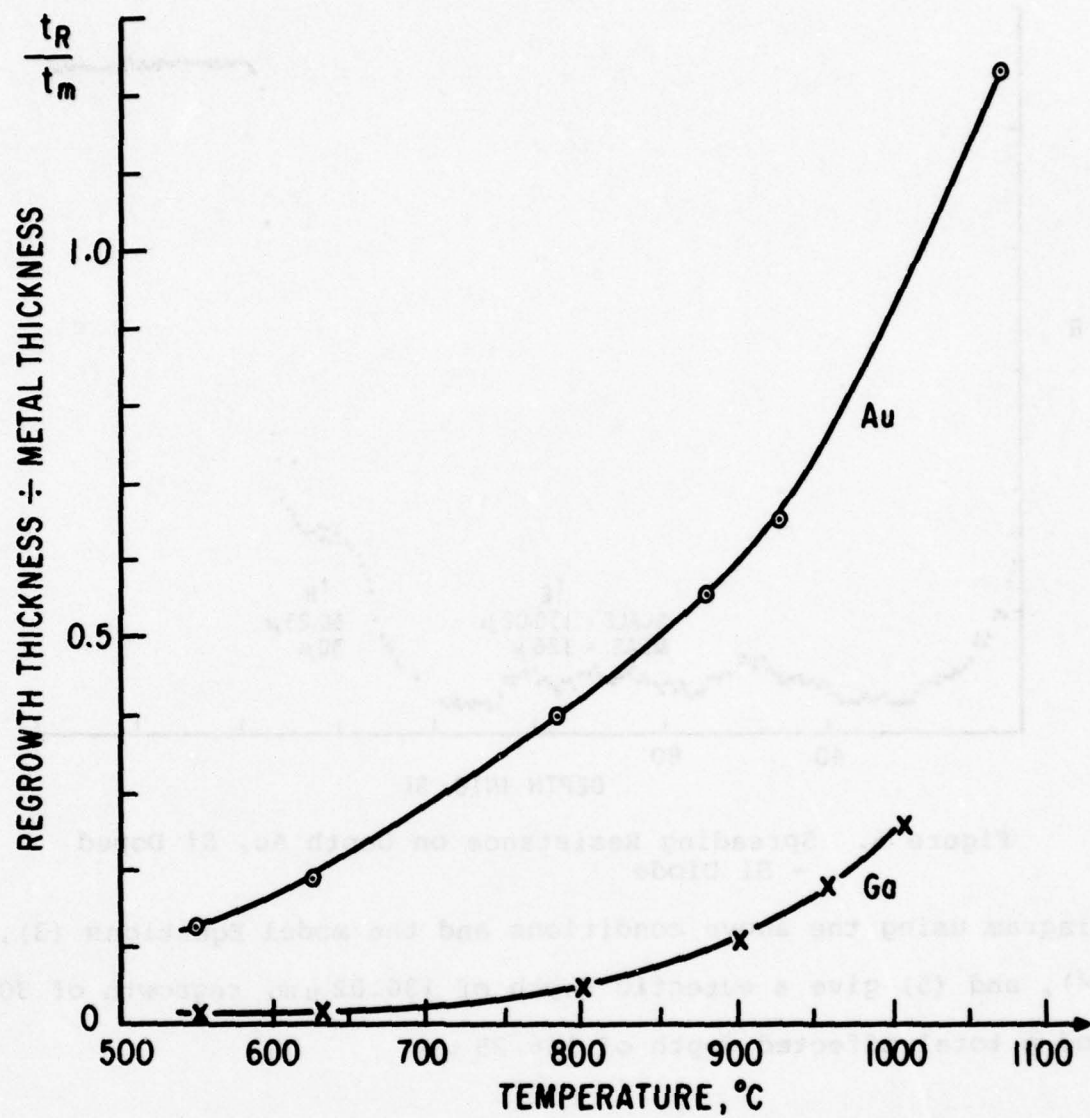
Figure 5. Crystal Regrowth for Alloying Above
the Eutectic for Au-Si and Ga-Si

Figure 6 shows spreading resistance measurements as a function
of depth obtained from a diode formed under steady state conditions
using gold as a carrier for antimony dopant. The conditions were
3.5 mils of gold with 1% antimony held at a temperature of 750 $^{\circ}$C
for one hour. Based on this resistance curve a eutectic depth
of 126 μm and a regrowth of 30 μm is indicated giving a total af-
fected depth of 156 μm. Calculations based on the Au – Si phase

19
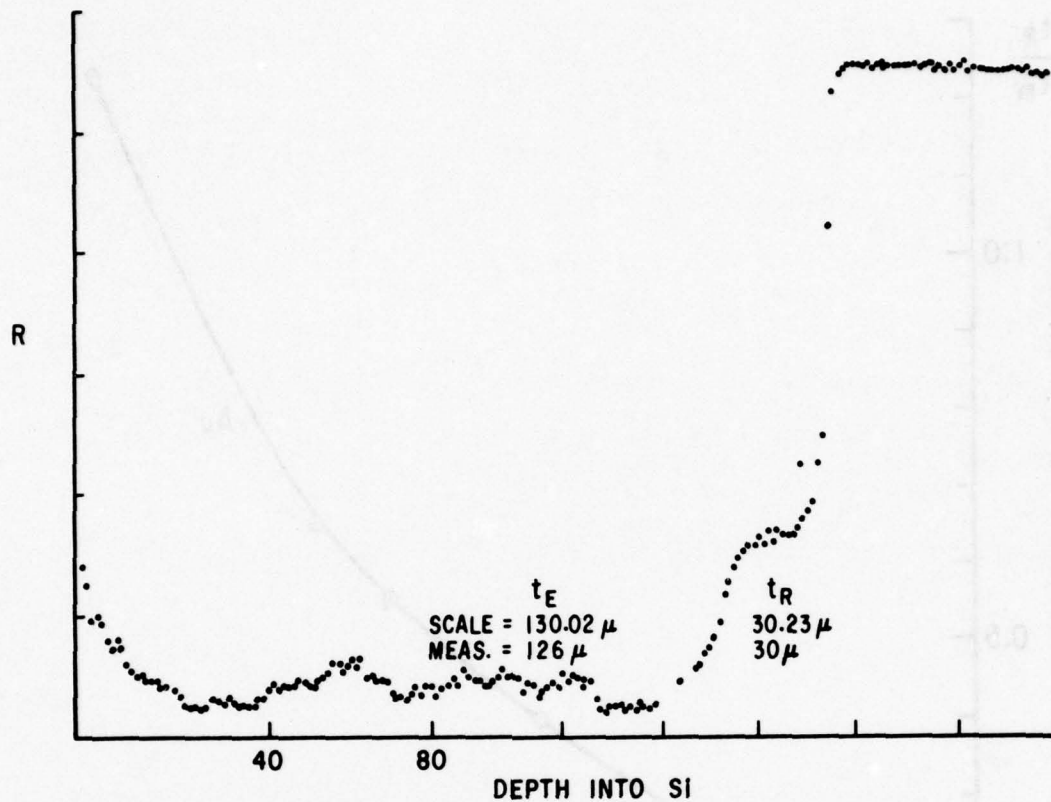
Figure 6. Spreading Resistance on Depth Au, Si Doped
- Si Diode

diagram using the above conditions and the model Equations (3),
(4), and (5) give a eutectic depth of 136.02 μm, regrowth of 30.23 μm
and a total affected depth of 166.25 μm.

The model has been used as an aid in setting up experiments
to determine the nature of the writing achieved under short pulse
conditions. Based on the excellent correlation of the model calcu-
lations and the Au-Sb-Si diode, we know that good abrupt junction
diodes can be formed under steady state conditions. We also know
from previous laser writing experiments that good, strong writing
effects can be obtained with Al-Si at temperatures below the melt-
ing point of aluminum and with single laser pulses of 150 μm sec

20

pulse duration. Furthermore from thermal model considerations
we know that steady state temperatures can be achieved in time
of the order on nanoseconds. The remaining question is whether
or not the alloy process can form good junctions within the short
pulse times. Using the alloy model, we have calculated the ex-
pected hole capture depth based on two limiting cases: (1) a diode
has been formed and the capture depth is the attendant depletion
width, and (2) no diode is formed and the captor depth is simply
the depth at the regrown crystal region. In the case of the latter,
it is assumed that the carrier lifetime has been killed in the
regrown region.

Alloy junction diodes are usually modeled as an abrupt junc-
tion [5] with a carrier concentration and space charge region as
shown in Figure 7. For this model the depletion fields in the
n and p materials with no external bias are given by the equations:

$$X_n = \left[\frac{2\varepsilon\phi_o N_A}{q \ N_D(N_D + N_A)} \right]^{1/2} \tag{11}$$

$$X_p = \left[\frac{2\varepsilon\phi_o N_D}{q \ N_A(N_D + N_A)} \right]^{1/2} \tag{12}$$

where ϕ_o is the contact potential:

$$\phi_o = \frac{kT}{q} \ \ln \ \frac{N_D N_A}{n_i^2} \tag{13}$$

21

P TYPE n TYPE

N_D

N_A

CARRIER CONCENTRATION

+ + + + + +
X_P + + + + + +
X_N
= =

SPACE CHARGE REGION
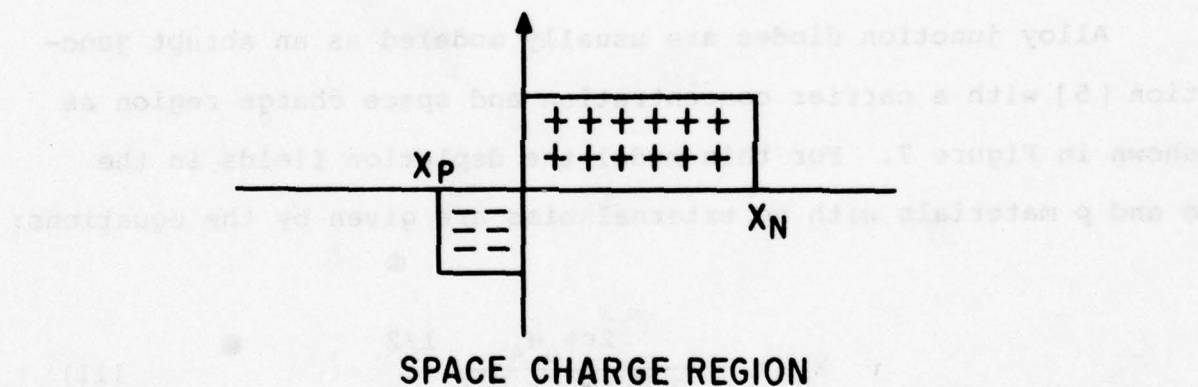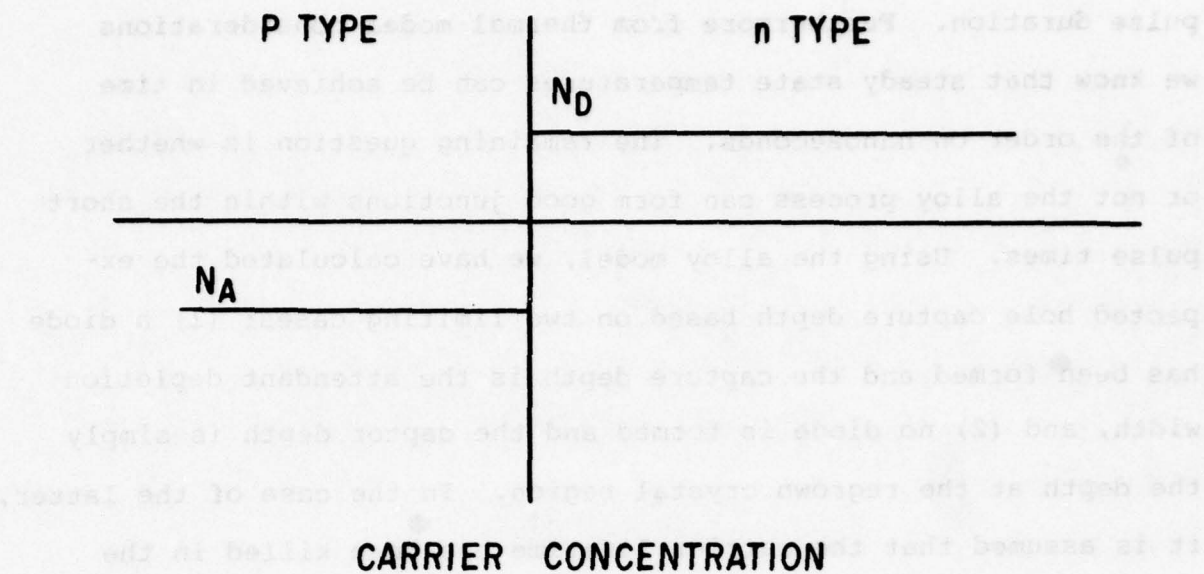
Figure 7. Carrier Concentration and Space Charge Region
for the One-Dimensional Abrupt Junction
Diode Model

In these equations:

X_n X_p = depletion field depth in n and p materials

N_A, N_D = acceptor and donor concentrations in the

p and n material respectively

n_i = intrinsic carrier concentration

ε = permittivity of the semiconductor

22

q   =   electronic charge

k   =   Boltzmann constant

T   =   absolute temperature

Using this diode model, the aluminum silicon phase diagram of
Figure 8 and the alloy model, the resulting dead layer thickness
was calculated as a function of temperature for various metal
film thickness as shown in Figure 9. For these calculations,
n on p planar diodes with constant n layer doping of $10^{16}/cm^3$
were assumed. For temperatures just above the eutectic the regrown
layer of the alloy process which provides the p doped portion
of the surface is less than the depletion field requirement of
Eq. 12. Under these conditions the p depletion region is just
equal to the regrown crystal region doped at concentration N_A de-
termined from the solid solubility data of Figure 3 at the spec-
ified temperature resulting in an n layer penetration of the de-
pletion field given by

$$X_n = \frac{N_A}{N_D} \, t_R$$

However, as the alloy temperature is raised, the regrown region
becomes thicker than X_p of Eq. 12 and the dead layer nearly satu-
rates with a slight slope from that point on. This occurs in the
range of 585° to 600 ^{o}C for the metal thicknesses assumed. This
saturation occurs because once the regrown crystal region exceeds
X_p and the full depletion width is formed, further increases in
the dead layer come from the increase in penetration of the eutectic

23

WEIGHT % SILICON

10   20   30   40   50   60   70   80   90

WEIGHT % Si
0.5   1.0   1.5   2.0

700

600   577°
(Al)   1.59
500   (1.56)

400

0.16 (0.17)
300

(Al) + Si
200

100

0

0.5   1.0   1.5
ATOMIC % Si

800

700

660°
600   577°

(Al) 11.3
500   (11.7)

400

0   10   20   30   40   50   60   70   80   90   100
Al   ATOMIC % SILICON   Si

TEMPERATURE, °C

1500   1412°
1400
1300
1200
1100
1000
900
Si→
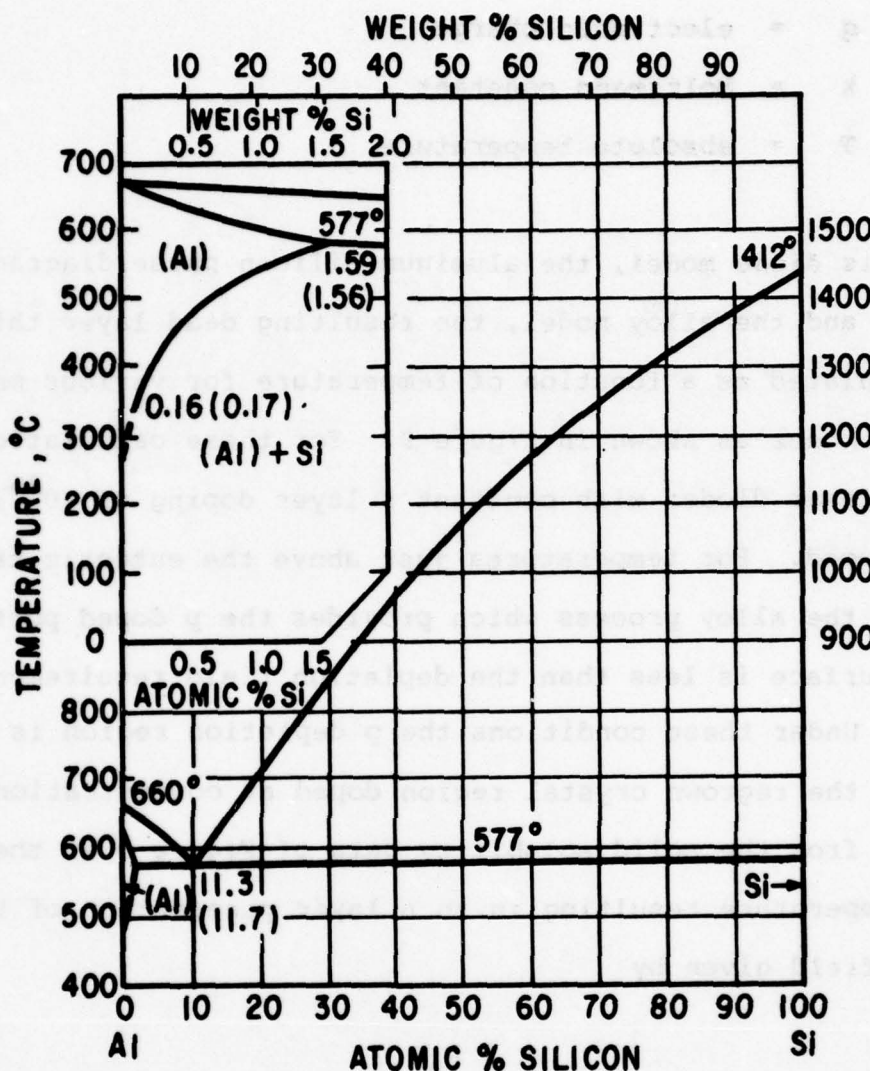
Figure 8. The Aluminum-Silicon System. (From M. Hansen,
and A. Anderko, Constitution of Binary Alloys,
McGraw-Hill, New York, 1958.)

and regrown regions with increasing temperatures. This is a slowly
increasing function of temperature because the regrown depth is
smaller than the depletion depth and increases in the regrown re-
gion come only from the slow increase in the silicon solubility
in the Al-Si eutectic with temperature.
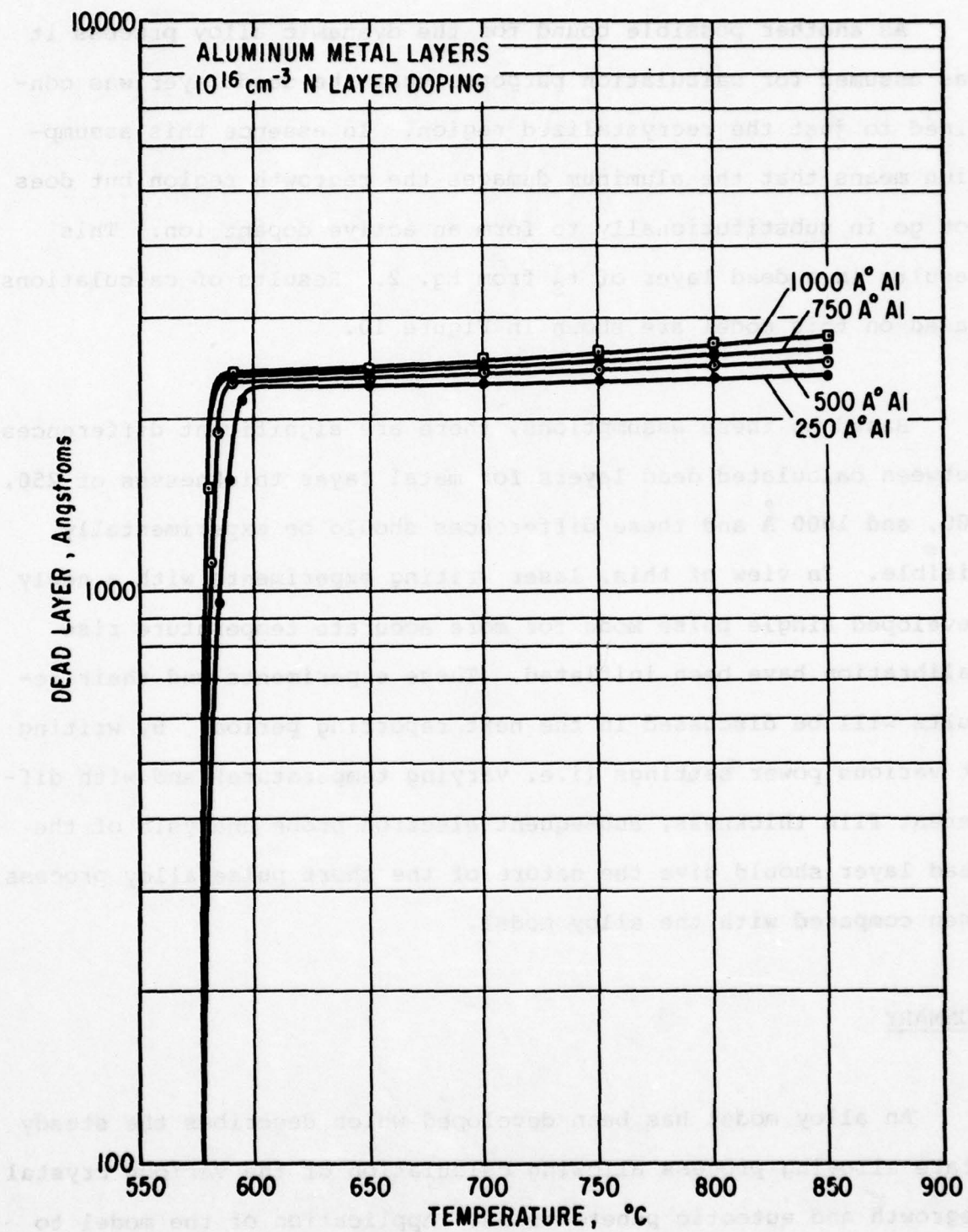
Figure 9. Dead Layer Based on Diode Formation
Aluminum Metal Layers 10^{16}cm^{-3}
N Layer Doping

As another possible bound for the dyanamic alloy process it was assumed for calculation purposes that the dead layer was confined to just the recrystalized region. In essence this assumption means that the aluminum damages the regrowth region but does not go in substitutionally to form an active dopant ion. This results in a dead layer of t_S from Eq. 2. Results of calculations based on this model are shown in Figure 10.

Based on these assumptions, there are significant differences between calculated dead layers for metal layer thicknesses of 250, 500, and 1000 $\overset{\circ}{A}$ and these differences should be experimentally visible. In view of this, laser writing experiments with a newly developed single pulse mode for more accurate temperature rise calibration have been initiated. These experiments and their results will be discussed in the next reporting period. By writing at various power settings (i.e. varying temperature) and with different film thickness, subsequent electron probe analysis of the dead layer should give the nature of the short pulse alloy process when compared with the alloy model.

SUMMARY

An alloy model has been developed which describes the steady state alloying process allowing calculation of the various crystal regrowth and eutectic penetrations. Application of the model to an Au-Sb-Si diode verifies its correctness. The model has been used to aid in the understanding of basic metal semiconductor re-
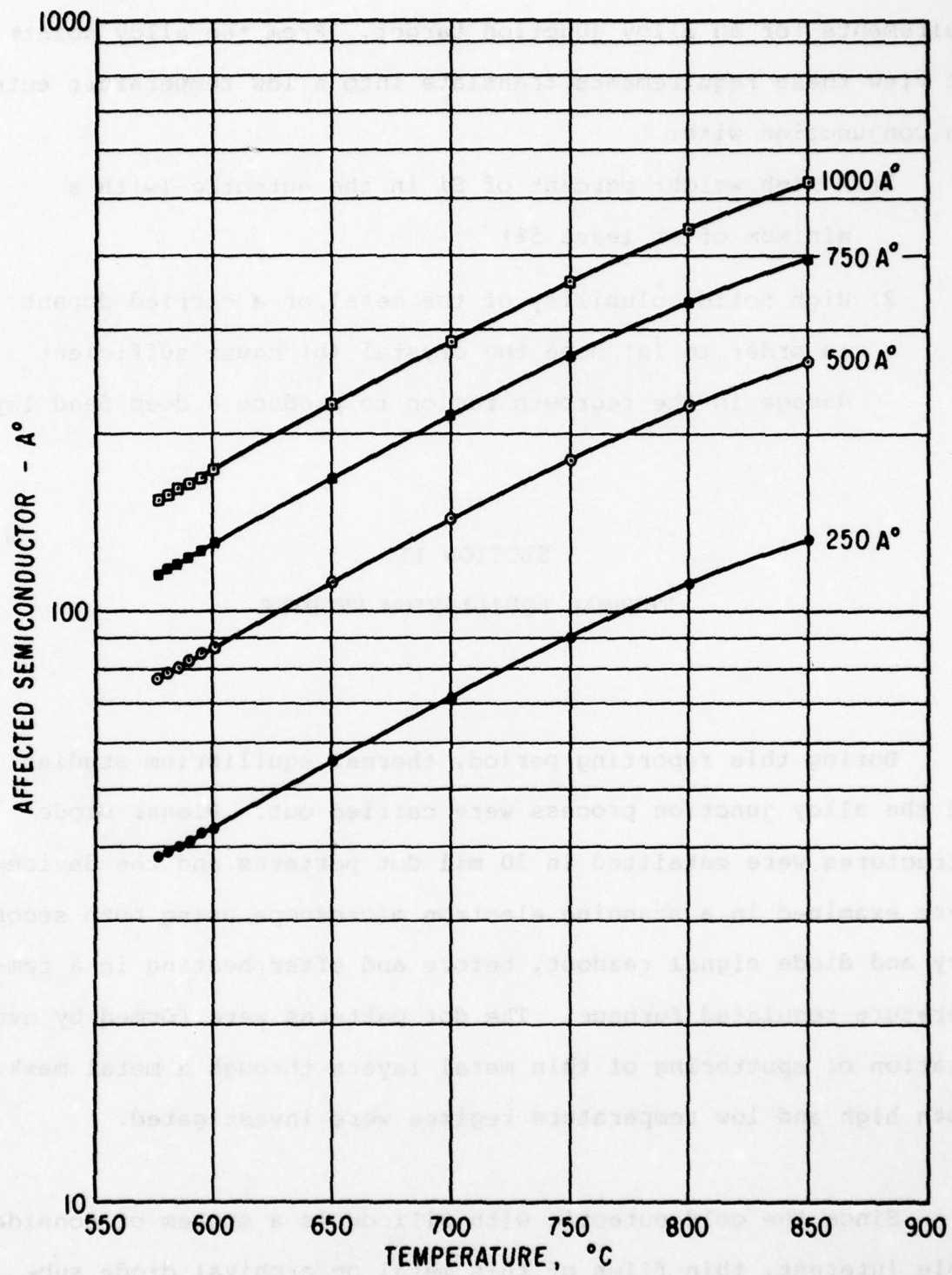
Figure 10. Dead Layer Based on Affected Semiconductor Depth, t_s, Aluminum Metal Layers $10^{16}cm^{-3}$ N Layer Doping

27

quirements for an alloy junction target. From the alloy point
of view these requirements translate into a low temperature eutectic
in conjunction with:

1) A high weight percent of Si in the eutectic (with a
   minimum of at least 5%)

2) High solid solubility of the metal or a carried dopant
   in order to (a) dope the crystal (b) cause sufficient
   damage in the regrowth region to produce a deep dead layer.

SECTION III
THERMAL EQUILIBRIUM STUDIES

During this reporting period, thermal equilibrium studies
of the alloy junction process were carried out. Planar diode
structures were metalized in 30 mil dot patterns and the devices
were examined in a scanning electron microscope using both second-
ary and diode signal readout, before and after heating in a tem-
perature regulated furnace. The dot patterns were formed by evap-
oration or sputtering of thin metal layers through a metal mask.
Both high and low temperature regimes were investigated.

Since the gold eutectic with silicon is a system of consider-
able interest, thin films of this metal on archival diode sub-
strates were studied. Figure 11 illustrates a typical experiment
consisting of several dot arrays produced by sputter depositing

28
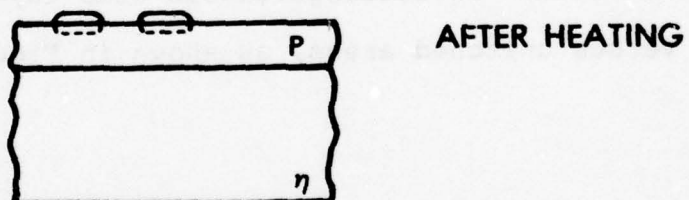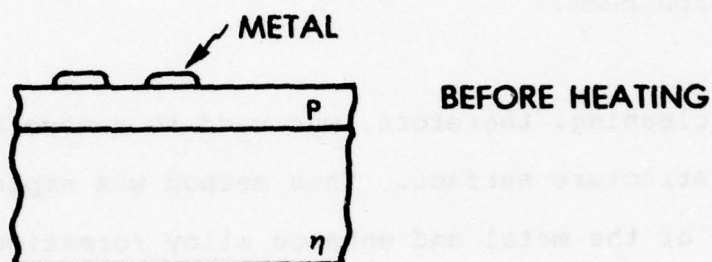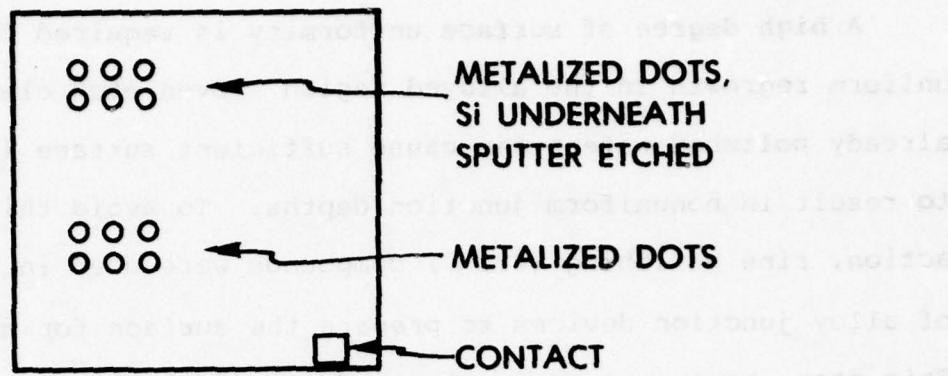
Figure 11. Illustration of Typical Thermal Equilibrium Alloy Junction Experiment, Consisting of Small Metalized Dot Arrays Deposited on Sputter Etched and Unetched Regions of a Planar Diode Device

200 Å of gold on PAR 1A target. PAR 1A targets were produced by two separate boron implants into an n-type substrate to form a p⁺pn structure. In these experiments, all substrate material was <111>, since the solid-liquid interface lies in this plane.

A high degree of surface uniformity is required for thin, uniform regrowth in the alloyed region. Even etch cleaning of already polished wafers can cause sufficient surface irregularity to result in nonuniform junction depths. To avoid this spiking action, fine polishing (0.1μ) compounds were used in the production of alloy junction devices to prepare the surface for metalization. This step, however, can result in damage depths $\approx 1\mu$, which would create a "dead layer" perceptible during readout of the device with an electron beam.

Sputter cleaning, therefore, was used to remove any native oxide on the structure surface. This method was employed to improve wetting of the metal and enhance alloy formation as well. Both sputter etched and unetched areas were metalized for comparison. Diode readout measurements were taken for both types of areas and the bar diode. No distinguishable dead layer was observed for the etched versus unetched areas, as shown in Figures 12 and 13.

Sample heating was performed in a furnace in a quartz boat located in the flat zone, surrounded by argon ambient. Target structures were maintained at temperature 5 minutes before removal. For sample PAR 1A, the low temperature run was performed at 375 $^{\circ}$C, 5 $^{\circ}$C above the eutectic temperature. Figures 12 and 13 compare the diode signal before and after baking for the metalized dot arrays, and Figure 14 indicates the signal before and after heating in the untreated diode region. Little evidence for alloying was observed.

30
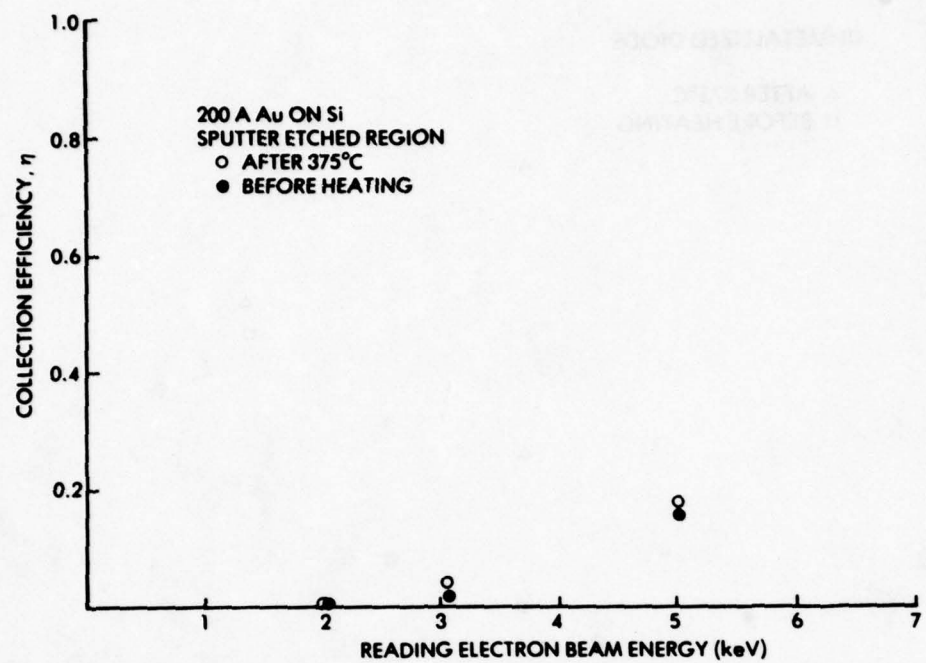
Figure 12. Collection Efficiency from p⁺pn Planar Diode Device Before and After 375 °C Bake, in a Region Metalized with 200 Å of Gold, Sputter Cleaned Before Deposition
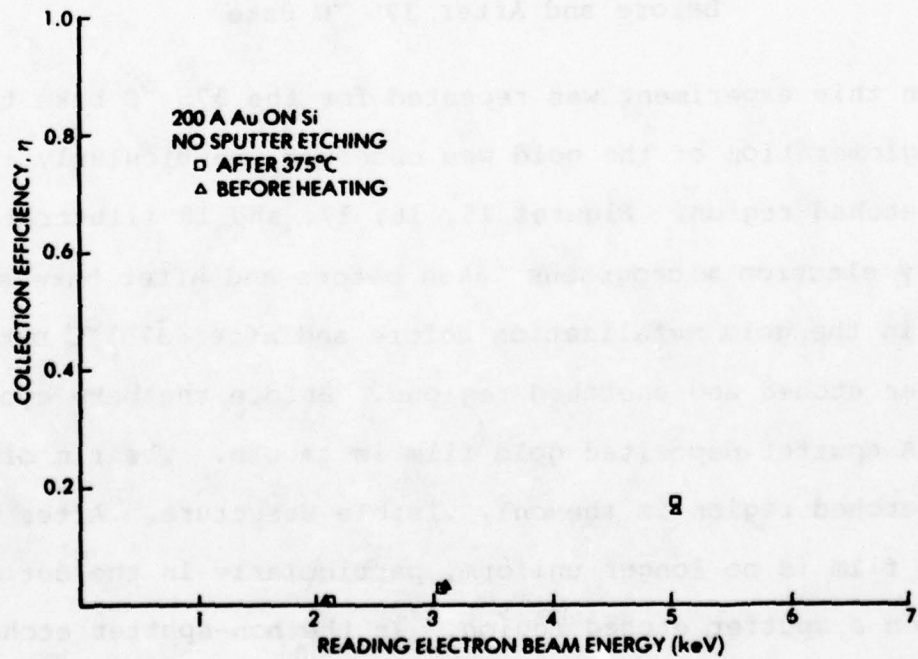
Figure 13. Collection Efficiency from p⁺pn Diode Device Before and After 375 °C Bake, in a Region Metalized with 200 A of Gold.

31

UNMETALLIZED DIODE

△ AFTER 375°C
□ BEFORE HEATING

COLLECTION EFFICIENCY, η

READING ELECTRON BEAM ENERGY (keV)
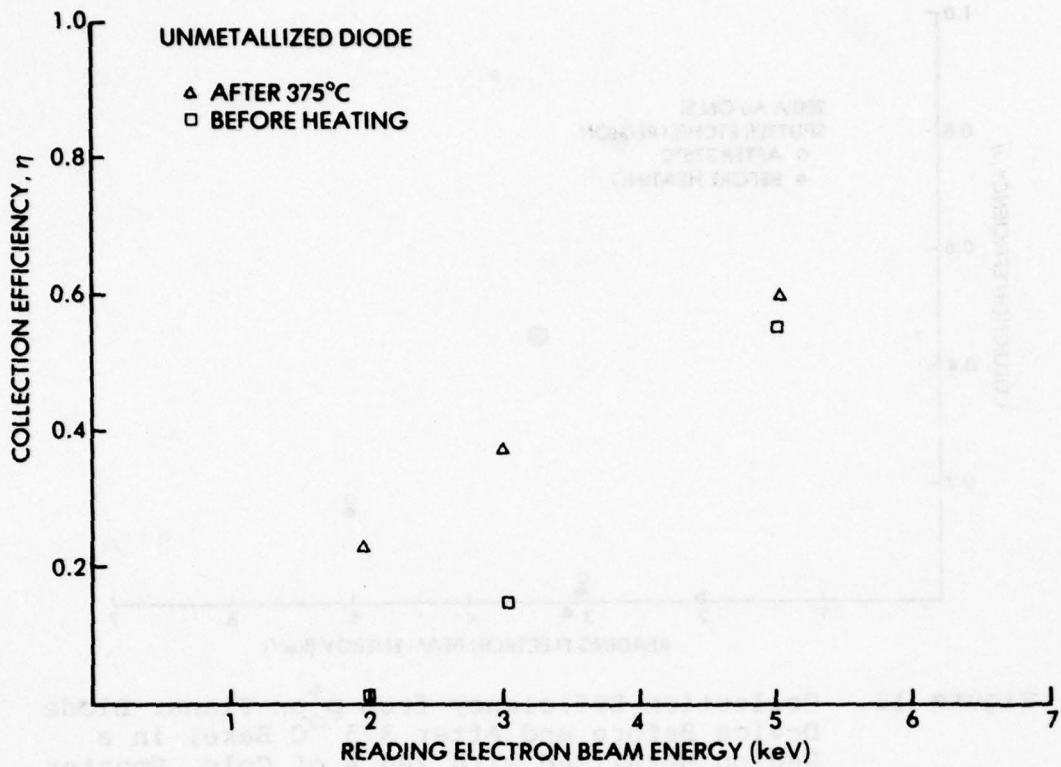
Figure 14.   Collection Efficiency from a p$^+$pn Diode
Before and After 375 $^\circ$C Bake

When this experiment was repeated for the 375 $^\circ$C bake tempera-
ture, agglomeration of the gold was observed, particularly in the
sputter etched region. Figures 15, 16, 17, and 18 illustrate
secondary electron micrographs taken before and after bake showing
changes in the gold metalization before and after 375 $^\circ$C bake,
in sputter etched and unetched regions. Before the bake cycle,
the 200 A sputter deposited gold film is smooth. The rim of the
sputter etched region is the only visible structure. After bake,
the gold film is no longer uniform, particularly in the dot de-
posited on a sputter etched region. In the non-sputter etched
region, the gold appeared to pull away from regions with poor
wetting properties. Figure 9 shows a close-up of the sputter

32
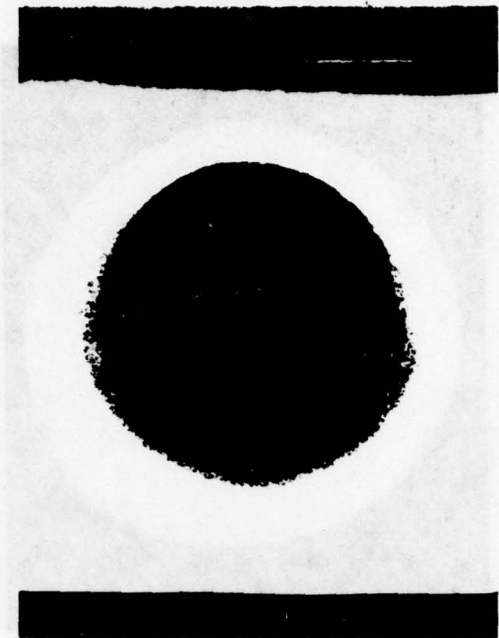
Figure 15. Secondary Electron Micrograph Showing Dot A4 on Target PAR 1(11)-2 Before 375 $^{\circ}$C Bake. Surface was sputter etched before deposition of 200 A gold film.
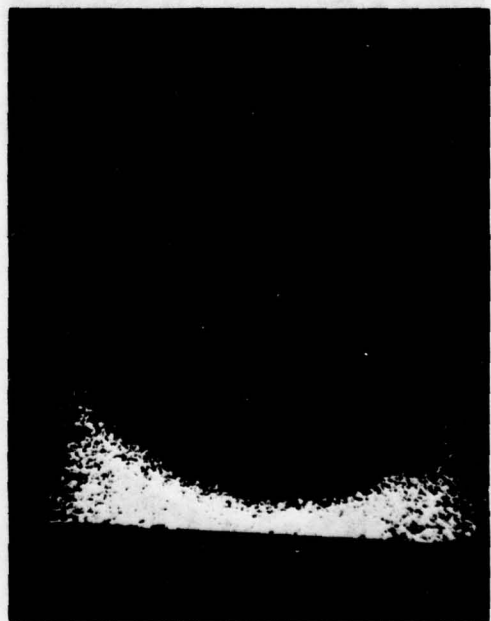
Figure 16. Secondary Electron Micrograph Showing Dot B4 on Target PAR 1(11)-2 Before 375 $^{\circ}$C Bake. Surface was not sputter etched before deposition of 200 A gold film.

33
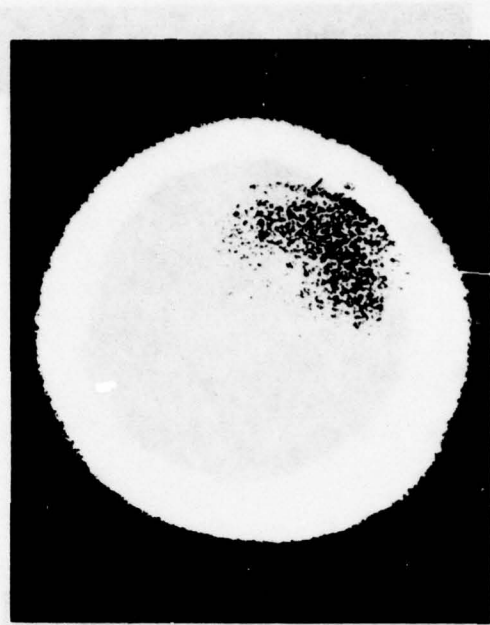
Figure 17. Secondary Electron Micrograph Showing Dot A4 on Target PAR 1(11)-2 after 375 $^\circ$C bake.
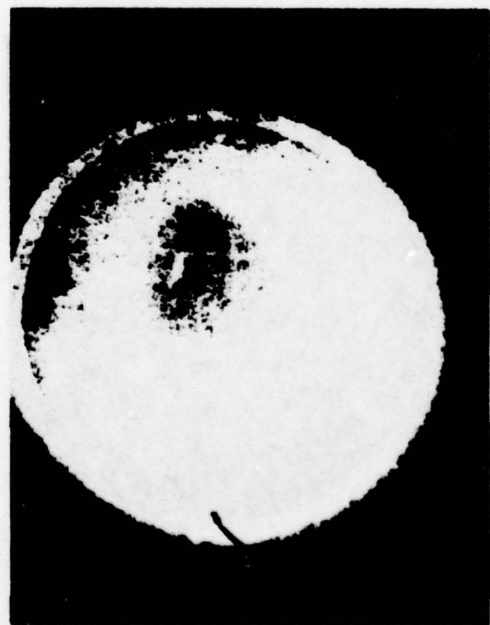
Figure 18. Secondary Electron Micrograph Showing Dot B4 on Target PAR 1(11)-2 after 375 $^\circ$C bake

34

Figure 19. Secondary Electron Micrograph of Faceted Gold Islands Present in Sputter Etched Region of Target PAR 1(11)-2 After 375 °C Bake. The gold regions are several microns in diameter.

etched region which displays clumps of gold across the surface. Multifaceted crystalline gold areas are present over the entire region. These islands are several microns in diameter. This effect could be the combined result of surface tension forces and the realignment of the gold film with the intermediate silicide layer whose growth is accelerated by the heating process. This growth rate is also dependent on surface conditions. An unmetalized device which had been sputter cleaned was carefully examined using the secondary signal in a scanning electron microscope to determine if the process induced surface irregularities. Even at the highest magnifications, no such nonuniformities were observed.

High temperature (800 °C) bakes were also performed to attempt
verification of the thermal equilibrium model (described in Sec-
tion II). Again, secondary and diode measurements were carried
out before and after heating of 1000 A gold films on target Par 1
(11)-4. Again, after the bake, the gold observed to be smooth
before heat treatment, agglomerated. Regular triangular gold crystals
were visible in the region sputter etched before gold deposition,
whereas in the nonsputter etched region, the gold had simply coagu-
lated into blobs (Figures 20 - 25). Diode measurements were made
on the gold islands; however, uncertainty in the thickness of these
faceted islands made a direct determination of the affected depth
difficult. There was evidence that alloying did occur underneath
the coagulated gold regions; however, the data was of insufficient
quality to allow corroboration with the model.
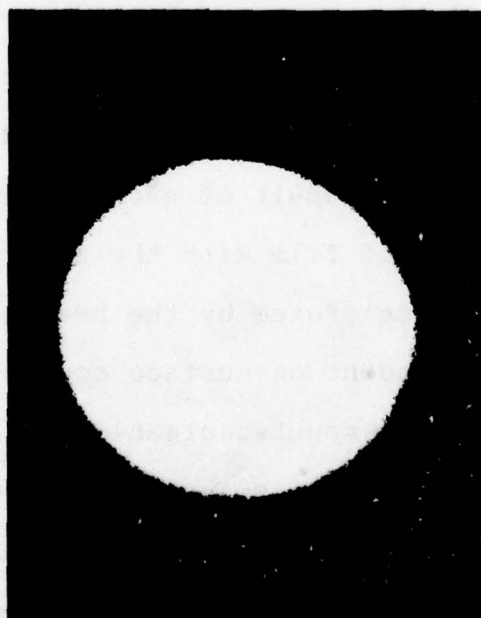
Figure 20.   Secondary Electron Micrograph of Dot B6 of
              Target PAR 1(11)-4, Formed by Sputter Deposition
              of 1000 A of Gold, Before 800 °C Bake

36
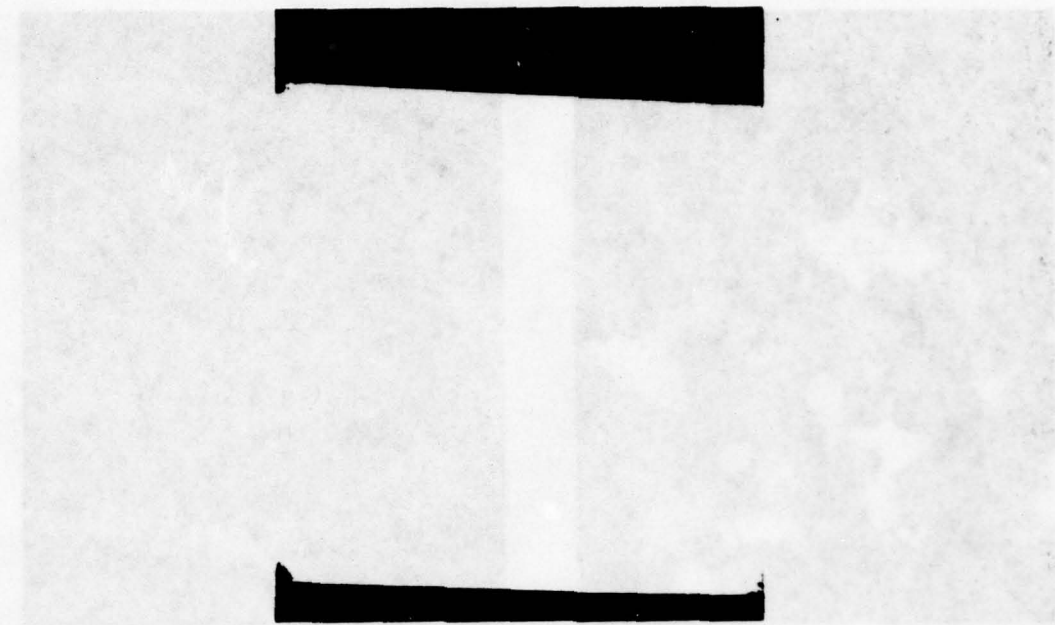
Figure 21. Secondary Electron Micrograph of Dot A5 of
Target PAR 1(11)-4, Formed by Sputter Deposition
of 1000 A of Gold in a Sputter Etched Region,
Before 800 $^{\circ}$C Bake
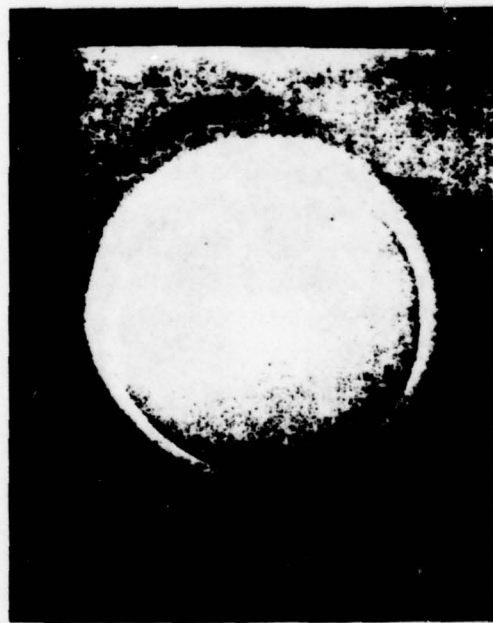
Figure 22. Secondary Electron Micrograph of Dot B6 of
Target PAR 1(11)-4 After 800 $^{\circ}$C Bake for
5 Minutes in Argon Ambient, Showing
Agglomeration of Gold

37
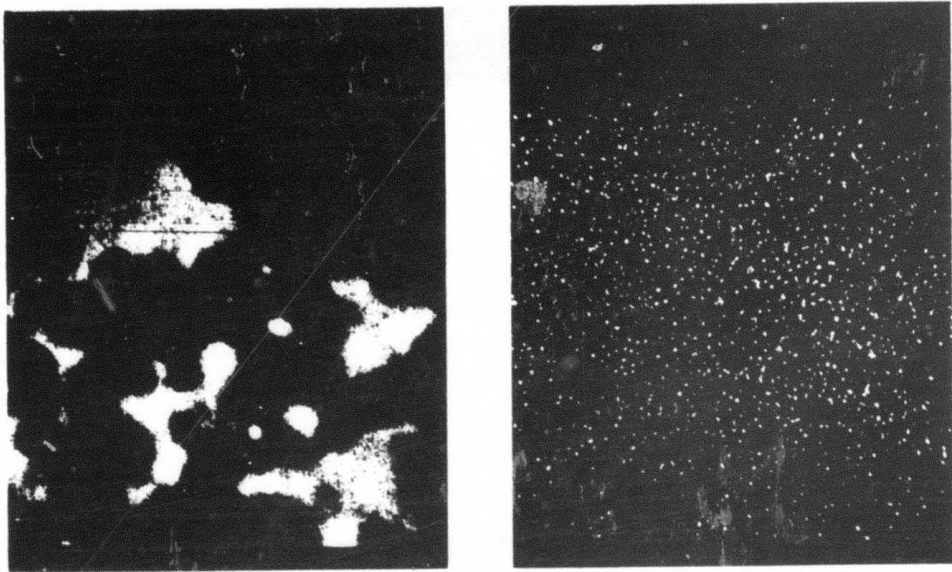
Figure 23.   Secondary Electron Micrograph Giving Magnified
Views of Regions of Agglomerated Gold in a
Non-sputter Etched Region of Target PAR 1(11)-4,
Dot B6
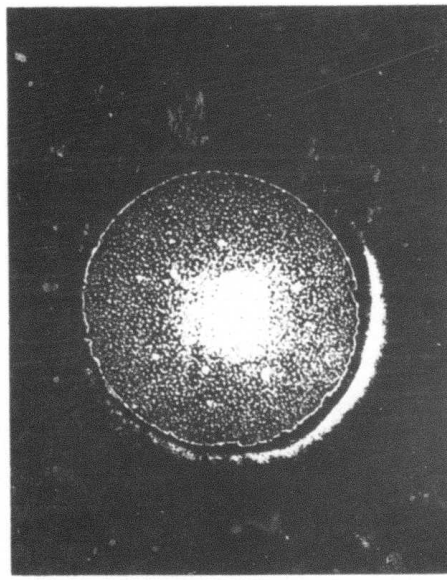
Figure 24.   Secondary Electron Micrograph of Dot B6
on Target PAR 1(11)-4 After $800\,^{\circ}C$ Bake
for 5 Minutes in Argon, Showing Triangular
Platelets of Gold
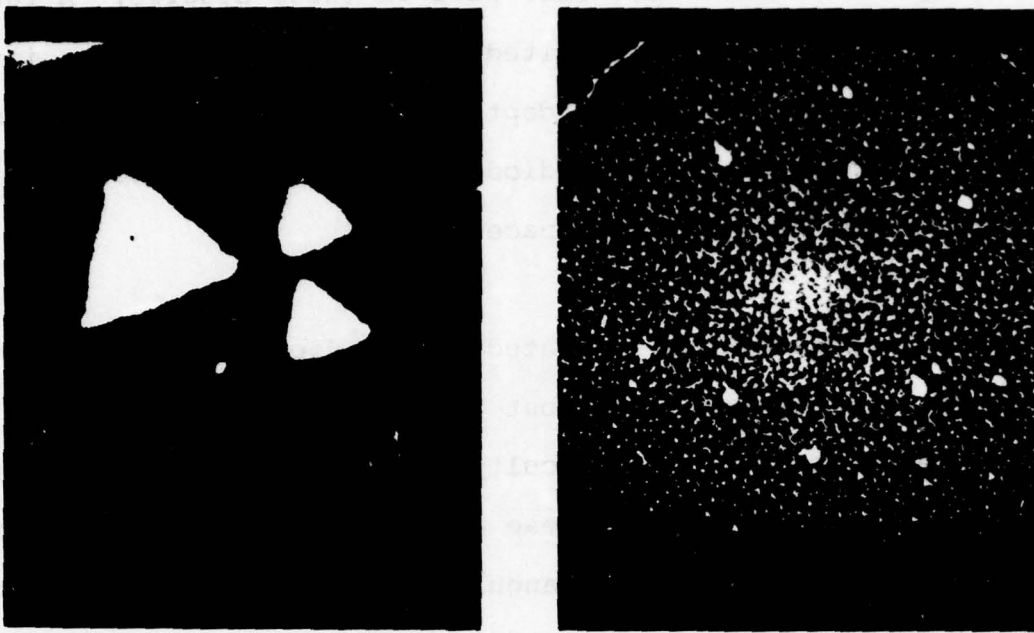
Figure 25.   Secondary Electron Micrographs Giving
Magnified Views of Triangular Gold
Platelets Formed in Sputter Etched
Regions of Target PAR 1(11)-4, Dot A5.
Platelets are typically 2 - 3 μ in
diameter.

Aluminum dot arrays on silicon planar diode structures were
also investigated, since this eutectic system is also of consider-
able interest. For these experiments, aluminum was sputtered in
a dot pattern on n and p diode structures. When this 1000 A alu-
minum film was examined at high magnification and low beam volt-
ages in the scanning electron microscope, collection efficiencies
resulted which indicated the presence of tiny pinholes. While
too small to be observed with secondary electrons, they did allow
penetration of the beam. The presence of such pinholes may be
desirable, since they may reduce the thermal conductivity in the
film. Similar effects had been seen in gold sputter deposited
films.

39

Evaporated films were also used in these studies. A 1000 A thick aluminum film was deposited on target MP 3-4(3) for investigation of the affected alloy depth at 790 ^{o}C heating in argon ambient for 5 minutes. Again, diode and secondary measurements were made before and after the furnace cycle.

These measurements indicated that a diode had indeed been produced by alloy formation, but again, agglomeration of the film during bake resulted in difficulty in obtaining absolute measurements of the alloy depth. These agglomerations were in the form of film discontinuity and triangular platelets of the order of 10 μm in size. No sputter cleaning had been done on this sample. Secondary electron micrographs illustrating these metal islands are shown in Figures 26 and 27. Figure 28 shows diode signal from

Figure 26.   Secondary Electron Micrograph
Showing Restructured 1000 A
Aluminum Film on Target MP 3-4(3)

40
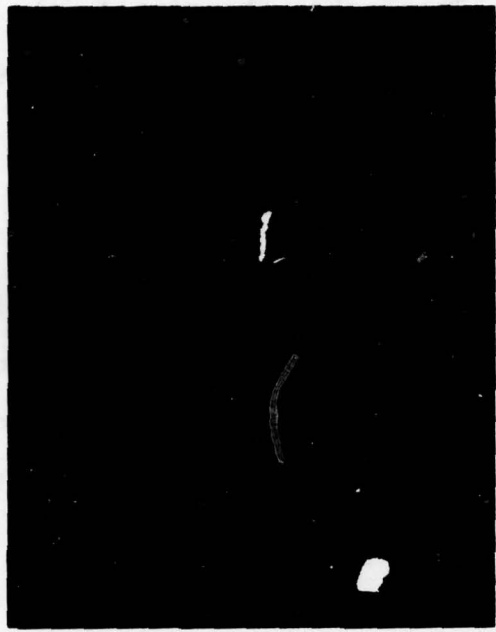
Figure 27. Secondary Electron Micrograph Showing
Magnified Al Triangular Platelet
($\sim 20\mu$ on a side) from Target
MP 3-4(3) After Heating at 690 $^{\circ}$C

Figure 28. Diode Readout from a Region Heated
at 690 $^{\circ}$C on Target MP 3-4(3),
Showing Low Gain in Regions of Metal
Agglomeration

41

a similar region. The darker the signal, the lower the gain in an area, such as at the location of the triangles.

SUMMARY

The experiments did clearly show that writing is not accomplished by simply bringing the constituents to their eutectic temperature. Higher temperatures are required; but the experiments neither proved nor disproved the predictions of the model in Section II on this point.

Experiments did indicate that thermal biasing of this type of target would be quite difficult, in view of the formation of silicide layers, and of the restructuring of the overlaying films. In addition, the experiments showed that there is a definite problem with making the metal species wet the surface of the silicon during alloying. For the alloy function approach to work, a method must be found to make the metal stay put when heated so that alloying can take place. The interaction of the metal layers with defects during the alloy process is another potential problem.

SECTION IV
THERMAL MILLING OF Se-As ALLOYS

INTRODUCTION

The electron milling concept is shown schematically in Figure 29. A focused electron beam locally heats a film of Se on a Si diode target causing vaporization of the Se. After writing, the target is read using an electron beam of the same energy but of lower beam current. Regions of reduced Se thickness due to the machining produce higher readout signals from the diode because of the increased penetration of the electron beam energy in the Si diode.
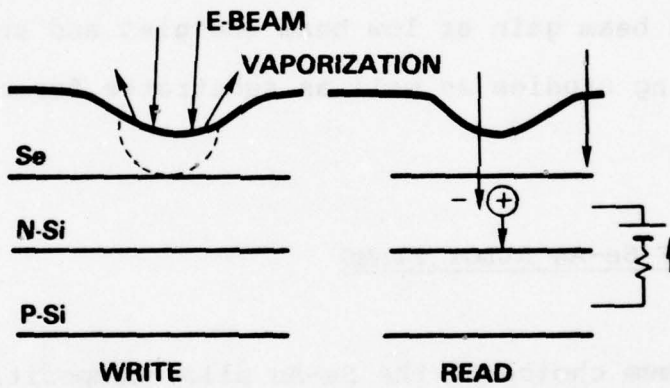
Figure 29. Electron Beam Milling Concept

Se alloyed with As was chosen for this application because it is a material with the following properties: low thermal conductivity, moderate mass density, low boiling temperature, good stability, and uniform amorphous thin films are possible. Amorphous Se films are known to have a strong tendency to recrystallize at room temperature. Crystalline films are in general undesirable because they have higher thermal conductivities and tend to be nonuniform on the scale of $0.1 \mu m$. Also films which

43

undergo amorphous to crystalline transitions near room temperature are unlikely to be dimensionally stable over long periods of time. The addition of As to Se has been known for some time to significantly stabilize Se against crystallization.

CHOICE OF SUBSTRATE PLANAR DIODE

N type planar diodes were chosen as the substrates for the Se milling investigations. These are identical to the As^+ implant through oxide targets developed during Phase I and Phase II. They are processed using the NAR process described in the Phase II Interim Report (June 1 - December 31, 1977). These diodes have high electron beam gain at low beam energies and are suitable for general writing studies as well as substrates for high resolution recording.

PREPARATION OF Se-As ALLOY FILMS

The optimum choice of the Se-As alloy composition for this application has not been determined. In general, the thermal conductivity of Se-As glasses increases with progressively greater As content up to 40% As [6]. This effect is less than a factor of two so that other factors will dominate the choice. In particular, the conditions of film preparation may be more important. As mentioned above, the As stabilizes the amorphous Se films against recrystallization [14, 17, 18, 19, 20, 33]. Amorphous Se exists in both Se_8 rings and long chains. Both of these forms tend to form complex crystalline structures with higher thermal

44

conductivities. Monoclinic and hexagonal crystals are formed by the Se rings and long chains, respectively. Addition of As forms $AsSe_{3/2}$ sites that break up the rings and cause cross-linking of the chain. [13]. There is theoretical [20] and experimental evidence [33] that only 100 ppm of As is required to achieve this stabilization. At higher As concentrations this process eventually results in the As_2Se_3 structure. Heating above the glass transition temperature T_g may cause some crystallization [6, 24] in the higher As concentration alloys. The extent to which this crystallization persists when subjected to rapid or slow cooling is not known.

Based on this evaluation it was decided to produce As-Se alloys with compositions ~20% As. The principal reasons for this were: this is the eutectic composition and so it has the lowest melting point, and it was the composition utilized in the previous GE work at Electronics Laboratory, Syracuse, N.Y. As will be seen below, all of the films prepared to date have much lower As concentrations (~1%). These films seem to be completely suitable as memory materials. As just discussed, there is evidence that As concentrations as low as 100 ppm may produce equally or more stable amorphous Se films [19, 20]. One percent As films are apparently a feasible composition for xerography drums [12, 11]. With a heating rate of 3 $^{\circ}$C/min the crystallization temperature of As-Se increases from 160 $^{\circ}$C to 196 $^{\circ}$C as the As concentration is increased from 0 to 2% [20]. This process provides some indication of the strong effect of As on the crystallization.

45

As-Se alloys were prepared by heating a charge of 23.3 g of Se and 5.8 g of As in an open carbon crucible in flowing argon at atmospheric pressure. For the first alloy run the temperature was increased slowly over 1 hour to 315 $^{\circ}$C and then dropped back to 300 $^{\circ}$C for 12 hours. Considerable evaporation of material occurred. Subsequent X-ray florescence analysis of the alloy indicated a composition of 1% As with no other impurities above 0.1%. Electron microprobe studies indicated no composition variations in the alloy although the 1% As composition is below the detection threshold due to the Bremsthrahlung background. It is believed that the As preferentially evaporated from the crucible. The vapor pressure of As in a dilute Se alloy is not known but it is predicted that the As and Se vapor pressures should be equal at 387 $^{\circ}$C [12]. Hence it is possible, but unlikely, that the As would preferentially evaporate at 300 $^{\circ}$C. A second possibility is the formation of As oxides due to an impure Ar gas or other leakage in the system. All of the As oxides are unstable or sublime below 315 $^{\circ}$C. A second alloy run at maximum temperature of 230 $^{\circ}$C did not produce mixing of the As and Se. Future alloys will be made in sealed evacuated quartz ampoules at temperatures ~ 350 $^{\circ}$C to prevent loss of As during alloying. All of the Se films prepared for the investigation described below used this material from the first alloy run.

The films were evaporated in a bell jar using indirectly heated carbon crucibles. The thickness was monitored with an

Infocon quartz crystal monitor and the evaporation controlled by a shutter. Deposition rates were typically 10 to 100 $\overset{o}{A}$/sec at the target. The films have not yet been analyzed, but based on the work of Sigai [12] and our estimates of the boat temperature (~ 300 ^oC), they should be $\lesssim$ 1% As. The Se should preferentially evaporate because of its higher vapor pressure. Since the shutter is in place during the initial part of the evaporation some As enrichment of the charge occurs before evaporation is started. Sigai found that for dilute (0.5% As) alloys it was impossible to reach a temperature high enough to obtain equal evaporation rates for As and Se. This he attributed to the poor thermal conductivity of the Se and the effect of evaporative cooling. Because of the compensating enrichment effect and the fact that the charge was typically evaporated to near completion it is expected that the films have ~ 1% As. Microprobe dispersive analysis indicated less than 2% As in the two samples tested. [NAR1-2(2), NAR1-12(1)].

Test glass disks are included with every evaporation. These are then covered with a thin Al film and the physical thickness measured using a Sloan M-100 Angstrometer (Fizeau technique). Figure 30 shows the correlation between the reported thickness based on the quartz monitor and the physical thickness. The quartz monitor thickness is based on a mass density of 4.25 g/cm^2 [15] and includes cos θ and r^2 corrections for the differences in monitor and sample positions. The slight disagreement is most likely due to a non cosine evaporation distribution for

47

the carbon crucible since about 10% of the Se charge is shielded from the monitor by the edge of the crucible.
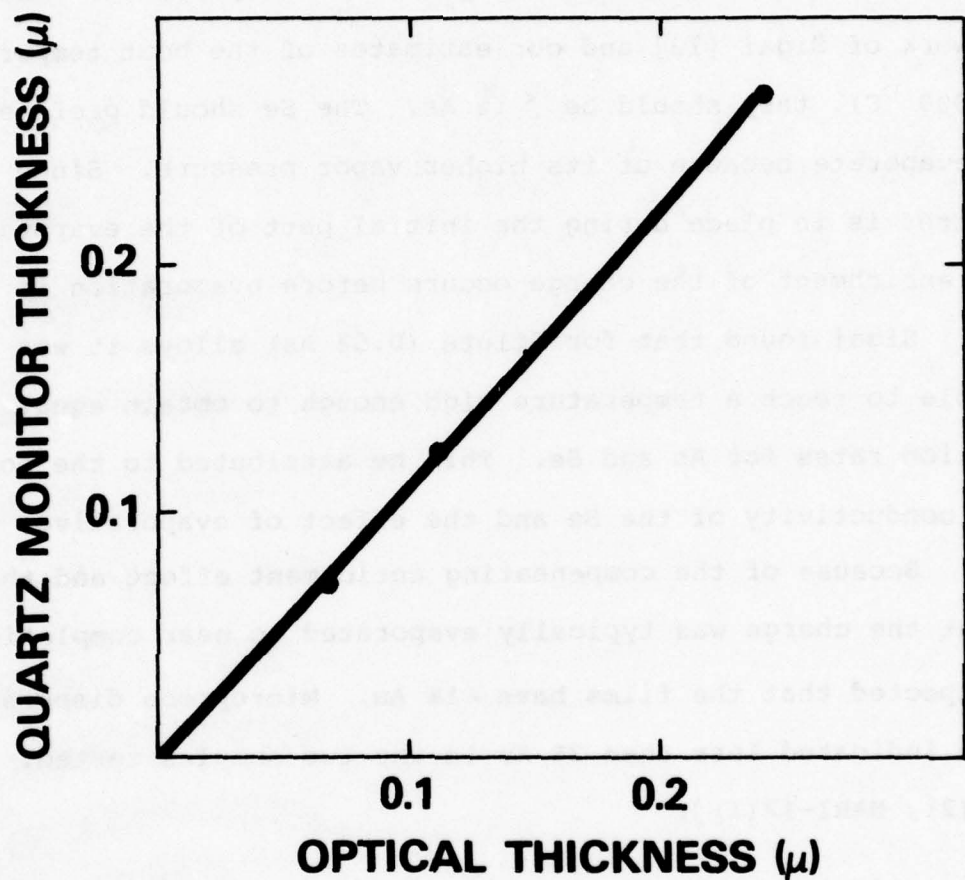
Figure 30. Comparison of Evaporated Se Film Thickness Measured by Quartz Monitor and Optical Interference

STABILITY OF THE EVAPORATED FILMS

Optical and SEM examination of the evaporated films indicate that they are amorphous and of generally good quality. Test films evaporated on glass disks and stored in a normal laboratory environment for several months still exhibit the reddish color and good optical transmission characteristic of amorphous Se

films. No degradation of the films has been observed although those films which had Al evaporated on them have shown some re-action with the Al. Al is a very reactive material and so this is not surprising.

Se WRITING EXPERIMENTS

Electron beam writing has been done in the Coates and Welter (C&W) field emission electron writing column purchased during Phase I. For writing, the beam is stepped in a 16 x 16 matrix of dots using two synchronized staircase generators. A number of modes of operation are possible. The beam moves between the dots of the matrix in <1 µsec. The time between transitions to a new spot can be varied between 20 msec and 0.088 msec. Without the use of beam blanking, the dwell time per spot can be varied between these limits. The matrix generator can be synchronized to a pulse generator which is used to drive the electrostatic beam blanker of the column. In this mode the beam dwell time can be as small as 0.5 µsec. This minimum time is limited by the performance of the C&W blanker. The beam blanker reduces the beam current to about 10% which is normally sufficient to prevent further writing. In either mode, single lines or the entire matrix can be written in a single shot or continuous modes.

In general, the operation of the column has been erratic. This has severely hampered progress on electron milling. The typical best performance of the column is 100 nA at 15 keV with

a spot size $\lesssim 0.1 \mu$m and 25 nA at 5 keV with a similar spot size $\gtrsim 0.1\mu$. At higher currents the spot size increases dramatically. The introduction of the beam blanking aperture into the column tends to further degrade the beam current and spot size.

Initially attempts were made to write on the 0.05 μm Se film. These were generally unsuccessful although some writing was obtained. Figure 31 shows a secondary image of a portion of the 16 x 16 dot array written with 70 nA at 5 keV and a dwell time of 20 msec/spot repeated 4 times at each spot. The spot size was ~ 0.2 to 0.3 μ during this writing experiment. Each of the 3 white dots corresponds to a single written bit. Estimates of the temperature rise achieved in this case are 200 $^{\circ}$C which is just sufficient to melt the Se film. The electron beam position is not completely stable because of a small differentiated part of the TV raster sync pulse signal which couples into the deflection coils of the column. This couples equally into each axis, so for long dwell times the beam spends 3% of the time deflected at a 45° angle. This causes a slight heating of the film in these adjacent areas. Apparently because of the surface tension characteritics of the molten Se, it is pulled towards these slightly warmer areas resulting in two raised regions of Se on each side of the centrally heated spot. The origin of the third raised spot is not as clear but may be related to astigmatism in the spot. Using diode signals it is inferred that the amount of change in Se thickness is $\gtrsim$ 5%.
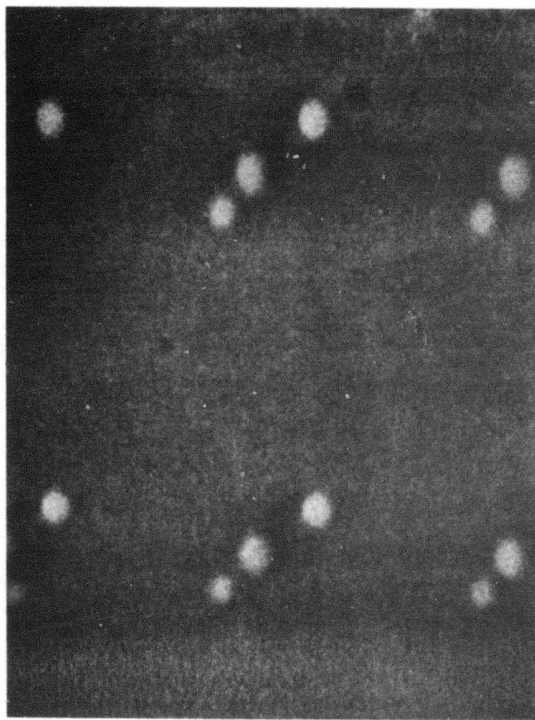
Figure 31.   Secondary Emission Image
of Viscous Flow Writing
on a 0.05 Micron Thick
As-Se Film.   Electron
beam writing at 5 keV and
70 nA with a spot size
~0.25 microns.

This does demonstrate ~0.3 μ writing of Se films.   The time
required to form these structures is 20 msec.   At shorter times
no writing was seen.   Several pulses at 20 msec were required
to produce a visible effect.   Se is a very viscous material [16]
and hence flows very slowly at these temperatures.   This type
of viscous flow writing is not useful for memory applications.

In its present condition the column does not provide suf-
ficient power to vaporize thin Se films.   In order to study vapor-
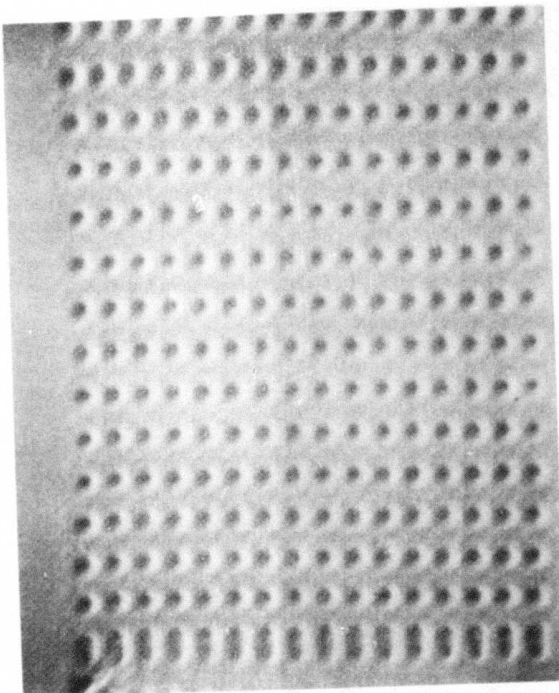
Figure 32. (a) Secondary Emission Image of a Dot Matrix Written on 1.8 Micron Thick As-Se Film at 100 nA, 16 keV and 100 μsec. per spot.

(b) Typical Diode Signal Readout of a Written Dot Matrix. Right trace is beam on signal in an area with no Se film, middle trace is the modulated diode signal as the beam is scanned across a row of dots. The base line trace is the beam off reference. Left image is a diode signal, Z-axis modulated image, of the written dot matrix.

52
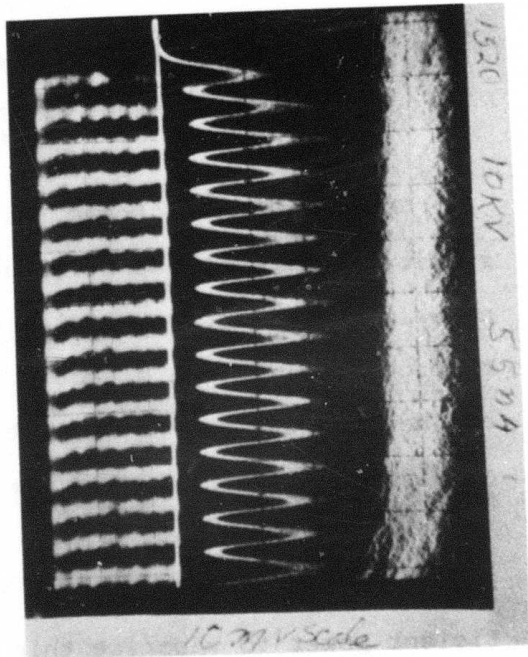
ization writing it was necessary to study thicker Se films and to raise the beam voltage. Much greater temperature rises can be achieved in thicker films because of the increased distance to the high thermal conductivity silicon substrate. Figure 32 shows a secondary emission image of some typical writing on the 1.8 μm Se films written at 15 keV and 140 nA. The electron spot size was 0.2 μm. The limitation on the size of the written regions is ~ 1 μ due to electron scattering.

The depth of the written holes is determined from the electron beam induced current in the underlying pn junction. This provides a very convenient method for the determination of the residual Se at the bottom of the hole. Such measurements would be nearly impossible by other techniques. Figure 33 shows a typical set of such measurements. Shown is the diode collection efficiency in the center of the written dots measured at several beam voltages. For writing the electron beam voltage was 15 keV and 140 nA or 70 nA. The spot size was ~0.1μm so the heated volume is determined by the electron range. The diode measurements are done at low beam currents $\lesssim$10 nA to prevent further machining of the film. No degradation or change in signal were seen during these measurements. The solid curves are a model calculation based on the following assumptions. The collection probability for the diode is as shown in Figure 19 of the Phase I Fourth Interim Report (January 16 - April 15, 1977) for Sv=10^6 cm/sec. This is appropriate for the NAR type diodes used here and provides a good fit to the measured collection efficiencies as shown in

53
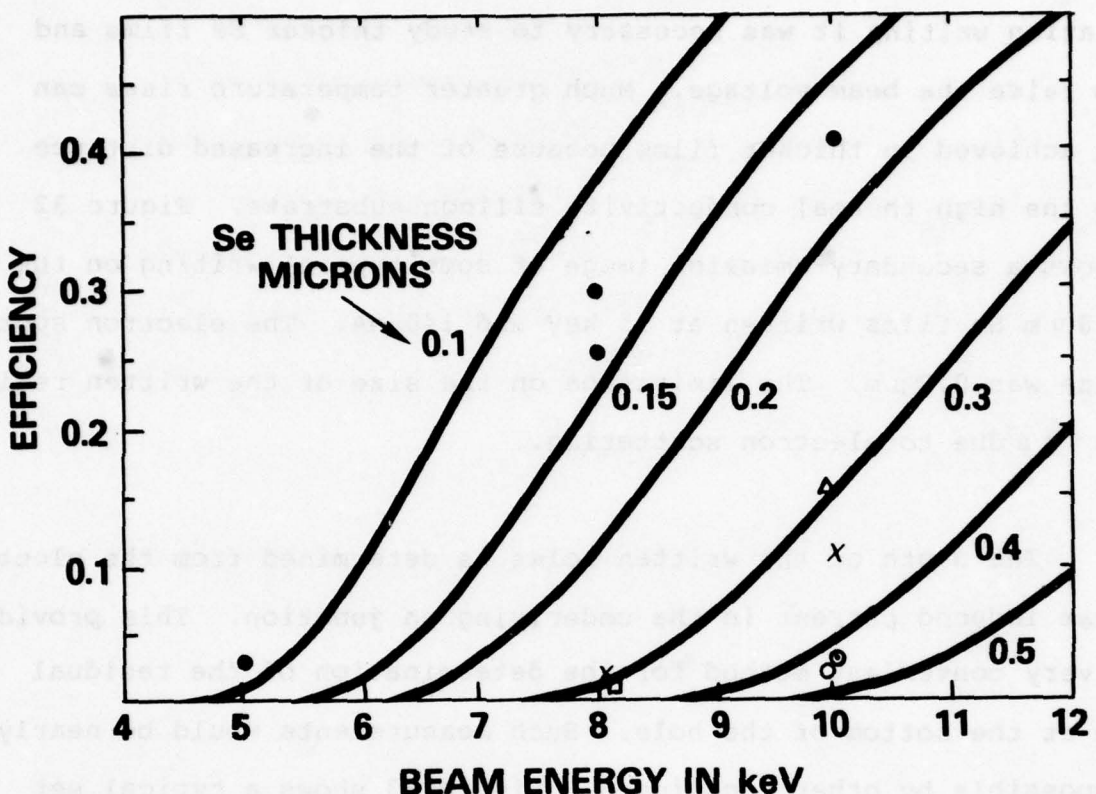
Figure 33. Diode Gain Measurements for the Determination
of Residual Se Film Thickness in Milled Holes
for Various Indicated Beam Currents and Dwell
Times ■ 0.24 msec. and 140 nA, ● 16 msec. and
140 nA (X) 1 msec. and 140 nA, (0) 0.11 msec.
and 140 nA, (Δ) 16 msec. and 70 nA and (θ)
1 msec. and 70 nA. All writing at 16 keV.
Model curves based on Equation (14).

Figure 17 of the same report. The effect of the Se is to absorb
electron beam energy as though it were a silicon film of thickness
$(\rho_{Se}/\rho_{Si})T_{Se}$ where ρ_{Se} and ρ_{Si} are the mass densities of Se and
Si respectively, and T_{Se} is the residual Se thickness after machin-
ing. The electron energy loss is described by the Grün formulation
as described on page 100 of the Phase I First Quarterly Report
(April 15 - July 15, 1976). This is a reasonable although not
exact method of adapting the uniform media Grün function data
to this two layer case. It is identical to the assumptions used

54

in the thermal modeling calculations described in more detail
in Section V of this report. Using these assumptions and gener-
alizing to two films of thickness T_1 and T_2 with mass densities
ρ_1 and ρ_2 the collection efficiency is given by:

$$\eta(E_B, T_{Se}) = \int_{q_1+q_2}^{1.1} \lambda(q)\ P(q-q_1-q_2)R_G(\rho_{Si}, E_B) \qquad (14)$$

$$q_1 = \frac{T_1}{R_G(\rho_1\ E_B)} \qquad q_2 = \frac{T_2}{R_G(\rho_2\ E_B)}$$

where $\quad R_G(\rho, E_B) = (\beta/\rho)\ E_B^{1.75} \quad E_B$ in KeV $\beta = 4.28 \times 10^{-6}$ g/cm^2 (15)

is the Grün range which depends upon the mass density and the
beam energy E_B. $\lambda(q)$ is the normalized Grün function for which
we use the computational approximation [36]

$$\lambda(q) = 0.6 + 6.21q - 12.40q^2 + 5.69q^3 \qquad (16)$$

As can be seen in Figure 33, the fit to the data is satisfac-
tory. The systematic deviations are probably due to the error
in approximating the energy loss function. These problems notwith-
standing, the data in Figure 33 still provide a useful measure
of the residual Se left in the written areas. If the thickness
is always estimated for approximately the same collection efficiency
(~0.1) the thickness determinations will be the most reliable

55

and have the least scatter. Table 1 shows the measured writing
depths for three different beam currents as determined from Fig-
ure 33.

TABLE 1

MEASURED WRITING DEPTHS FROM FIGURE 5
FOR 16 keV WRITING ON 1.6 µ As-Se

Beam Current	Dwell Time	Residual Thickness
µA	µsec	µ
140	16	0.12
140	1	0.32
140	0.24	0.34
140	0.11	0.45
70	16	0.28
70	1	0.45

Secondary emission images of additional writing experiments
show that the writing depth becomes very small for dwell times
between 10 and 50 µ sec for beam currents in the range of 100 nA.

MODELS FOR THE WRITING PROCESS

A number of factors which are important for an understanding
of the thermal milling process will be considered separately.
These are: the vapor pressure and its relation to the evapora-
tion rate of the material; heating models for the temperature
rise in the multilayer targets; the effect of the latent heats
of vaporization and fusion; and the thermal properties of amorphous

56

Se-As alloys. Based on these discussions a quantitative model for the milling process will be described.

A. Thermal Properties

The thermal conductivity of bulk amorphous Se-As alloys is summarized in Table 2 based on the measurements of several investigators. As can be seen from the table, there is considerable scatter in the values obtained. Some of the scatter is undoubtedly due to the fact that Se can have many amorphous structures. (See Reference 20.) Also note that all of these measurements are on bulk material, which is prepared by quenching or slow cooling from the melt rather than vacuum evaporation. For our modeling studies a value of 0.005 watt/cm/sec will be adopted as a nominal pessimistic value. The thermal conductivity of Se-As tends to increase moderately with temperature except for a dip at the glass temperature T_g which occurs between 50 and 200 $^{\circ}$C depending upon the composition [6].

The heat capacity is of less critical importance since it determines only the thermal time constant and not the maximum temperature rise. A good nominal value at room temperature for amorphous Se is $C_p = 1.35$ J/cm^3/deg C [22].

B. Vapor Pressure

The vapor pressure curves [24, 23, 12] for pure As and Se are shown in Figure 34. The standard vapor pressure curve for

57
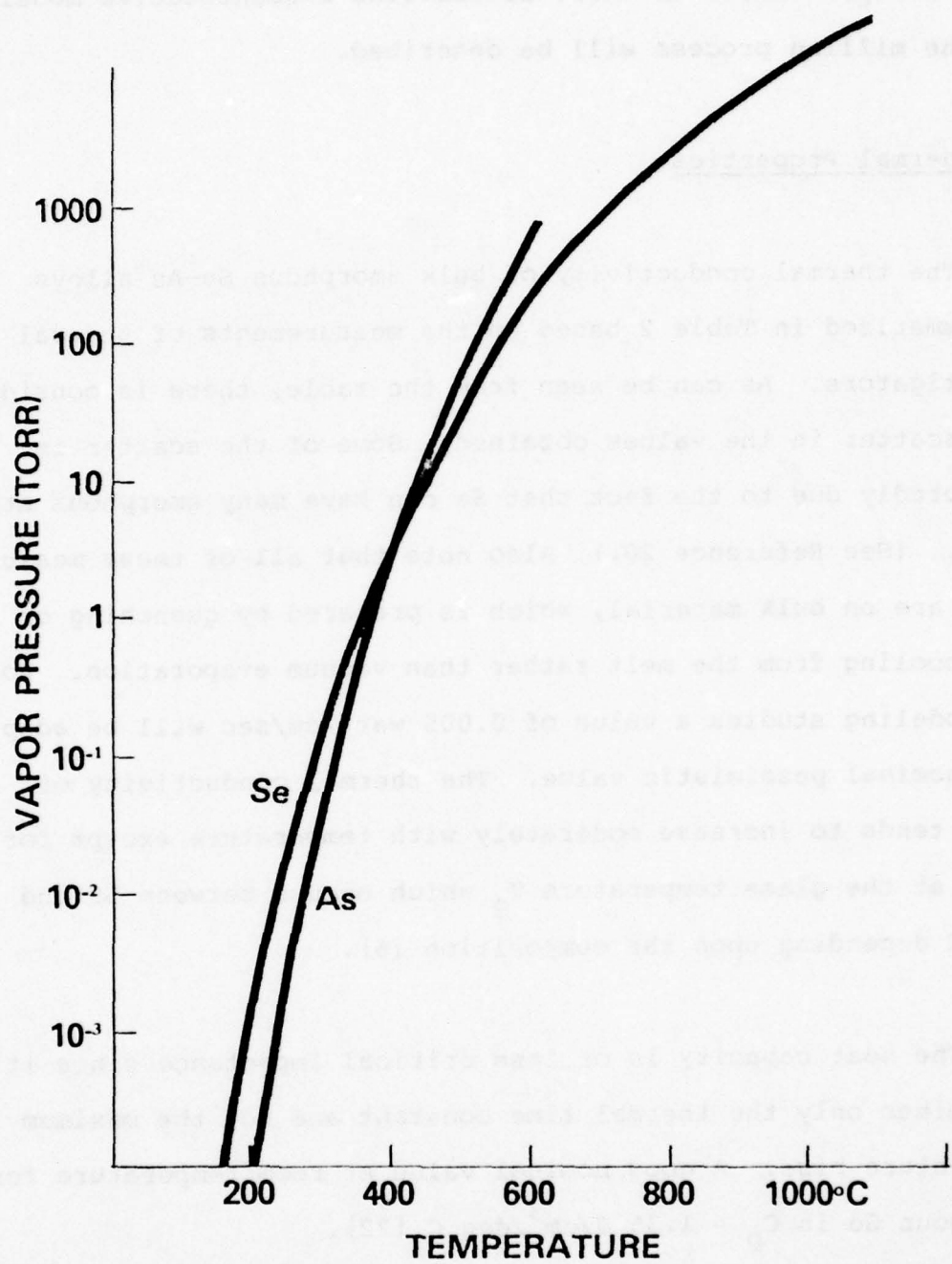
Figure 34. Vapor Pressure for Se and As Versus Temperature

TABLE 2
THERMAL CONDUCTIVITY OF BULK As Se GLASSES
(Amorphous Alloys) at 40 °C

At % As	K watts/cm-sec	Reference
0	3.0×10^{-3}	6
10	3.3	6
20	3.6	6
30	3.4	6
40	4.0	6
45	3.6	6
50	3.2	6
40	2.0	7, after reference 8
40	3.0	8
40	7.0	9, 10, after reference 8
20(?)	1.4	21
0	6.8	22
0	4.9 (20 °C)	22

59

As is based on the sublimination of As from the solid phase. Sigai [12] has estimated from thermodynamic data the correction for the vapor pressure over the liquid phase. This correction is very small. The Se curve can be described by

$$\log P_{atm} = A - B/T \tag{17}$$

where P_{atm} denotes the vapor pressure in units of atmospheres, $A = 5.6$ and $B = 5376 \, ^{O}K$.

For significant concentrations of As, the vapor pressure of each component of the alloy can be determined using the law of Raoult:

$$\frac{P_{As}^{O} - P_{As}}{P_{As}^{O}} = 1-X_{As} = \frac{P_{Se}^{O} - P_{Se}}{P_{Se}^{O}} = X_{As} \tag{18}$$

where X_{As} is the mole fraction of As in the liquid P_{As}^{O} and P_{Se}^{O} are the vapor pressures of As and Se and P_{As} and P_{Se} are the vapor pressures in the alloy. Since the As and Se vapor pressures are so similar and the As is only a small fraction of the alloy composition this correction can be neglected.

C. Evaporation Rate

The evaporation rate in vacuum can be determined from the vapor pressure using an argument originally due to Langmuir (see

60

Eq. 32 and References 29 and 30 for a critical discussion). The
evaporation flux J_v in g-atoms/cm^2 sec is given by:

$$J_v = \frac{\alpha_v f P_{atm}}{(2\pi MRT)^{1/2}} \tag{19}$$

where M is the molecular weight in grams, MR = 1.987 cal/g-atom$^\circ$K
is the gas constant, $f = 1.554$ g$^{1/2}$ cal$^{1/2}$/cm^2 atm sec is a con-
version factor and α_v is a sticking or condensation parameter.
This is essentially the probability of evaporation or the proba-
bility of condensation. For liquid to vapor transitions α_v is
normally $\simeq$ 1. The derivation of this equation essentially assumes
no interference from the evaporated material still in the vicinity
of the evaporating region. That is, the derivation assumes the
vapor pressure is much larger than the background pressure.
This may not be true at very high evaporation rates so that Eq. 19
may overestimate the evaporation rate at high rates.

As an example, Eq. 19 gives for Se at T = 690 $^\circ$C where P_{atm} =
1 atm, J_v = 2.64 cm/sec. Hence to machine 0.1 microns of material
at this temperature would require 3.8 μ sec. To machine significant
amounts of material in $\lesssim$ 0.1μ sec will require $P \gtrsim$ 10 atm or $T \gtrsim$ 920
$^\circ$C.

D. Heat of Vaporization

The heats of transformation of Se (ΔH_ℓ for the solid to
liquid change and ΔH_v for the liquid to vapor change) are tabu-
lated in Table 3.

61

TABLE 3

HEATS OF TRANSFORMATION OF Se

Phase Change			Reference
ΔH_ℓ	1.25	kcal/g atoms	23
	1.3		31
ΔH	14.27		23
	6.3		31

It can also be shown [33] that the vapor pressure is related to the heat of vaporization or the Gibbs free energy change between the liquid and vapor state by:

$$\log P_{atm} = \frac{-\Delta H_v}{4.575T} + \text{const} \tag{20}$$

Using the fit to the vapor pressure data in Eq. 17 gives ΔH_v = 24.6 kcal/g-atom which does not agree well with Table 3. Since the properties of high temperature Se have not been well studied, it is helpful to keep in mind that the heats of transformation in Table 3 may be in error. For the purposes of modeling we will use 1.25 and 14.3 kcal/g at for the ΔH and ΔH_v.

To estimate the effect of these heats of transformation on the writing process, consider the relative powers involved in vaporizing a $(0.1\mu)^3$ volume of Se in 0.1 μsec. Using the bulk Se mass density, ΔH_v = 14.3 kcal/g-atom = 3250 J/cm^3. To vaporize

62

the 0.1μ cube of Se requires ΔH_v volume/time = 3.25×10^{-5} watts into heat of vaporization. As will be seen, to maintain the temperature of this volume of material at 900 °C requires $\sim 5 \times 10^{-4}$ watts so the effect of evaporative cooling is about a 10% effect. However, to machine the same amount of material in 0.01μ sec would require 10 times the power into heat of vaporization which is comparable to the power required to maintain the temperature. Hence the beam power would have to be almost doubled to provide the heat of vaporization. The heat of vaporization will become a critical limitation on the writing rate above 10 Mbits/sec.

E. Backscattered Electrons

Se is a material of relatively high atomic number so that the reflected energy due to backscattered electrons is non-negligible. Figure 35 shows the number backscatter ratio η versus atomic number Z from Bishop [26] and Palluel [27] at 5 keV. The energy dependence above 5 keV is very weak. The energy backscatter ratio f is the ratio of the total energy backscattered from the sample material to the incident electron energy. The average energy of the backscattered electrons is ~ 0.5. A more exact relation is given by Sternglass [28] based on integrals of the backscatter energy distributions as:

$$f = (0.45 + 0.002Z) \eta \qquad (21)$$

From Figure 35 $f(Se) = 0.20$ using Bishop's value for η.

63
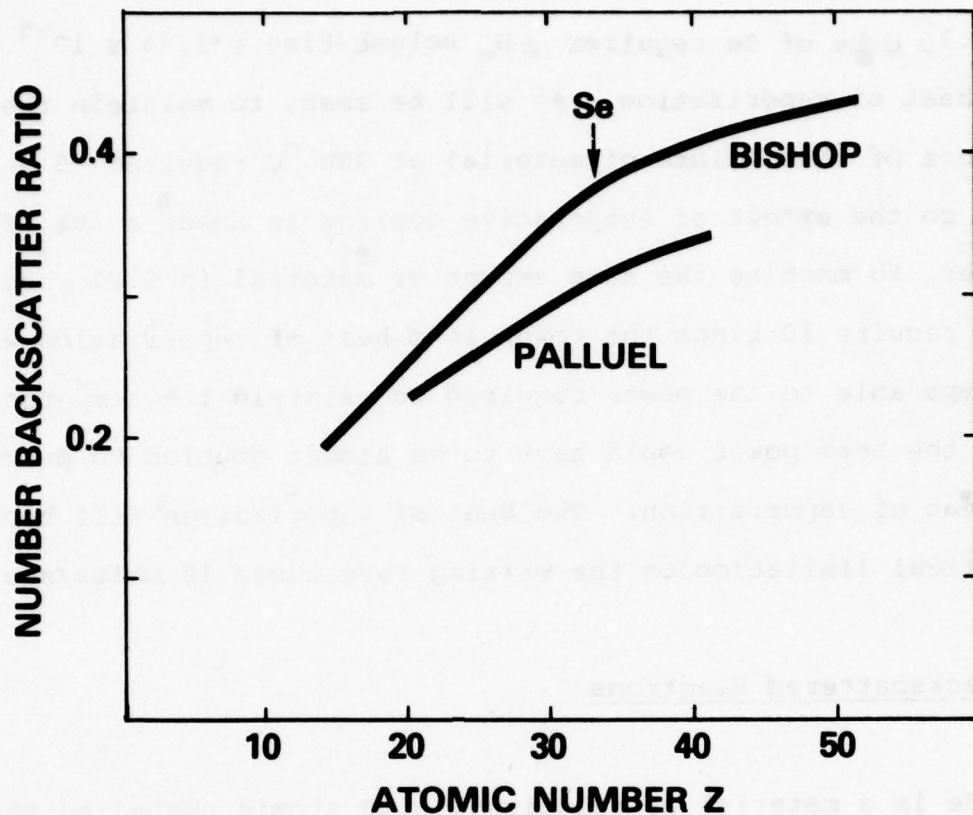
Figure 35.   Number Backscatter Ratio for 5 keV Electrons
Versus Atomic Number Based on the Results
of Bishop and Palluel

F. Heating Models

As described in a separate section of this report a full
two-dimensional heating model is being applied to the calculation
of the temperature rises in multilayer targets. In this section
approximate models for the heating and for the process using
one- and two-dimensional heating models will be described. These
are combined with the vaporization properties in the following
section to provide a complete milling model.

64
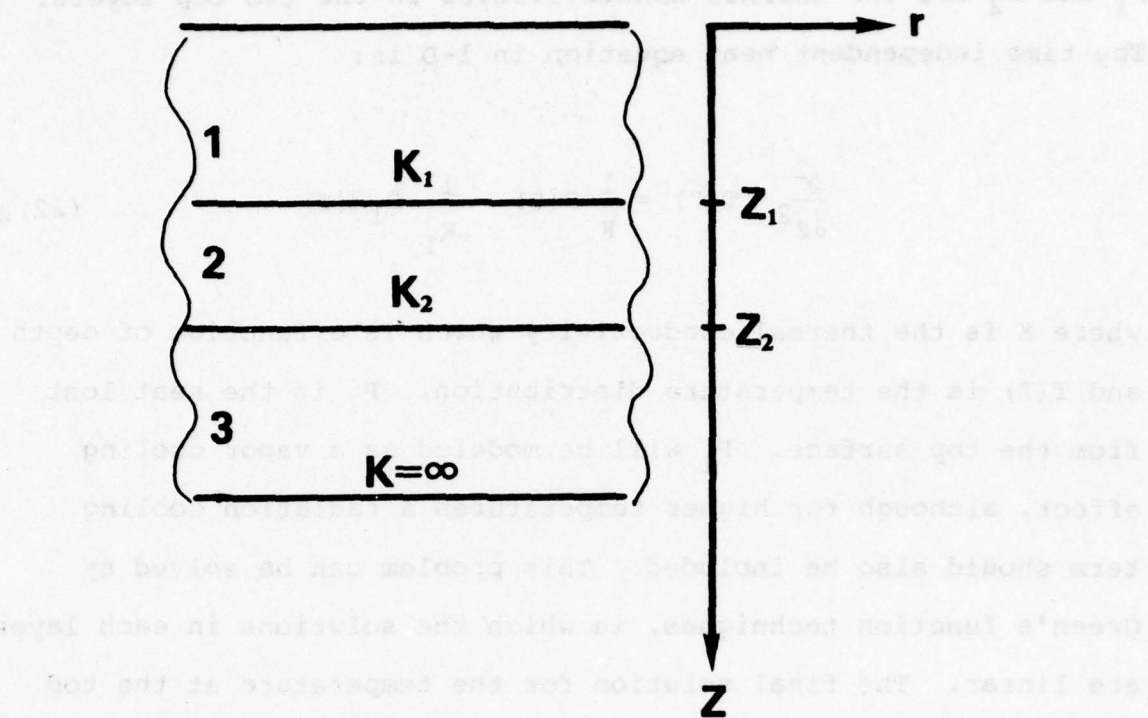
Figure 36. One-Dimensional Heating Model
Geometry

i) One-dimensional Model

In cases where the thickness of the films is small compared
to the electron range and/or electron spot size, one-dimensional
models will provide very good solutions for the temperature rise.
Figure 36 shows the definition of symbols for a three layer heat-
ing model. The source of heat $P(Z)$ (electron beam) is uniform
in r but can vary arbitrarily in depth z. This energy distribu-
tion will be the Grün function in the final results. Film #1
will normally be Se and film #2 a low mass density thermal in-
sulating film such as SiO_2. Film #3 will be the silicon sub-
strate which is taken as an infinite conductivity material for
this model since its conductivity is about 100 times Se or SiO_2.

K_1 and K_2 are the thermal conductivities in the two top layers. The time independent heat equation in 1-D is:

$$\frac{\partial^2}{\partial z^2} T(Z) = \frac{1}{K} P(Z) - \frac{1}{K_1} P_1 \delta(Z) \qquad (22)$$

where K is the thermal conductivity which is a function of depth and $T(Z)$ is the temperature distribution. P_1 is the heat lost from the top surface. P_1 will be modeled as a vapor cooling effect, although for higher temperatures a radiation cooling term should also be included. This problem can be solved by Green's function techniques, in which the solutions in each layer are linear. The final solution for the temperature at the top surface is:

$$T(0) = \int_0^{Z_2} dZ_0 \, P(Z_0) \left\{ \begin{array}{ll} \dfrac{Z_1-Z_0}{K_1} + \dfrac{Z_2-Z_1}{K_2} & Z_0 < Z_1 \\[2ex] \dfrac{Z_2-Z_0}{K_2} & Z_0 > Z_1 \end{array} \right\} + P_1\left(\frac{Z_1-Z_2}{K_2} - \frac{Z_1}{K_1}\right) \qquad (23)$$

ii) Two-dimensional Solution

A second solution is for the case shown in Figure 37. This geometry assumes a semi-infinite medium where the input power is uniformly distributed over a hemisphere of radius a. This is an appropriate approximation when the film thickness is much larger or comparable to the electron range and spot size. A complete time dependent solution for this problem was obtained

66
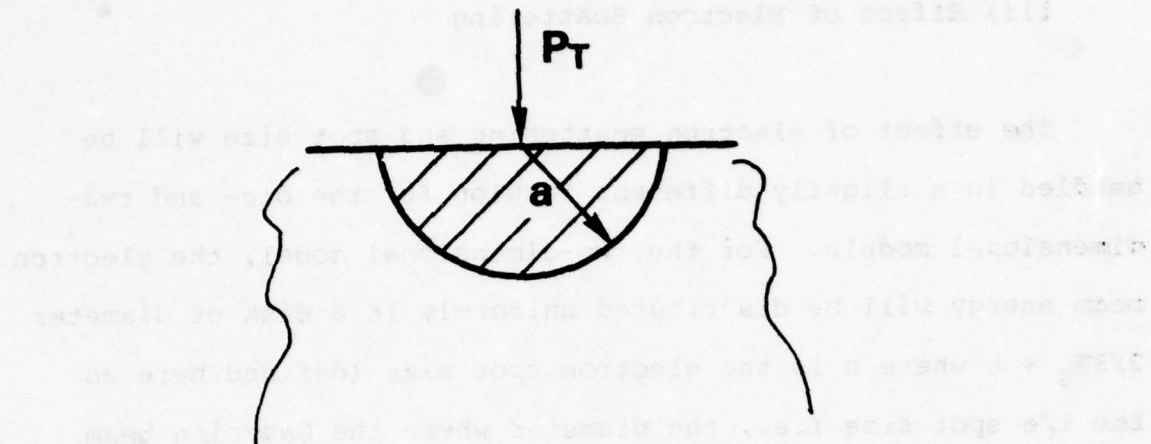
Figure 37. Two-Dimensional Heat-
ing Model Geometry

by Goldenberg [34] . The equilibrium temperature rise at the
surface of the center of the hemisphere T(O) is given by:

$$T(O) = 3 P_T/4\pi Ka \qquad (24)$$

where P_T is the total power into the hemisphere. The thermal
time constant is given by:

$$\tau = a^2/k \qquad (25)$$

where $k = K/C_p$ is the thermal conductivity. For Se $k \sim 4 \times 10^{-3}$
cm^2/sec so that typical thermal time constants for 0.1 μm geometries
are $\sim 6 \times 10^{-9}$ sec. Hence we are justified in treating all calcula-
tions in the time independent limit down to about 3 thermal time
constants of $\sim 2 \times 10^{-8}$ sec. This was already implicitly assumed
in the one-dimensional model discussion.

iii) Effect of Electron Scattering

The effect of electron scattering and spot size will be handled in a slightly different fashion for the one- and two-dimensional models. For the two-dimensional model, the electron beam energy will be distributed uniformly in a disk of diameter $2/3 R_G + b$ where b is the electron spot size (defined here as the $1/e$ spot size i.e., the diameter where the Gaussian beam profile has fallen to $1/e$ of its peak value which corresponds to the spot which includes 60% of the beam current). This is known to be a good assumption and was discussed briefly in the Phase I First Quarterly Report (April 15 - July 15, 1976) and more completely in Reference 35. Hence the input beam power distribution is given by:

$$P(Z) = \frac{(1-F) E_B I_B}{A R_G} \lambda (Z/R_G) \tag{26}$$

where E_B is the beam energy, I_B the total beam current, f the energy backscatter fraction discussed earlier, $\lambda (q)$ the normalized Grün function Eq. 16 and $A = \pi/4 \; (2/3 \; R_G + b)^2$ is the area of the film heated by the beam.

Equation 26 can be generalized for the multilayer problem as follows:

$$P(Z) = \begin{cases} \dfrac{(1-f) E_B I_B}{R_1 A} \; \lambda \; (Z/R_1) & Z \le Z_1 \\[3mm] \dfrac{(1-f) E_B I_B}{A R_2} \; \lambda \left(\dfrac{Z_1}{R_1} + \dfrac{Z-Z_1}{R_2} \right) & Z \ge Z_1 \end{cases} \tag{27}$$

where R_1 and R_2 are the Grün ranges in films 1 and 2 respectively. This is a reasonable assumption that was previously discussed in connection with the determination of the milled Se thickness using electron beam diode signals.

For the two-dimensional model the input beam power P_T is given by:

$$P_T = (1-f) E_B I_B \qquad (28)$$

and the radius a of the heated area by:

$$a^2 = \frac{1}{2} (2/3R_G+b) \, R_G \qquad (29)$$

Equation 29 is the geometric average of the depth of beam penetration R_G and the lateral radius of the heated volume $(2/3R_G+b)/2$. These two temperature models define the extreme cases for the heating model. Typically the one-dimensional model conditions will be well satisfied near the bottom of a milled hole. As a criteria for the transition between the models we require that the temperature at the surface, as a function of film thickness z_1, be continuous. This typically produces a transition between the two models for $z_1 \sim 2/3R_1$. This is a reasonable way to join the two models that produces a slightly high estimate of the surface temperature in the transition region. Hence the milling rates will be slightly optimistic.

69

iv) **Milling Model**

In order to treat the milling process new depth variables
are defined as follows: Z is the depth of milled film #1 relative
to the initial thickness. Let Y_1 and Y_2 be the thicknesses of
the initial layers 1 and 2. Then $z_1 = Y_1 - Z$ and $z_2 = Y_2 + Y_1 - Z$.

Using Equations 27 and 23 the one-dimensional model for
the surface temperature T_O can be expressed as

$$T_O = \frac{I_B E_B (1-f)}{\frac{\pi}{4}(\frac{2}{3}R_1+b)^2} \left\{ \frac{-R_1}{K_1} F(z_5) + \left(\frac{z_1}{K_1} + \frac{z_2-z_1}{K_2} \right) H(z_5) + G \right\} -P_1 \frac{z_1}{K_1} + \frac{z_2-z_1}{K_2}$$

(30)

$$G = - \frac{R_2}{K_1} \left[F(z_6) - F(z_5) \right] + \frac{z_2}{K_2} \left[H(z_6) - H(z_5) \right] \qquad \alpha R_1 > z_1$$

$$G = 0 \qquad\qquad\qquad \alpha R_1 \leq z_1$$

where H and F are particular integrals of λ :

$$H(q) = \int_O^q dy\lambda/y = \sum_{i=1}^4 a_{i-1} \frac{q^i}{I}$$

(31)

$$F(q) = \int_O^q y dy\, \lambda(y) = \sum_{i=2}^5 a_{i-2} \frac{q^i}{I}$$

(32)

$\alpha = 1.1$ is the maximum extent of the normalized Grün function λ and

$$Z_5 = Min(Z_1, \alpha R_1)$$

(33)

70

$$Z_6 = \text{Min}(Z_2, \, \alpha \, R_2 + Z_1 \, (1 - R_2/R_1)) \tag{34}$$

The P_1 term is the power density lost to heat of vaporization. This can be expressed as:

$$P_1 = J_v \, \Delta \, H_v \, \frac{\rho_1}{M_1} \tag{35}$$

where J_v is the evaporation flux in cm/sec of solid material and $\Delta \, H_v$ the heat of vaporization joules/g-atom, and P_1 and M_1 the mass density and g-atomic weight of the evaporating layer. The diameter of the evaporating region is effectively obscured in this treatment by the way the surface temperature is calculated. Actually, only the milling of the center of the heated region is treated correctly. Equation 35 assumes that the entire heated area of diameter $\sim (2/3R_1 + b)$ is evaporating at the same rate. Actually the edges will evaporate somewhat slower so this estimate of the heat lost to vaporization is somewhat too large.

Since P_1 in Eq. 35 depends on the surface temperature T_o through the dependence of J_v on T_o, T_o must be determined by iteration. In the computer program Eqs. 35 and 30 are solved for T_o by Gaussian iteration. The temperature converges to within 0.3% in three iterations.

The milling depth Z as a function of time is determined by integration of the milling rate equation 36

$$Z(t) = \int dt \, \frac{\partial Z}{\partial t} = \int J_v \, (T_o) \, dt \tag{36}$$

71

The time step size Δt for the integration is adjusted so that the incremental milling depth ΔZ per time increment is never larger than 0.003 of the first film thickness. This was verified to give good convergence of the integration.

RESULTS

Figure 38 shows a typical output of the calculation. For the moment ignore the experimental points and the dotted curves. The vertical axis is the amount of milled depth versus writing time per spot. Figure 39 shows the surface temperature versus milled depth. This is not the temperature profile in the film but a plot of the surface temperature as a function of milling depth. The region of constant temperature is the region in which the two-dimensional model is applied. The top curve is the surface temperature without the effect of heat of vaporization cooling and the lower curve is the actual temperature during milling. Note that the moderate effect of vapor cooling is ~20% as previously estimated.

The solid curve in Figure 38 is for 100 nA beam current and corresponds approximately to the experiment described in the experimental results of Table 1. The two dotted curves are similar calculations for 50 and 200 nA beam currents. This shows the very strong dependence of the writing rate on beam current due to the strong dependence of vapor pressure on temperature. Three sets of experimental points are shown for 140, 70, and 50 nA beam current. The 140 and 70 nA data comes from Table 1

72

while the 50 nA data is based on estimates of the writing depths
in the secondary emission micrograph in Figure 40. In all cases
the beam voltage was 16 keV and well focused to ~ 0.1 μm. Because
of the large amount of electron scattering at 16 keV the exact
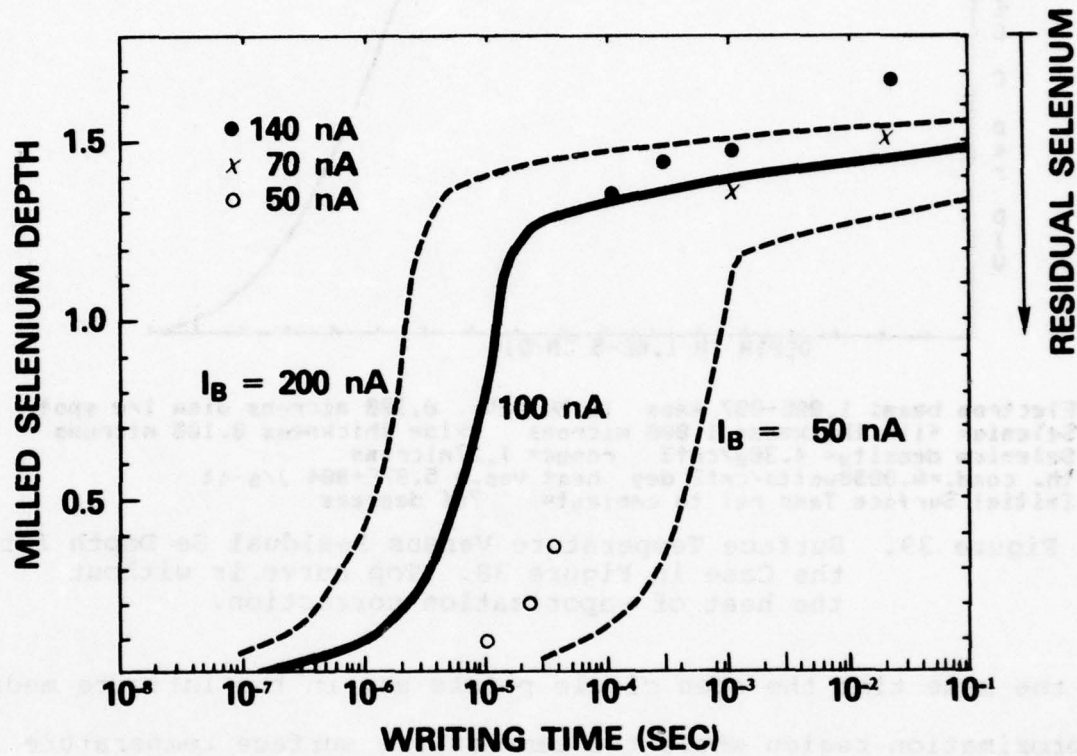
Figure 38. Milling Depth Versus Time Calculated Using
Milling Model

spot size is not important since electron scattering determines
the heated volume. Note that for writing times less than 10^{-3} sec
there is excellent agreement between model and experiment. The
two regions corresponding to the two temperature models can be
clearly distinguished. The solid and cross points for long dwell
times are in the region of the one-dimensional model where the
temperature rise is limited by heat flow to the substrate, while
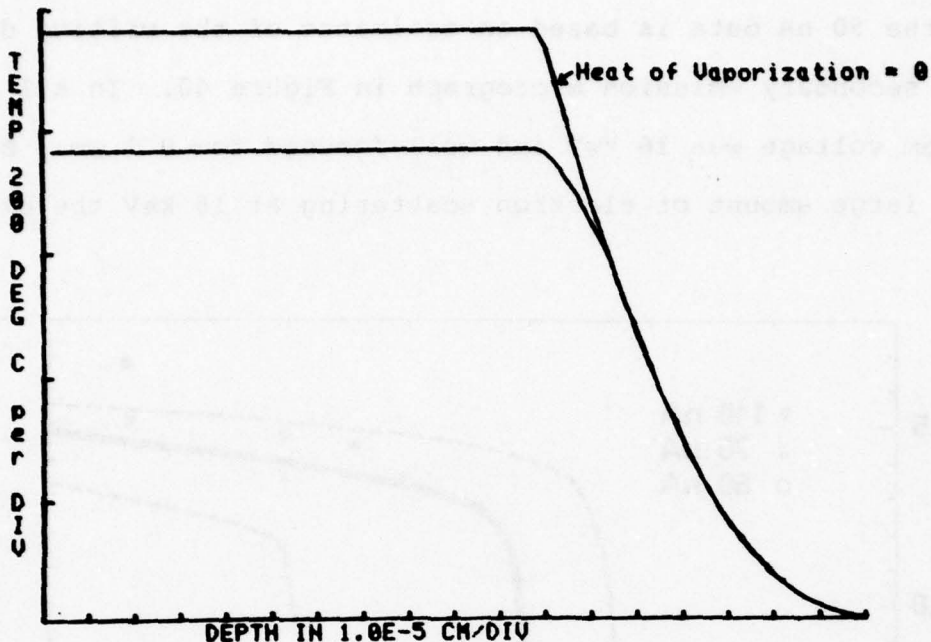
Electron beam: 1.00E-007 Amps   16.00 keV   0.100 microns diam 1/e spot
Selenium film thickness 1.800 microns   oxide thickness 0.100 microns
Selenium density= 4.30g/cm†3   range= 1.27microns
th. cond.=0.0050watts/cm†2 deg heat vap.= 5.97E+004 j/g-at
Initial Surface Temp rel to ambient=   766 degrees

Figure 39.   Surface Temperature Versus Residual Se Depth for
             the Case in Figure 38. Top curve is without
             the heat of vaporization correction.

at the same time the open circle points are in the infinite media

approximation region where the temperature surface temperature

is independent of film thickness and is determined by the thermal

conductivity of the Se film.

As can be seen, the agreement is very good. A further improve-

ment could be obtained by multiplying all of the calculated surface

temperatures by about 1.3 since in all cases the data is better fit

by a beam current about 1.3 times larger than measured. The small

difference between theory and experiment is either due to the ap-

proximate thermal models used or to a lower thermal conductivity

within the range of published values. Since the error is such as

74
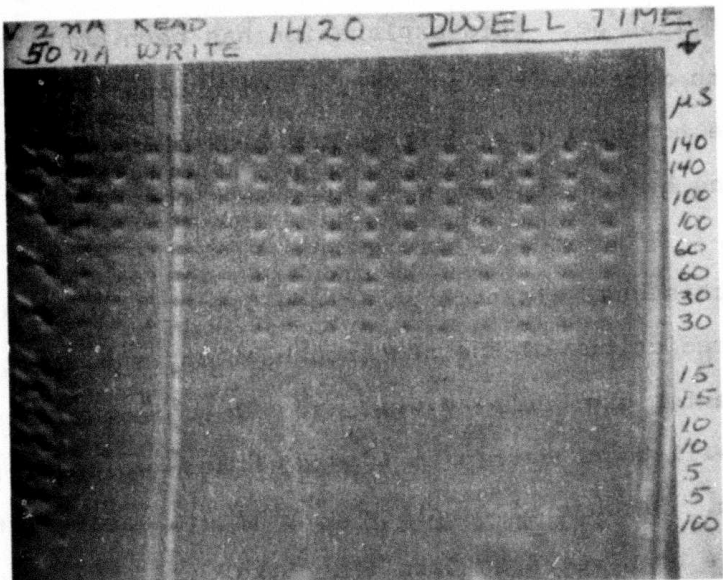
Figure 40.   SEM Secondary Image of
              Writing on 1.8μ Se at
              50 nA and 16 keV for In-
              dicated Dwell Times

to overestimate the required beam current no further corrections
or refinements will be attempted at this time.

Note that the model deviates from experiment at long dwell
times. This is due to melting and flow of the film. The melting
temperature is 200 $^\circ$C which is a factor of 3 below the temperature
required for rapid vaporization. Observations of the Se film
in the SEM under raster scan conditions show that as the Se film
is raised above its melting temperature by the beam it tends
to wet and flow towards the region last hit by the electron beam.
Hence, if the beam dwells for a long time on one spot molten
material at the bottom of the milled hole will flow up the side

of the walls increasing the milled depth. The observed flow rates are very slow. This is consistent with the very high viscosity of molten Se. This explanation has been confirmed by writing with much lower beam currents with power sufficient only to melt the top surface. Melting and flow of the film to the sides of the heated region in ~1 msec were observed.

With this justification it is now appropriate to apply the model to predictions of the required beam current, spot size, and voltage for high density writing. To achieve 0.1 µm-bit sizes, it will be necessary to produce heated volumes of dimension 0.1 µm. Because of electron beam lateral scattering, this will require beam voltages less than 5 keV and spot sizes slightly less than 0.1 µm. For this reason the model calculations described in the remainder of this section concentrate on parameters in this region. Figures 41 through 45 show some applications of the model to such high density writing conditions. All of the relevant parameters can be read in the headings. The total diameter of the heated region will be approximately the spot diameter + 0.66 times the electron range in Se. The election range in Se is indicated in the heading.

Figures 41 and 42 show the milling behavior for a 3 keV electron beam on a 0.03 µm thick Se layer with 0.05 µm of oxide for thermal isolation. A beam current of 100 nA removes 0.024 µm of Se. The residual amount of Se is 0.06 µm. If a 3 keV electron beam is used for readout of this milled region the diode signal gain will be approximately 250. This is 0.3 of the maximum possible

76
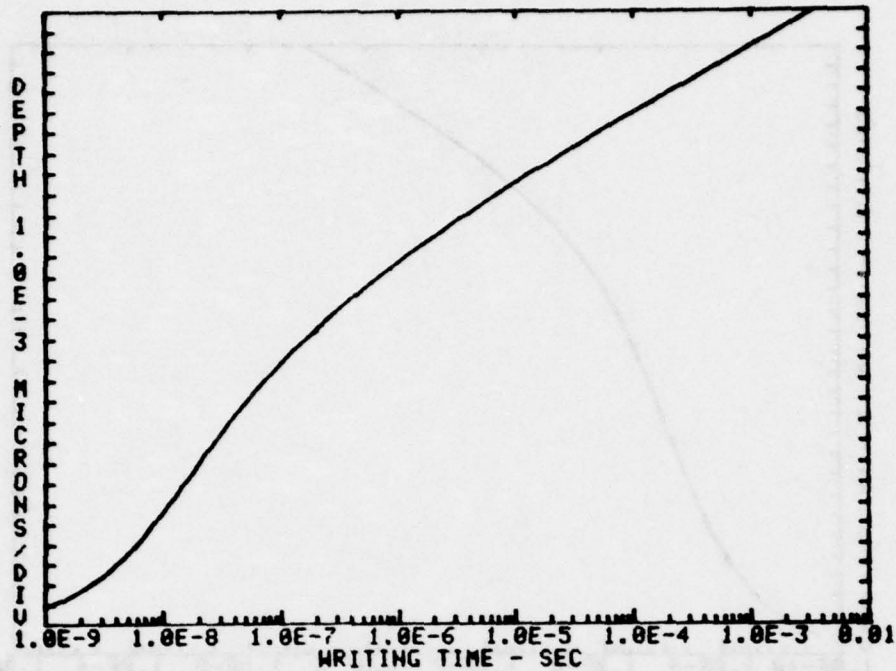
Electron beam: 5.00E-008 Amps   3.00 keV   0.030 microns diam 1/e spot
Selenium film thickness 0.030 microns   oxide thickness 0.050 microns
Selenium density= 4.30g/cm↑3   range= 0.07microns
th. cond.=0.0050watts/cm↑2 deg heat vap.= 5.97E+004 j/g-at
Initial Surface Temp rel to ambient=   1056 degrees

Figure 41.   Milling Calculation for 3 keV, 50 nA 0.03μ Beam
on 0.03μ Se on 0.05μ Oxide

gain that would occur if there were no residual Se and no oxide

isolation layer. Since the diode signal in the unwritten area

would be zero the gain of 250 should provide sufficient signal

for 10 Mhz readout rates with beam currents $\leq$ 10 nA.

Figure 43 shows a similar calculation without the oxide

isolation layer but with the Se film thickness increased from

0.03 to 0.055 μm to provide an equivalent mass thickness of ma-

terial above the diode. At 10^{-7} sec, 0.028 μm of Se is milled

as compared to 0.024 μm for the above case with the oxide isola-

tion layer with the result that the diode signal is 10% higher.

Hence the oxide thermal isolation layer has no clear advantage.

77
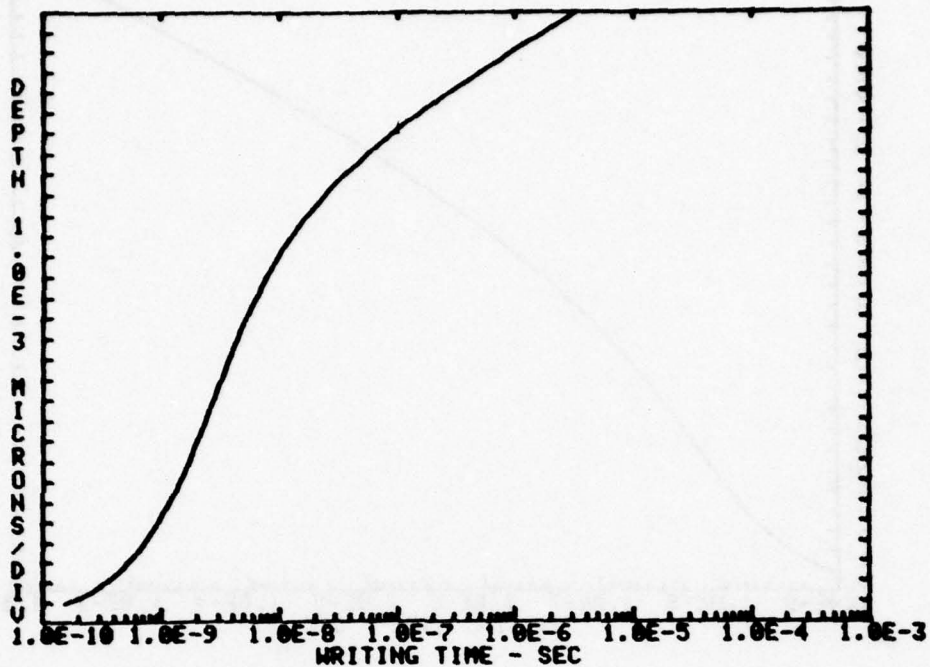
Electron beam: 1.00E-007 Amps   3.00 keV   0.030 microns diam 1/e spot
Selenium film thickness 0.030 microns   oxide thickness 0.050 microns
Selenium density= 4.30g/cm†3   range= 0.07microns
th. cond.=0.0050watts/cm†2 deg   heat vap.= 5.97E+004 j/g-at
Initial Surface Temp rel to ambient=   1431 degrees

Figure 42.   Milling Calculation for 3 keV, 100 nA
0.03µ Beam on 0.03µ Se on 0.05µ Oxide

Of course significant changes in the thermal conductivities of
either the milled or isolation layer would change this conclusion.

Figure 44 shows a similar calculation at 4 keV for the case
of no thermal isolation. The Se thickness has been increased
to 0.11 µm which is the range of the electron beam so that the
diode readout signal at 4 keV will still be approximately zero.

Again 100 nA produces significant milling. Figure 45 shows
the surface temperature profile for the case of Figure 44. Note
the significant effect of the heat of vaporization that reduces

78

Figure 43.   Milling Calculation for 3 keV, 100 nA
on 0.055μ Se

the surface temperature by almost a factor of two.   This is typ-

ical of writing cases where the surface temperature is such as

to produce significant milling in less than 0.1 μsec.   Figure 46

illustrates the effect of heat of vaporization on writing rate.

In the absence of heat of vaporization, doubling the beam current

should increase the writing rate by several orders of magnitude

because of the strong dependence of evaporation rate on tempera-

ture.   This phenomenon is seen to occur for beam currents between

50 and 100 nA.   However, at the higher currents almost no increase

in writing rate is obtained because most of the added power is

going into heat of vaporization.   Hence, the large heat of vapor-

79
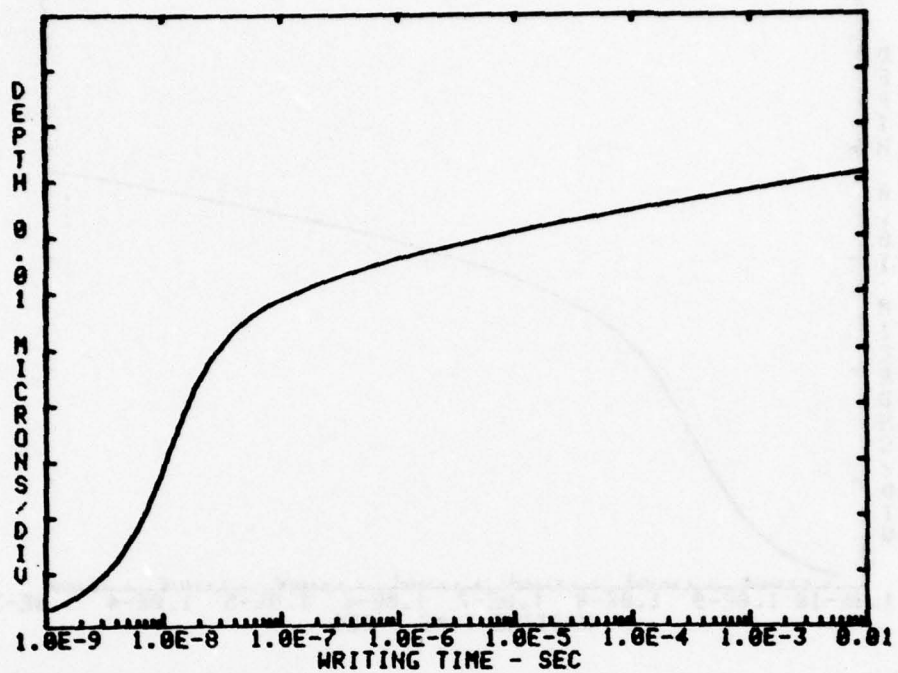
Electron beam: 1.00E-007 Amps   4.00 keV   0.050 microns diam 1/e spot
Selenium film thickness 0.110 microns   oxide thickness 0.000 microns
Selenium density= 4.30g/cm↑3   range= 0.11microns
th. cond.=0.0050watts/cm↑2 deg   heat vap.= 5.97E+004 j/g-at
Initial Surface Temp rel to ambient=   1267 degrees

Figure 44.   Milling Calculation for 4 keV, 100 nA
0.05 μ Beam on 0.11μ Se

ization of Se will effectively limit the writing rate to about

50 MHz for beam currents 300 nA.

Figure 47 shows the milling behavior predicted for a 25 nA,

0.1 μm diameter beam at 5 keV. This is comparable to the best

performance currently available at low voltage in the C&W writing

station. Occasionally higher currents are achieved but at in-

creased spot sizes so that the beam power density is actually

reduced. No milling is predicted for dwell times below 10^{-3} sec.

However, as previously discussed, viscous flow of the molten

80

Figure 45. Surface Temperature During Milling
for Case in Figure 44.

Se occurs for dwell times above 10^{-3} sec making interpretation
of long dwell time experiments difficult.

Note that the predicted surface temperature is just above
the melting temperature of 200 $^\circ$C for Se. Viscous flow writing
is undoubtedly the origin of the writing shown in Figure 31.

RELATION BETWEEN MASS DENSITY AND THERMAL CONDUCTIVITY
FOR THE CHOICE OF AN OPTIMUM MILLING MEDIA

Low thermal conductivity is obviously desired for thermal
milling because the maximum temperature rise is inversely propor-

81
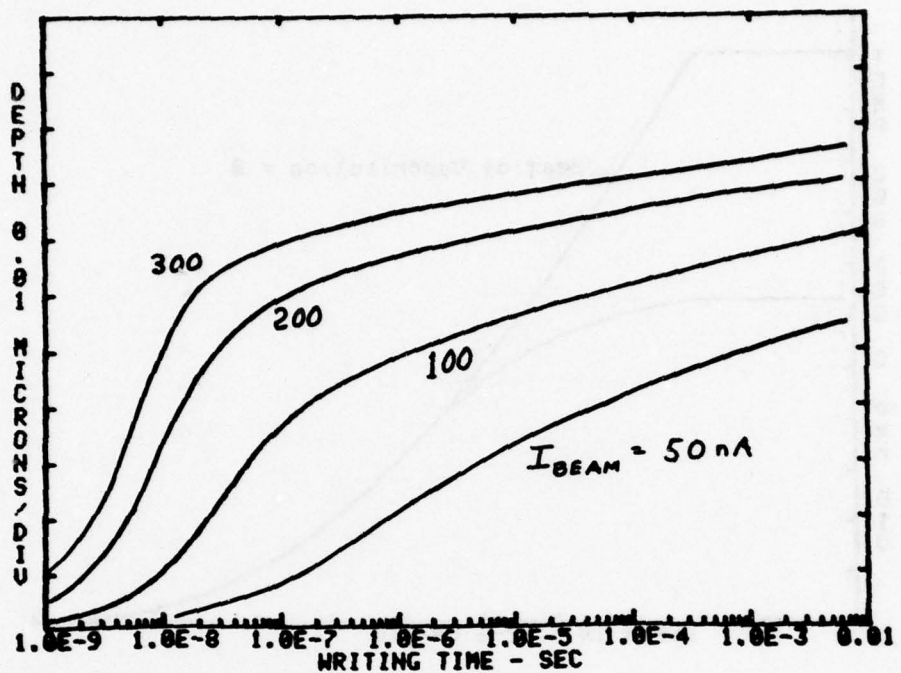
Electron beam: 1.00E-007 Amps   4.00 keV   0.100 microns diam 1/e spot
Selenium film thickness 0.110 microns   oxide thickness 0.000 microns
Selenium density= 4.30g/cm↑3   range= 0.11microns
th. cond.=0.0050watts/cm↑2 deg   heat vap.= 5.97E+004 j/g-at
Initial Surface Temp rel to ambient=   1096 degrees

Figure 46. Milling Calculation for 4 keV, 100 nA
0.01μ Beam on 0.11μ Se

tional to the thermal conductivity, ignoring substrate effects.

However, to some extent, a higher mass density can compensate

for a higher thermal conductivity because the power absorption

per unit depth from the electron beam is greater. Higher electron

beam energies can then be utilized because of the reduced elec-

tron range and lateral scattering in the higher mass density

materials. Based on the two-dimensional heating model discussed

previously, (see Equation 24) the surface temperature rise in

the infinite media approximation is given by:

$$T_{(O)} = 3 \ P_T/4\pi K \ R_G \tag{37}$$

82
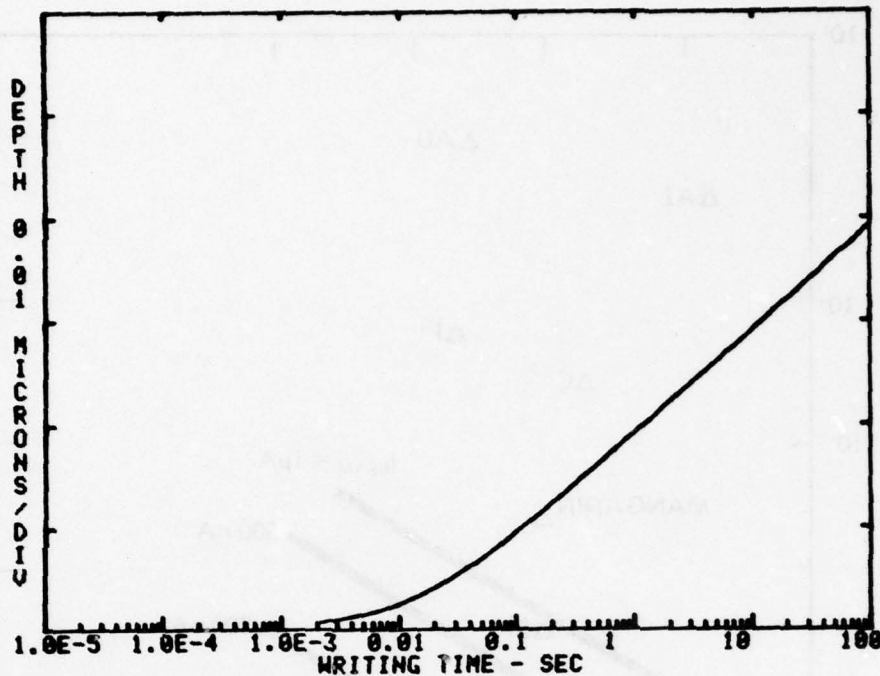
Electron beam: 2.50E-008 Amps   5.00 keV   0.100 microns diam 1/e spot
Selenium film thickness 0.060 microns   oxide thickness 0.100 microns
Selenium density= 4.30g/cm↑3   range= 0.17microns
th. cond.=0.0050watts/cm↑2 deg   heat vap.= 5.97E+004 j/g-at
Initial Surface Temp rel to ambient=   209 degrees

Figure 47. Milling Calculation for 5 keV, 25 nA,
0.1μ Beam

where $P_T = I_B \times E_B$ is the beam power. This ignores spot size

effects so that the radius of the heated volume is taken as the

Grün range R_G. Using Eq. 15 for R_G results in Eq. 38 for the

relation between surface temperature at the start of milling,

mass density, and thermal conductivity. Requiring a surface

temperature of 2000 $^{\circ}$C for rapid thermal milling and $R_G = 0.1\mu$ to

limit the size of the heated and milled region to 0.1μ yields

the curves in Figure 48. Any material has a unique position

on this plot. The solid lines labeled with various beam currents

are the locus of points for which the surface temperature rise

will be exactly 2000 $^{\circ}$C based on Eq. 38 for $R_G = 0.1\mu$.

83
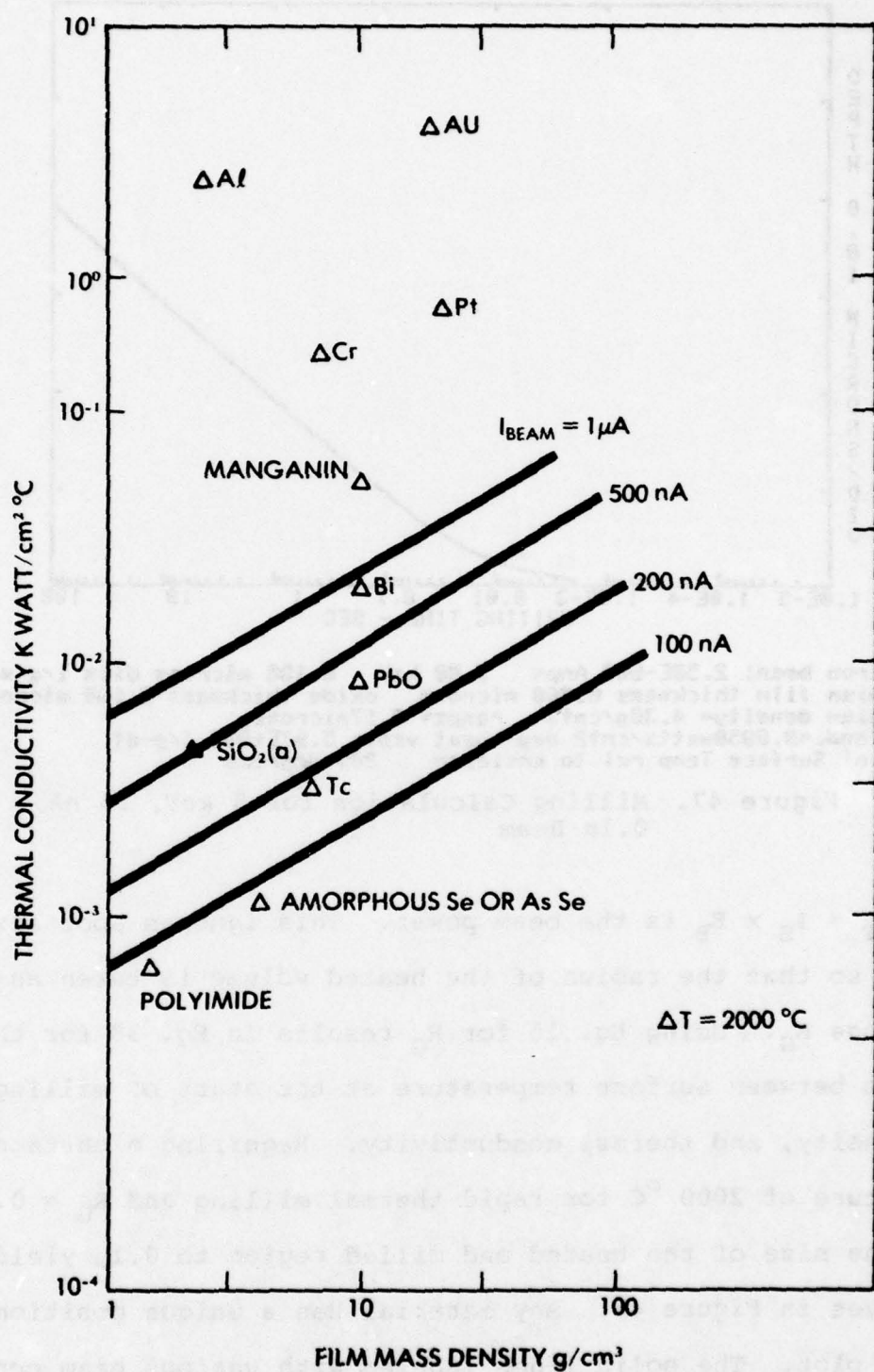
Figure 48. Thermal Conductivity Versus Mass Density Plot for Various Materials Compared to a Heating Model for the Maximum Temperature Rise Achievable in Various Films at 0.1 Micron Written Spot Size

$$\frac{4}{3} \frac{\pi \Delta T_o}{I_B} = \rho^{0.57} K^{-1} \alpha^{-0.57} R_G^{-0.43} \qquad (38)$$

Any material below this line will reach a temperature higher than 2000 °C for the indicated beam current. This graph illustrates that the trade-off between mass density and thermal conductivity goes, approximately as the square root of the mass density and provides a convenient method for comparing the relative writing efficiencies of materials of different mass densities. Plotted on the graph are data points for some common materials. The polyimide point is typical of many polymers. This shows very clearly that even though many polymer films might have slightly lower thermal conductivity than Se-As, their reduced mass density does not make them any more attractive. Of course, if the mass density could be increased by loading with heavy metals without seriously affecting the thermal conductivity this process would be preferable. Metal loading might also reduce the other problem with polymers of electrostatic charging during electron beam readout or writing.

SUMMARY

Electron milling by evaporation has been demonstrated on amorphous Se-As alloy evaporated films. A model for the milling process has been developed which includes the effects of thermal evaporation, solutions to the heat flow equation, and evaporative cooling. This has been compared to writing experiments at 16 and 5 keV on 0.05 and 1.8 μm thick evaporated Se-As films. Good

agreement was obtained between these experiments and the model. Based on the model it is predicted that a 0.05 μm diameter beam at 4 keV and 100 nA or, 0.1 μm diameter beam at 200 nA will be sufficient for 10 MHz milling at 0.1 μm-bit spacing. The above beam specifications assume that all but 1/2 of the beam current is contained in the stated beam diameter. The effect of evaporative cooling is small (20%) but does have a noticeable effect at 10 MHz writing rates. The writing rate will be limited by evaporative cooling and the thermal time constant to about 50 MHz for beam currents less than 400 nA. The Se-As films prepared for these studies are amorphous, uniform and stable, and have the thermal properties expected based on reported measurements on similar bulk materials.

SECTION V

TWO-DIMENSIONAL ELECTRON BEAM HEATING MODEL

INTRODUCTION

The increasing complexity and diversity of the multilayered electron beam targets under examination have resulted in a greater need for a more detailed and precise method of modelling the electron beam heating. The simple analytical approaches can only be used with confidence to model single thick layers or to gain a basic understanding of the temperature increase on beam diameter and thermal conductivity. Our interest in material systems using two and three materials with widely differing densities and thermal properties has made it impossible to predict with any confidence either the distribution of electron beam energy loss or the resulting temperature patterns. The simple computer models described in the first quarterly report have been expanded to a family of programs designed to deal with the variety of needs, each in the most efficient possible way. In addition, a model for electron beam heat loss has been formulated. We believe that this model closely approximates an actual beam even in a target of multilayered materials. The model is based on actual experimental studies and will be described in detail later.

The very small physical dimensions of the heated area and the very short times required for the completion of these processes conspire to make it virtually impossible to examine any sort of

87

details of the process on an experimental level. Thus experimentally, the process either works or it doesn't. The existence of a detailed, time dependent model allows us to understand in detail why a given process either succeeds or fails and what changes are likely to improve it. The model also permits us to try experiments that are presently beyond our capability but that may become practical in the future. Finally, it permits us to vary the large number of parameters involved in the system and to determine the optimum values. In much of the discussion which follows, a particular case will be used as an example. The case chosen is a 600 $\overset{\circ}{A}$ film of selenium over a 400 $\overset{\circ}{A}$ film of silicon dioxide on a silicon substrate. The electron beam is 4 kV at 1 μA and has a 500 $\overset{\circ}{A}$ radius.

MODEL CONCERNS

No model, no matter how carefully formulated, can exactly reproduce nature. It is important to recognize in advance what approximations are being made and attempt to assess their impact on the validity of the results.

1. Bulk values are assumed for all of the material parameters in spite of the very small dimensions and the possibility of size effects.

2. All interfaces, whether between differing materials or between the material and its outer boundaries, are assumed to be without substance even though we know that there is

88

a different physical and electronic structure near these interfaces. This is done simply because we do not know how to treat them properly.

3. The model is a finite difference formulation of the heat flow equation with the electron beam energy loss function providing the heat input. As a part of the solution the device is broken up into finite cell volumes and the heat flow equation is approximated at these points by finite differences replacing the spatial derivatives.

The effect of the finiteness of cell size is measured by reducing cell size and observing the difference. Figure 49 shows the center temperature as a function of depth for our example after 0.2 ns. The open circles of the coarser mesh show that this faster and more economical size is completely adequate for most purposes.

4. The peripheral cells are held at ambient (starting) temperature. This brings a finiteness to the problem and represents a "worst case" temperature rise.

5. The program has been tested by comparison with the "uniform hemisphere" problem which can be done analytically. The results are also constant with varying time interval and cell size.

6. The distribution of energy loss from the electron beam has been studied for a number of materials and we have a high degree of confidence with the present algorithm. One lingering concern is that energy is absorbed by a semiconductor primarily by electron-hole excitation and that the actual phonon

(heat) production may occur at a different location depending
on drift fields, lifetime, etc.

MODEL DESCRIPTION

The most general version of the computer program has [1]
variable cell size [2] checks every cell boundary for continuity
of heat flow in the event of differing adjacent materials [3],
and takes account of the temperature dependence of all thermal
properties. The most useful version has constant cell size. That
is, the cross-sectional area of the ring-shaped cells is fixed.
The cell volume obviously depends on the "ring" diameter, and the
radial (R) and axial (Z) dimensions need not be the same. This
version assumes, at most, two uniform layers of different material
on a still different substrate. It also suppresses the tempera-
ture dependence of the thermal characteristics (including phase
changes) in order to both speed the calculation and permit direct
temperature scaling with beam current. The following, then, is
a description of this most useful program, "HOTSPOT3." A short
user's guide is presented in Appendix A followed by a listing of
the program.

The development of a single general purpose algorithm to de-
scribe the electron beam heating has required considerable effort
and trial. The first step was to solve the problem in a single
medium. Fortunately, an empirical formula for total heat loss
as a function of depth has already been developed and depends
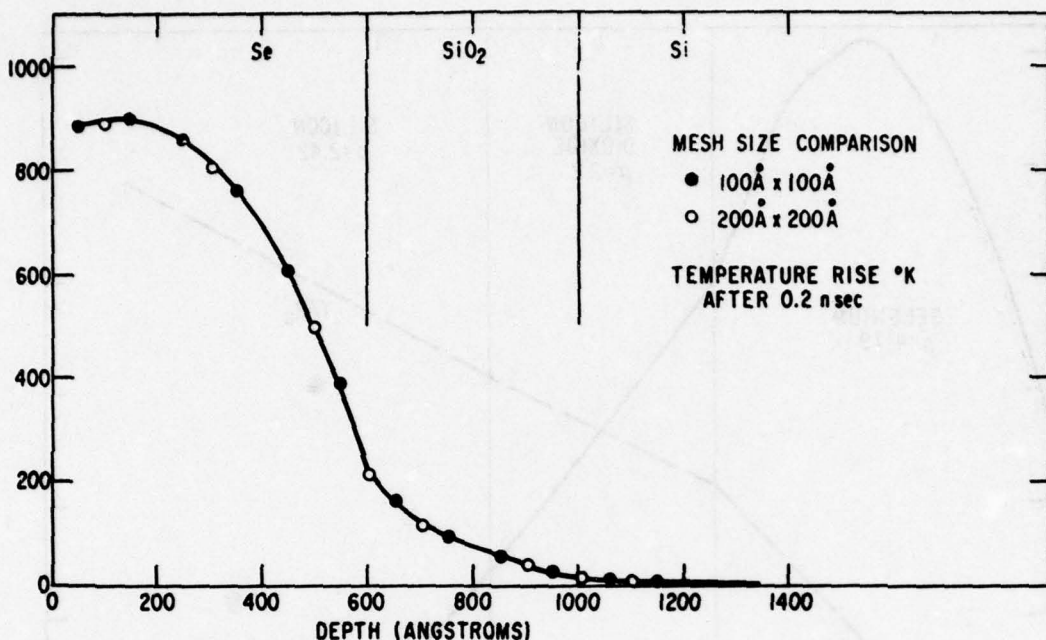
Figure 49.   Axial Temperature as a Function of Depth
Comparing Two Different Mesh Sizes

only on density of the target material and beam energy. A uni-
versal energy loss per unit volume curve can be drawn if the
depth argument is given in distance divided by Grün range, Rg.
In order to extend this universal curve L(Y/Rg) from one material
to another, it was assumed that the normalized depth argument,
Y/Rg, was continuous at boundaries between materials of differing
range. The radial shape of the beam is arbitrarily taken to
be Gaussian at all depths. The only remaining problem, then,
is to decide in what way the width of the Gaussian varies with
depth. After many trials, it was found that best agreement with
the experimental data available was obtained if the width in-
creased linearly at a 30 degree angle from the beam axis.

91
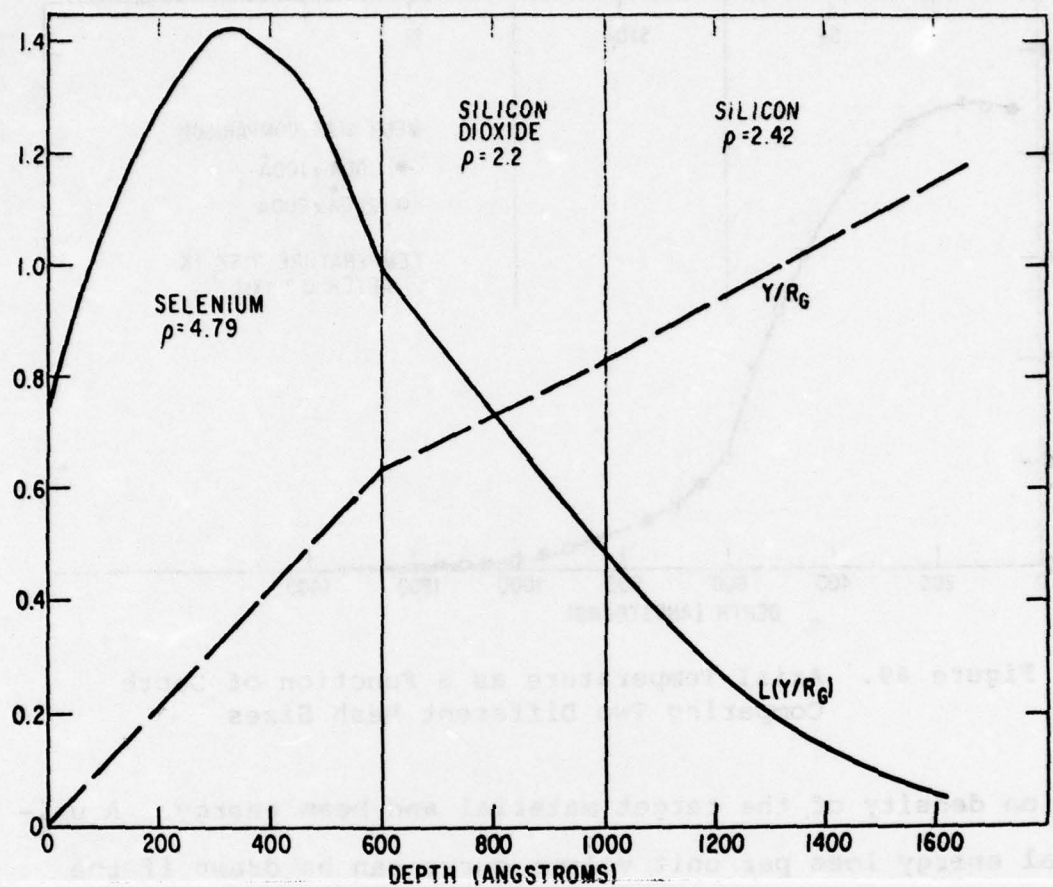
Figure 50. Empirical Universal Energy Loss Function L(Y/Rg)
with Its Argument Showing the Method of Matching
at Interfaces

Figure 50 shows a plot of L(Y/Rg) as a function of depth in
our multilayered example. Also shown is Y/Rg (dashed line). Fig-
ures 51 and 52 show contours of equal energy loss per volume for
beams differing only in energy. These diagrams illustrate one
of the subtleties of this problem and further demonstrate the
need for such a model. One might expect that simply increasing
the beam energy would increase all of the temperatures in the spot
area. However, the increase in volume of the beam pattern with
increasing energy can more than offset the greater available power.
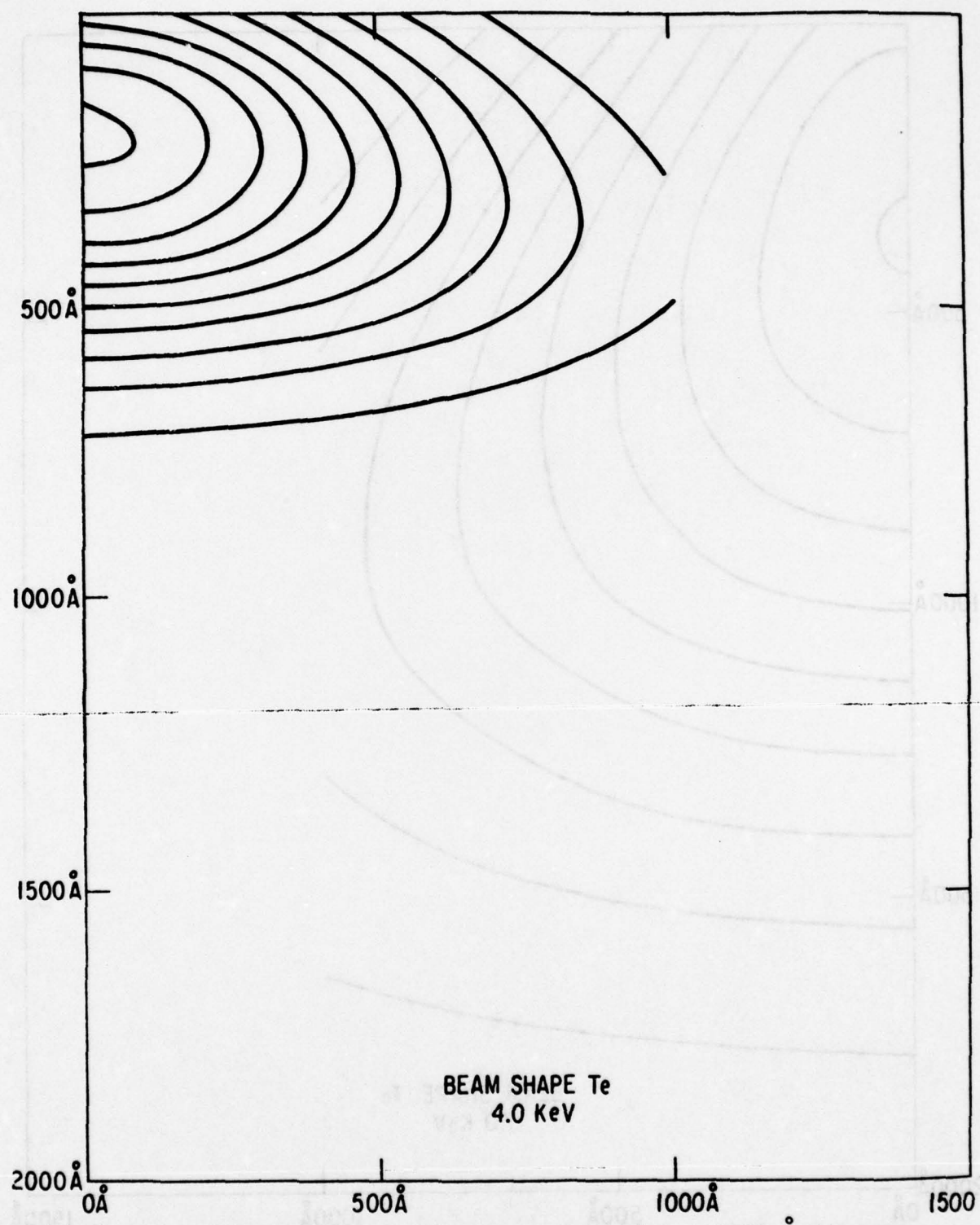
Figure 51.   Contours of Equal Energy Loss for a 1000 Å Diameter
4 kV Electron Beam in Tellurium

93
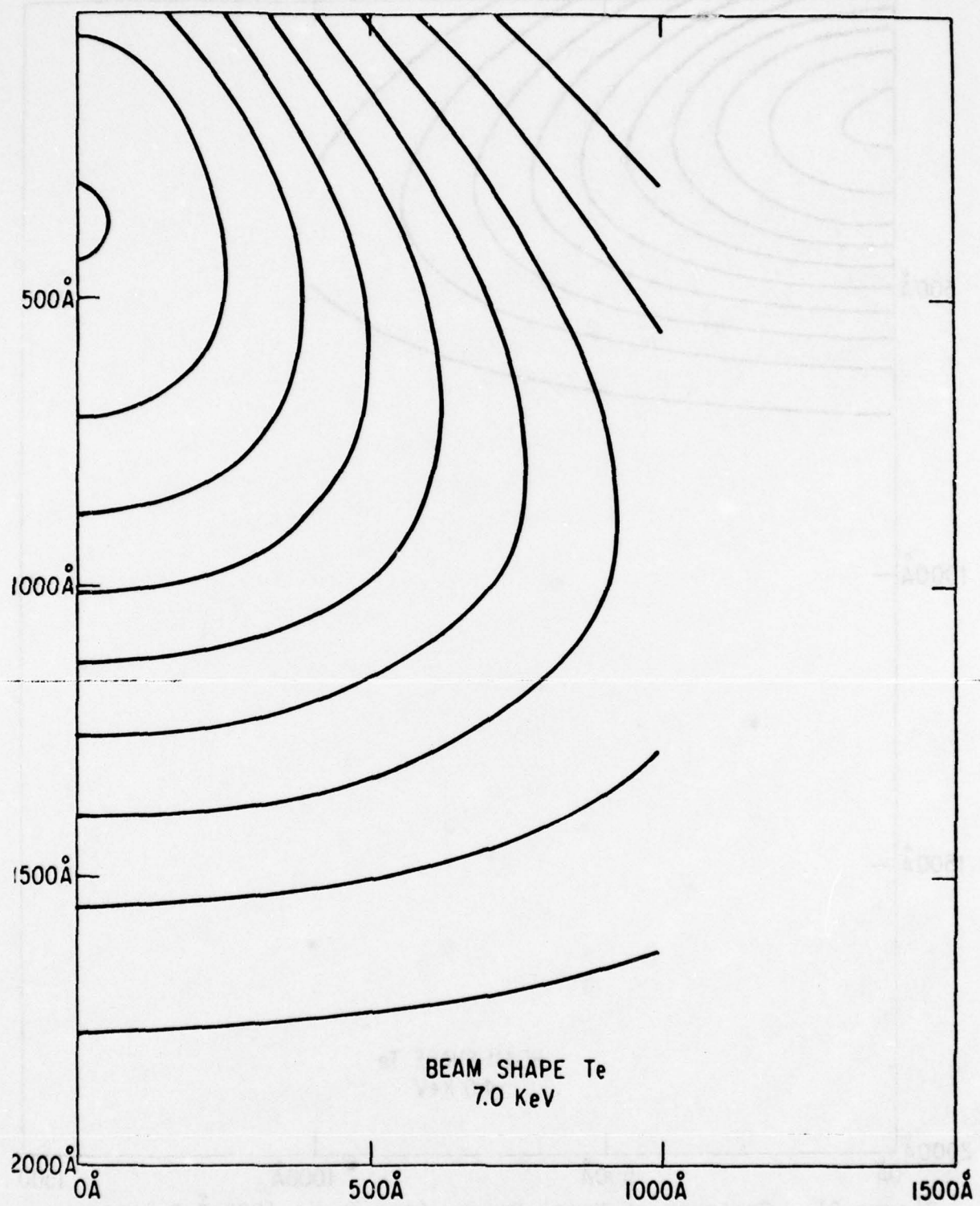
Figure 52.   Contours of Equal Energy Loss for a 1000 Å Diameter
7 kV Electron Beam in Tellurium

94

In fact, there is an optimum beam energy for maximizing the temperature at any given depth. Such matters will become clearer during the discussion of results.

SELECTED RESULTS

Some examples will now be given of uses to which the program has been put. For purposes of scaling convenience, a beam current of one microampere has been used throughout even though this leads to unrealistic temperatures in some cases.

1. It was desired to learn the effect of a thin layer of silicon dioxide between the silicon substrate and a 600 Å selenium film. This could be useful for electron beam milling. The program was run with and without a 400 Å silicon dioxide middle layer. Figure 53 shows the axial temperature as a function of depth after 1.5 ns. The relatively low thermal conductivity of the oxide layer has resulted in a somewhat higher temperature in the selenium. If the program is extended to 4 ns it can be seen from Figure 54 that the effect of the oxide is relatively much greater at longer heating times.

Another concern is the size of the mark made on the surface. To examine this, a family of curves showing the temperature at various depths as a function of distance from the beam axis is shown in Figure 55. Note that the diameter affected may be either larger or smaller than the effective

beam diameter of 500 Å depending on where the vaporization temperature occurs on each curve. In all cases the beam diameter is defined as the e^1 diameter of a Gaussian spot profile.

2. In some larger scale milling experiments, it was decided to calculate the surface heating rate of a 12000 Å selenium film on silicon dioxide using a 16 kV beam. Figure 56 shows the surface (500 Å deep) temperature as a function of time plotted for two different beam radii.

3. In a study of the effect of beam energy and film thickness on the temperature of tellurium films on silicon, the following results were obtained (see Table 4). Over the range considered, the interface temperature for a 600 Å tellurium film on silicon goes through a maximum at a beam energy between 5 and 6 kV. Yet a still higher interface temperature can be reached with a thinner (400 Å) film at 4 kV.

4. Calculations done for gold and aluminum on silicon have also been performed. A 4 kV —Å diameter beam on a 200 Å gold film will raise the interface temperature by 72 °C in 0.2 ns. A 2.5 kV —Å diameter beam on a 465 Å aluminum film will raise its interface temperature by 60 °C in 0.6 ns.
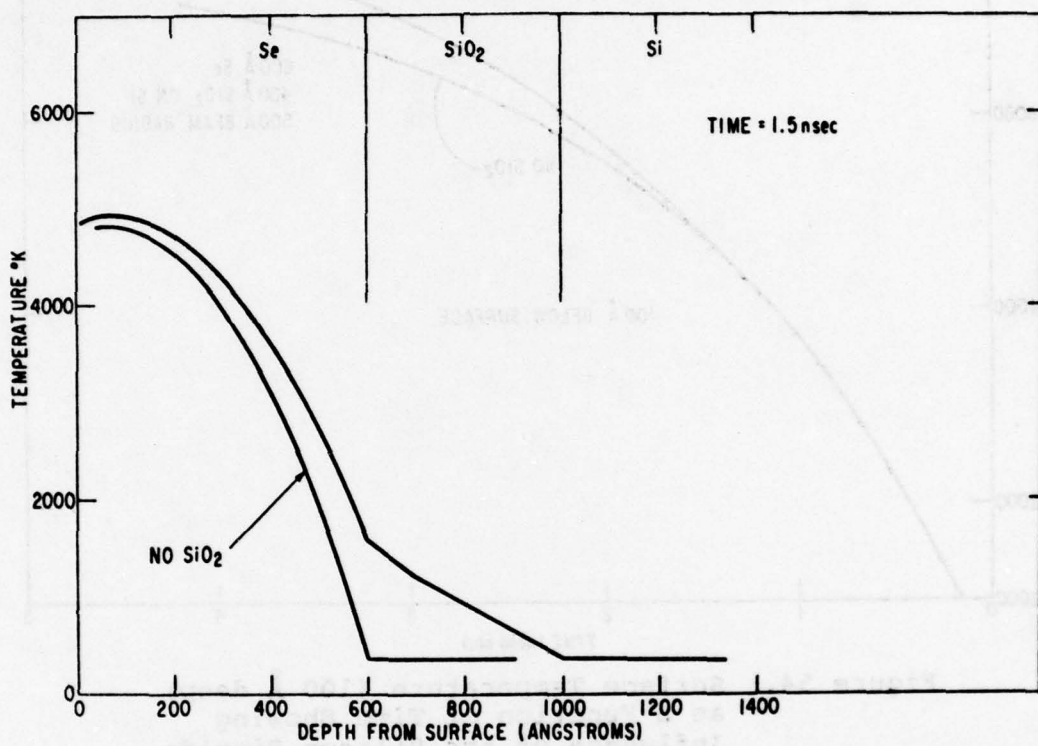
Figure 53. Axial Temperature as a Function of Depth
            After 1.5 ns Showing Influence
            of the Silicon Dioxide Layer
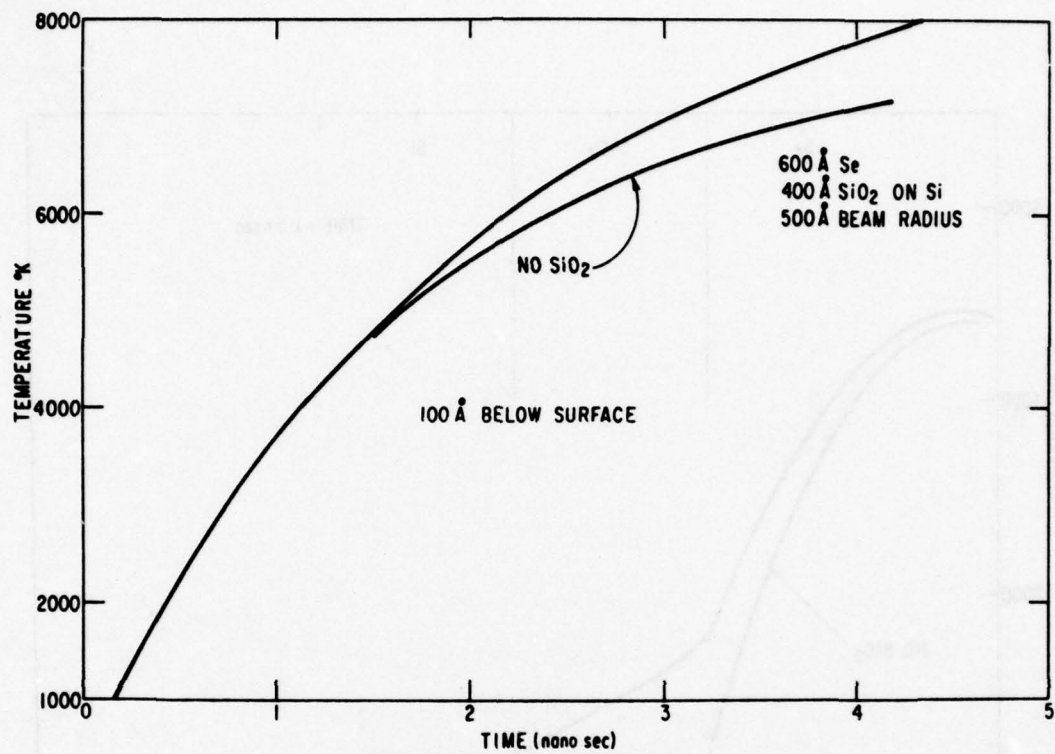
Figure 54.   Surface Temperature (100 Å deep)
as a Function of Time Showing
Influence of the Silicon Dioxide
Layer
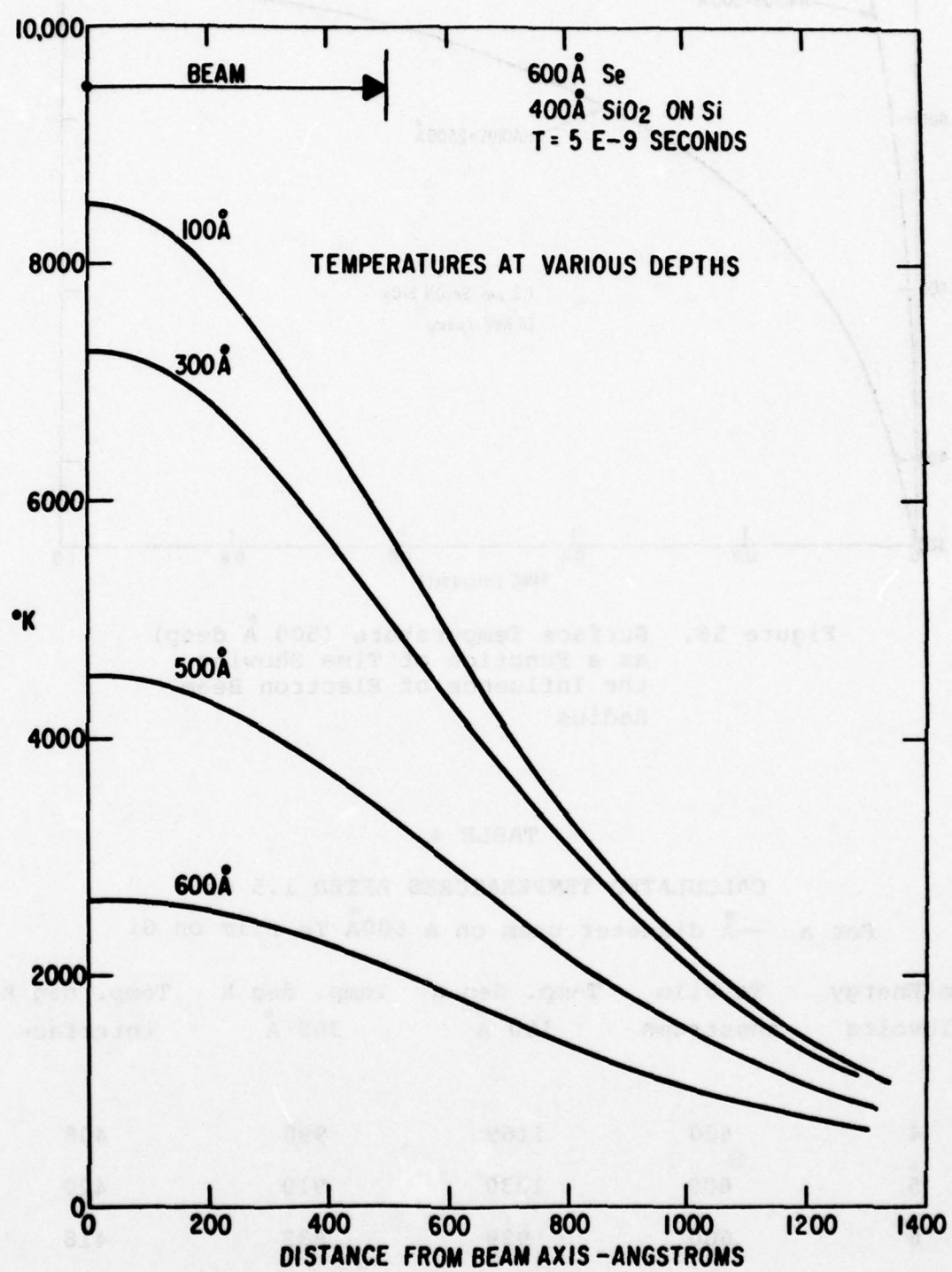
Figure 55. Temperatures Away from the Beam Axis
at Various Depths After 5 ns
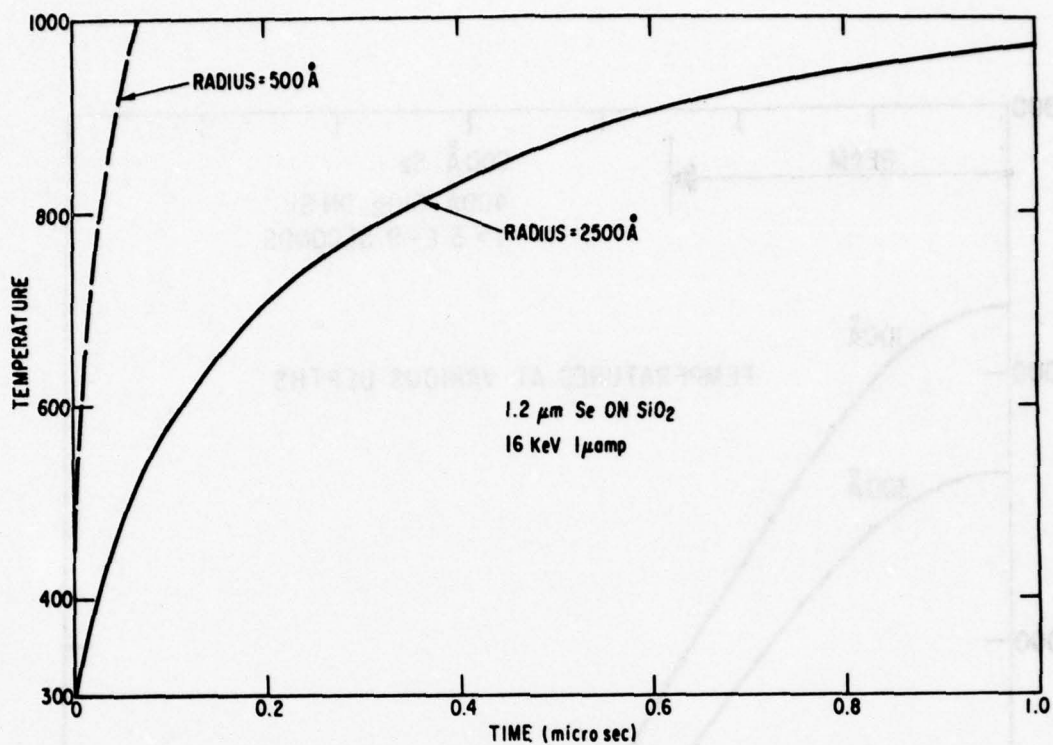
Figure 56. Surface Temperature (500 Å deep)
as a Function of Time Showing
the Influence of Electron Beam
Radius

TABLE 4

CALCULATED TEMPERATURES AFTER 1.5 ns

For a —Å diameter beam on a 600Å Te film on Si

Beam Energy kilovolts	Te Film angstroms	Temp. deg K 100 Å	Temp. deg K 300 Å	Temp. deg K interface
4	600	1169	990	408
5	600	1039	910	420
6	600	939	833	418
4	400	910	674	429

SECTION VI
ELECTRON MICROPROBE ANALYSIS

INTRODUCTION

During the current phase of the Archival Memory Contract, considerable interest in electron beam thermal machining as a recording technique has developed. With this method of recording, a high current finely-focused electron beam is used to machine submicron data sites on the surface of a suitable recording medium. Electron beam thermal machining as a method of recording information is not a new concept in itself and has been previously worked on at GE as well as in other companies. [37/38] Prior efforts in this area tended to be limited in target material and operation due to the low current capabilities of submicron electron probes. A further limitation was the requirement for secondary emission readout. During recent years the thermionic-aided field emission (TFE) electron source has seen significant advances in its development to the point where now it can be considered a reliable high current density source for submicron operation. This source coupled with the development of efficient diode detectors in both the BEAMOS and Archival Memory Programs makes the thermal machining memory concept a much more attractive technology.

A design for a TFE source electron probe capable of one microamp in a 1000 Å spot (90% current diameter) was developed during

101

Phase I of this contract and reported in the Phase I Fourth Interim
Report (January 16 - April 15, 1977. Subsequently, it was learned
that Lee Veneklassen of ETEC, one of the leaders in TFE development,
was developing a similar electron probe. Negotiations began earlier
in this reporting period with ETEC for the purchase of a column
of this type for a research tool. In order for us to better under-
stand the column specifications and its projected capabilities,
an analysis of the microprobe optics was performed under this con-
tract. The analysis is described in this section of the report.

MICROPROBE ANALYSIS

By way of background the column schematic for the electron
microprobe design developed here during Phase I is shown in Fig-
ure 57. As can be seen, the microprobe consists of a thermionic-
aided field emission source with a dual magnetic lens focusing
system. The design relied upon the first lens collimating the
beam and the second lens producing the final image on the target.
In order to obtain low aberrations and therfore much higher current
density, the target plane had to be close to the final lens. There-
fore, prelens double deflection, as indicated in this schematic,
was required. Based on the analysis of this design, the resulting
current versus spot size characteristics as shown in Figure 58
were developed. As seen from this figure, at 4000 V, better than
one microamp of current can be delivered into a 1000 Å spot. The
analytical techniques combine aberrations and geometric spot sizes
in quadrature. Previous experience indicates that this represents

102

a 90% current diameter spot. The proposed ETEC design as published earlier this year 39 is shown in Figure 59, along with experimentally obtained current versus spot size data. In this column the electron gun is an oxygen processed 100 thermionic-aided field emission. A specially designed variable focus electrostatic lens serves as the first lens. The final lens is a standard magnetic ETEC autoscan objective lens with prelens deflection. For the high current density probe it is seen that a slightly converging probe between lenses is used rather than a collimated system as shown in our design. The current versus spot size characteristic, however, indicates that for the high current mode about one microamp of current is achievable in the tenth micron spot diameter. In fact, the whole probe current versus spot size characteristic appears very similar to the Phase I design shown previously in Figure 58. With this data negotiations began with ETEC for a similar electron probe system.

In order that we might better understand the ETEC column design and its specifications, an analysis of the focusing optics was conducted in this Laboratory. Optical properties for the aberration coefficients, focal lengths, etc. were requested from ETEC for their column design. These properties were supplied. Using this data in our analytical programs, the beam current versus spot size characteristic shown in Figure 60 was calculated. The fact that these computations resulted in a probe current of only a few tens of nanoamperes in a 1000 A spot size was totally unexpected and quite perplexing. On the one hand, it was recognized that

103
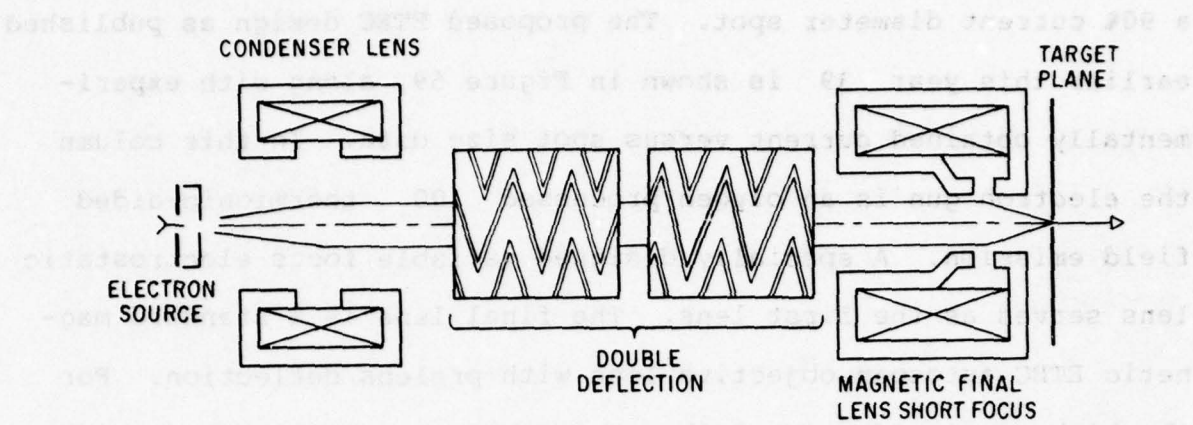
Figure 57. Electron Microprobe Design of Phase I

Veneklassen's data was experimental and thus hard to refute. This
made the calculation procedures used here of some question. On
the other hand, similar calculation procedures have previously
been used in BEAMOS and other programs at General Electric labora-
tories with excellent correlation between experiment and theory.
The major responsibility of this analytical study was then to re-
solve the discrepancy between these initial calculations and the
experimental results published for the column similar to the column
that was in negotiations.

One of the first possible areas for disagreement was noted
to be in the definition of spot size. In the experiments of
Veneklassen, spot size was determined by scanning the beam across
a sharp knife edge. The resulting rise time and current achieved
by scanning across the sharp edge were then correlated with the
scan velocity to result in a given distance measurement for the
15-85% rise time. As previously noted, the spot size for the
analytical work was determined by combining the various spot sizes
due to the aberrations and the geometric imaging of the source

104
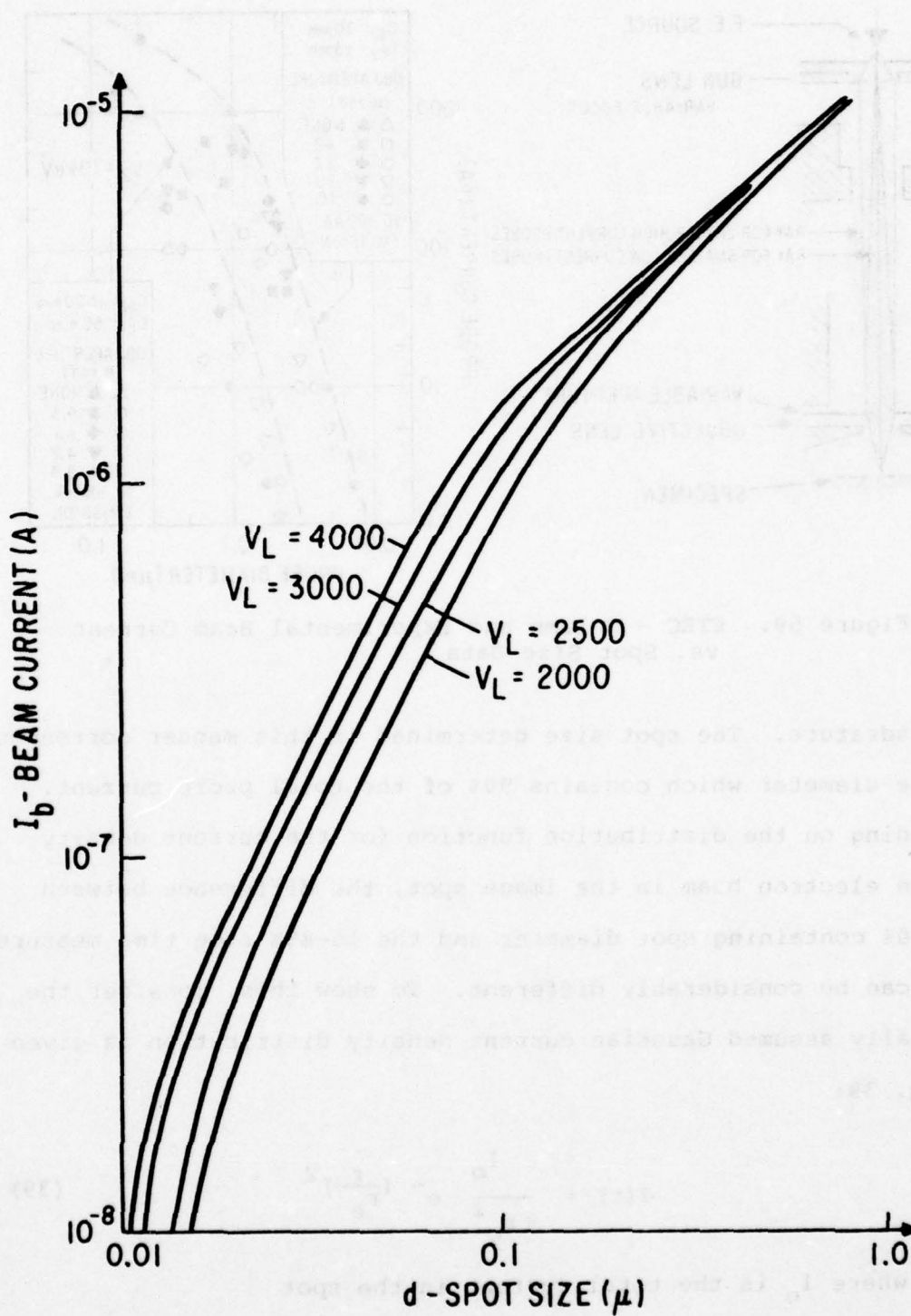
Figure 58. Beam Current vs Spot Size for the Phase I
Microprobe Design
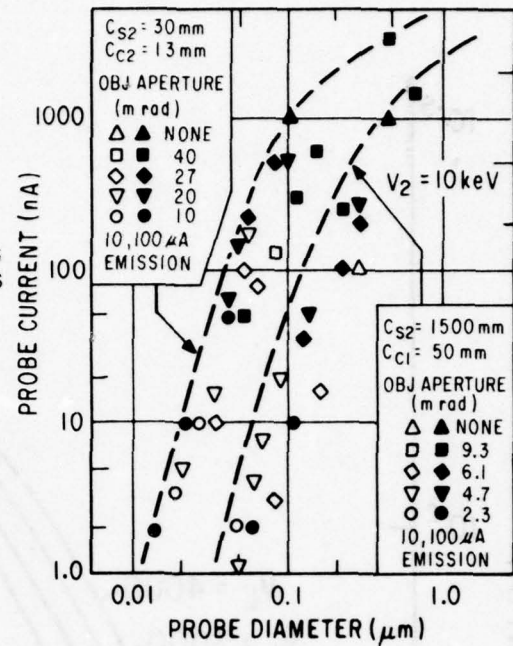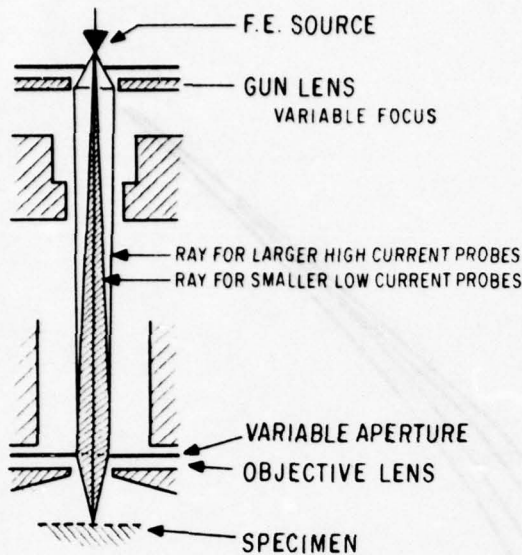
Figure 59.   ETEC - Column and Experimental Beam Current
vs. Spot Size Data

in quadrature.   The spot size determined in this manner corresponds

to the diameter which contains 90% of the total probe current.

Depending on the distribution function for the current density

of the electron beam in the image spot, the difference between

the 90% containing spot diameter and the 15-85% rise time measure-

ment can be considerably different.   To show this, consider the

generally assumed Gaussian current density distribution as given

by Eq. 39:

$$J(r) = \frac{I_o}{\pi r_e^2} \, e^{-(\frac{r}{r_e})^2} \tag{39}$$

where I_o is the total current in the spot

r is the spot radius

r_e is the radius with the beam at $\frac{1}{e}$.

106
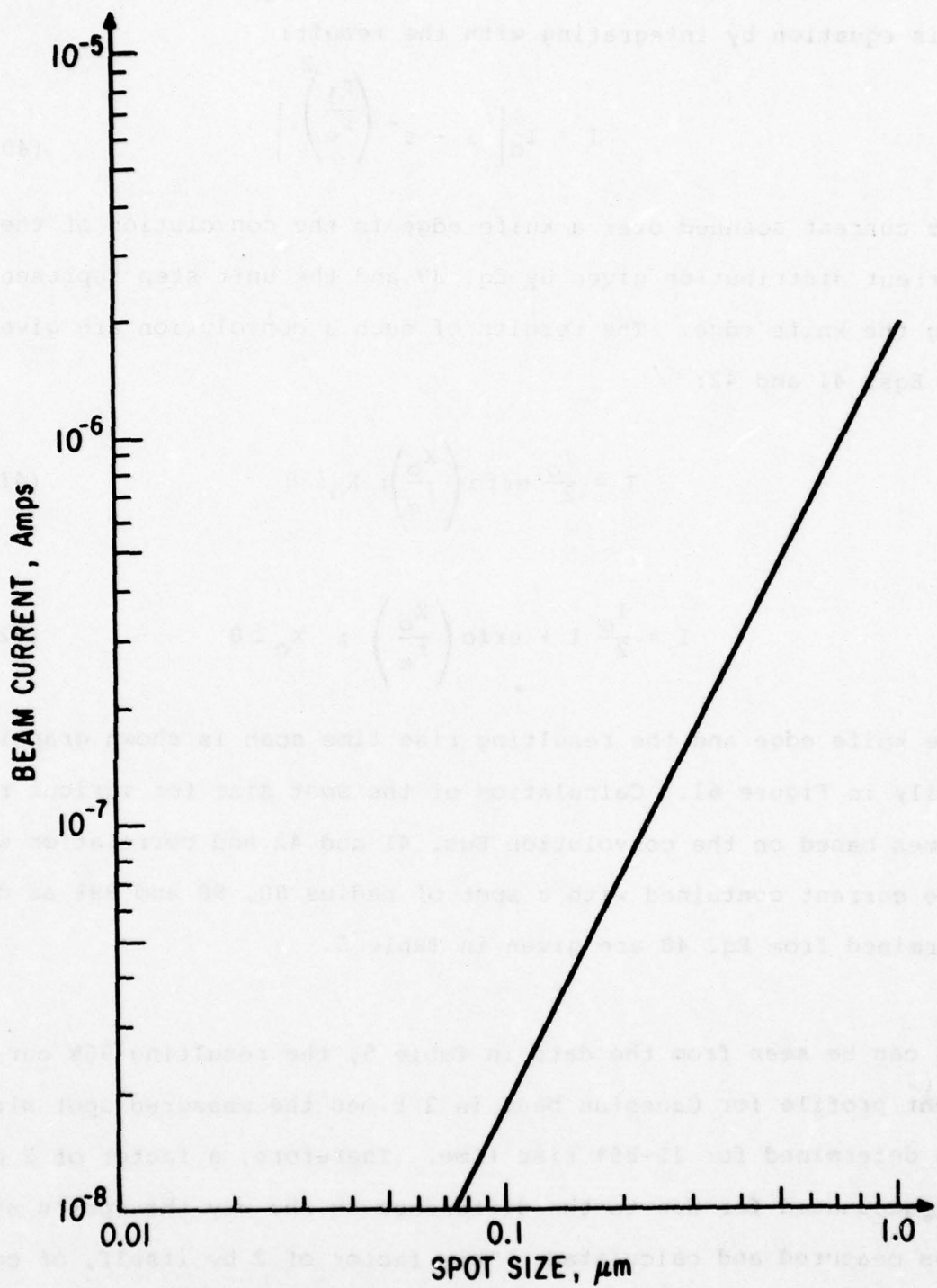
Figure 60. Initial Calculation of Beam Current vs. Spot Size for ETEC Microprobe

The current contained with a radius of spot r_1 can be found from this equation by integrating with the result:

$$I = I_o \left[1 - e^{-\left(\frac{r_1}{r_e}\right)^2} \right] \qquad (40)$$

The current scanned over a knife edge is the convolution of the current distribution given by Eq. 39 and the unit step representing the knife edge. The results of such a convolution are given in Eqs. 41 and 42:

$$I = \frac{I_o}{2} \text{ erfc}\left(\frac{X_o}{r_e}\right); \quad X_o \geq 0 \qquad (41)$$

$$I = \frac{I_o}{2}\left[1 + \text{erfc}\left(\frac{X_o}{r_e}\right) \right]; \quad X_o \leq 0 \qquad (42)$$

The knife edge and the resulting rise time scan is shown graphically in Figure 61. Calculation of the spot size for various rise times based on the convolution Eqs. 41 and 42 and correlation with the current contained with a spot of radius 80, 90 and 99% as determined from Eq. 40 are given in Table 5.

As can be seen from the data in Table 5, the resulting 90% current profile for Gaussian beam is 2 times the measured spot size as determined for 15-85% rise time. Therefore, a factor of 2 can be accounted for due to the difference in the way the spot's size was measured and calculated. This factor of 2 by itself, of course, does not account for the difference between the calculated results using our program and the experimental data furnished by ETEC.

108

TABLE 5
RELATIONSHIPS OF EDGE SCAN VERSUS
% CURRENT DIAMETERS

Edge Scan	$\dfrac{I_{meas}}{I_{total}}$	% Current Radius to Measured Radius		
x% to 1-x%		r_{80}/r_{meas}	r_{90}/r_{meas}	r_{99}/r_{meas}
1-99	0.932	0.77	0.93	1.31
5-95	0.740	1.10	1.31	1.85
10-90	0.563	1.40	1.67	2.36
15-85	0.413	1.74	2.08	2.95
20-80	0.302	2.11	2.53	3.58

Therefore, the search continued for discrepancies between the calculated and experimental results. Another discrepancy was found in the mode of operation of the two lens system. Our two lens analytical programs are set up for the special case of a parallel beam between lenses. The reason for this is that it is well-known that the aberration coefficients for a given lens are polynomial functions of the magnification. Therefore, the lowest aberration coefficients occur when the lenses are operated with either the image or the object at infinity. A design optimized for this condition therefore should result in more current per unit spot. In talking with Veneklassen, he indicated that his first lens was optimized for the thermionic emission gun; however the final lens was the objective lens from an ETEC autoscan SEM and not necessarily optimized for the field emission cathode.

109

SCAN

CURRENT COLLECTOR

X_0

I/I_0

1

1-X %

X %

$d_{X \to 1-X \%}$

TIME
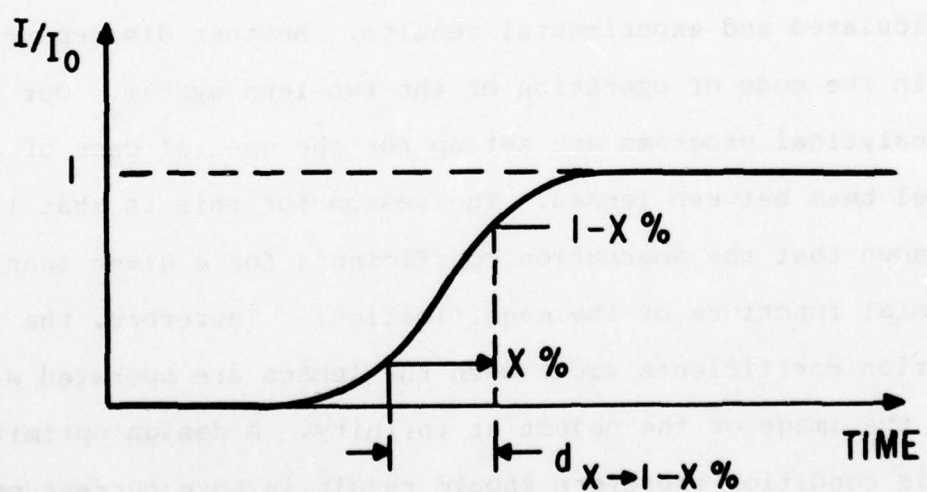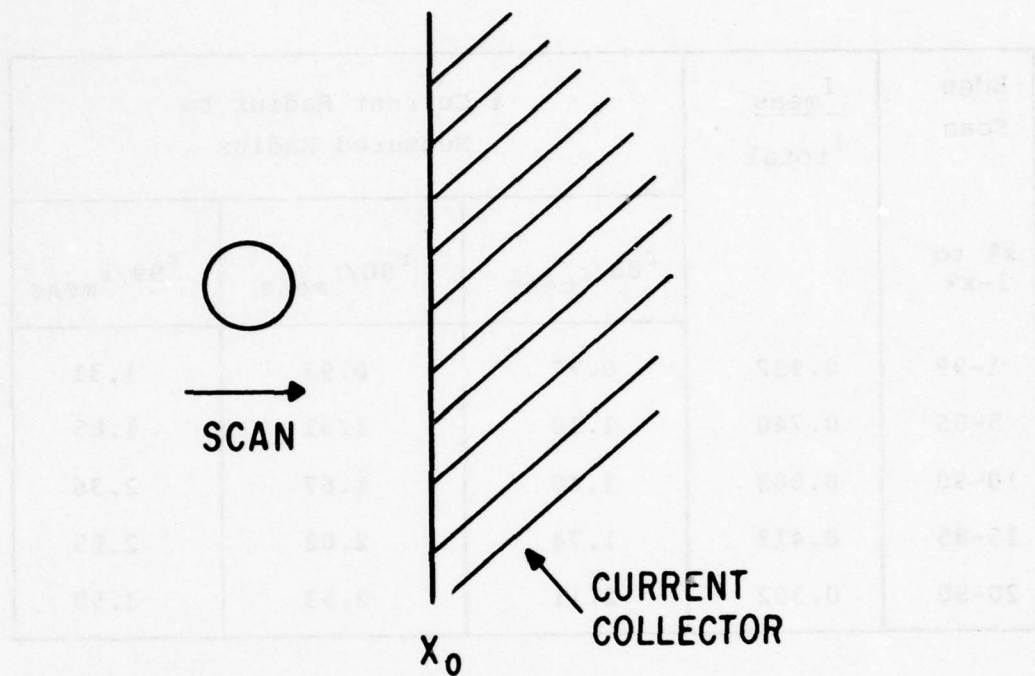
Figure 61. Edge Scan of an Electron Spot

His analysis therefore indicated that running the beam with either
a slightly diverging or converging beam between lenses gave more
current per unit spot. In order to study this effect, some of
our existing programs were modified to allow calculation for a
nonparallel beam between lenses. At present, all the CR&D optical
programs are for electrostatic lenses and therefore the exact case
of a first electrostatic lens and second magnetic lens of the
Veneklassen probe could not be treated. We were able, however,
to choose two electrostatic lenses that came close to the properties
of the electrostatic and magnetic lens of the Veneklassen system
for analytical purposes. In this manner we could study the effects
of operating with the beam parallel or nonparallel between the
two lenses. The results of beam current versus spot size calcula-
tions for this all electrostatic lens system are shown in Figure 62.
Shown on this figure are cases where the beam is parallel between
lenses and slightly diverging and slightly converging for the case
when the final lens is not optimized with the first lens. Also
shown on this curve is parallel beam case where the final lens
was optimized using the techniques developed in previous ion column
design work. From the figure, it can be seen that for a nonoptimized
lens system a slightly diverging or converging lens yields more
current per unit spot than the parallel beam case. This is in
support of Veneklassen's claim. However, the curves also show
that if the final lens is optimized for parallel beam operation
with the first lens then a significant increase in current per
unit spot can be achieved with this mode of operation. This pro-
cedure bears out our previous concept of the proper mode of opera-
tion for a two lens system. These calculations show that another

111

factor of two in beam current per unit spot size in the tenth micron spot size region could be achieved by running the nonoptimized lens system with the beam slightly diverging or converging between the two lenses.

In further discussions with Lee Veneklassen it was found that there was a difference in the definition of the chromatic aberration coefficient between his usage and our program. Veneklassen defines the chromatic aberration coefficient:

$$r_C = 1/2 \ C_C \ \frac{\Delta V}{V} \ \alpha \qquad (43)$$

whereas the definition of chromatic aberration coefficient used in our programs is:

$$r_C = C_C \ \frac{\Delta V}{V} \ \alpha \qquad (44)$$

As can be seen, the chromatic aberration coefficient is a factor of two larger by our definition. What this means is that in using the chromatic aberration coefficient supplied to us by Veneklassen it had to be divided by two in order to fit the definition for our program. This could prove significant since as can be seen from the calculated beam current versus spot size curves, the beam is operating in the chromatic limit in the tenth micron region.

All of these correction factors were incorporated in our optics analysis program and the beam current versus spot size for the Veneklassen optical data was recalculated. The results are

112
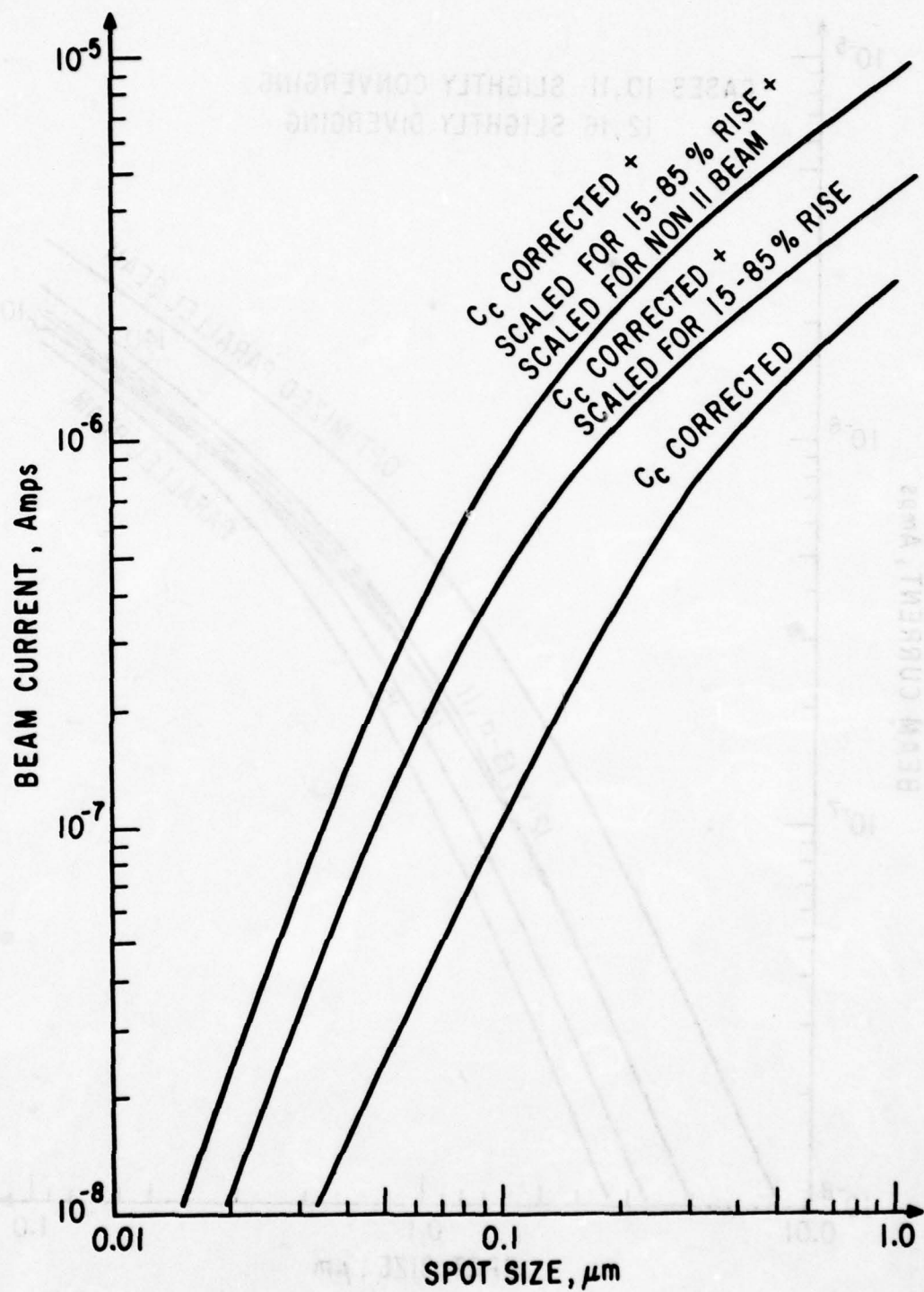
Figure 62. Beam Current Vs. Spot Size
Two Electrostatic Lenses
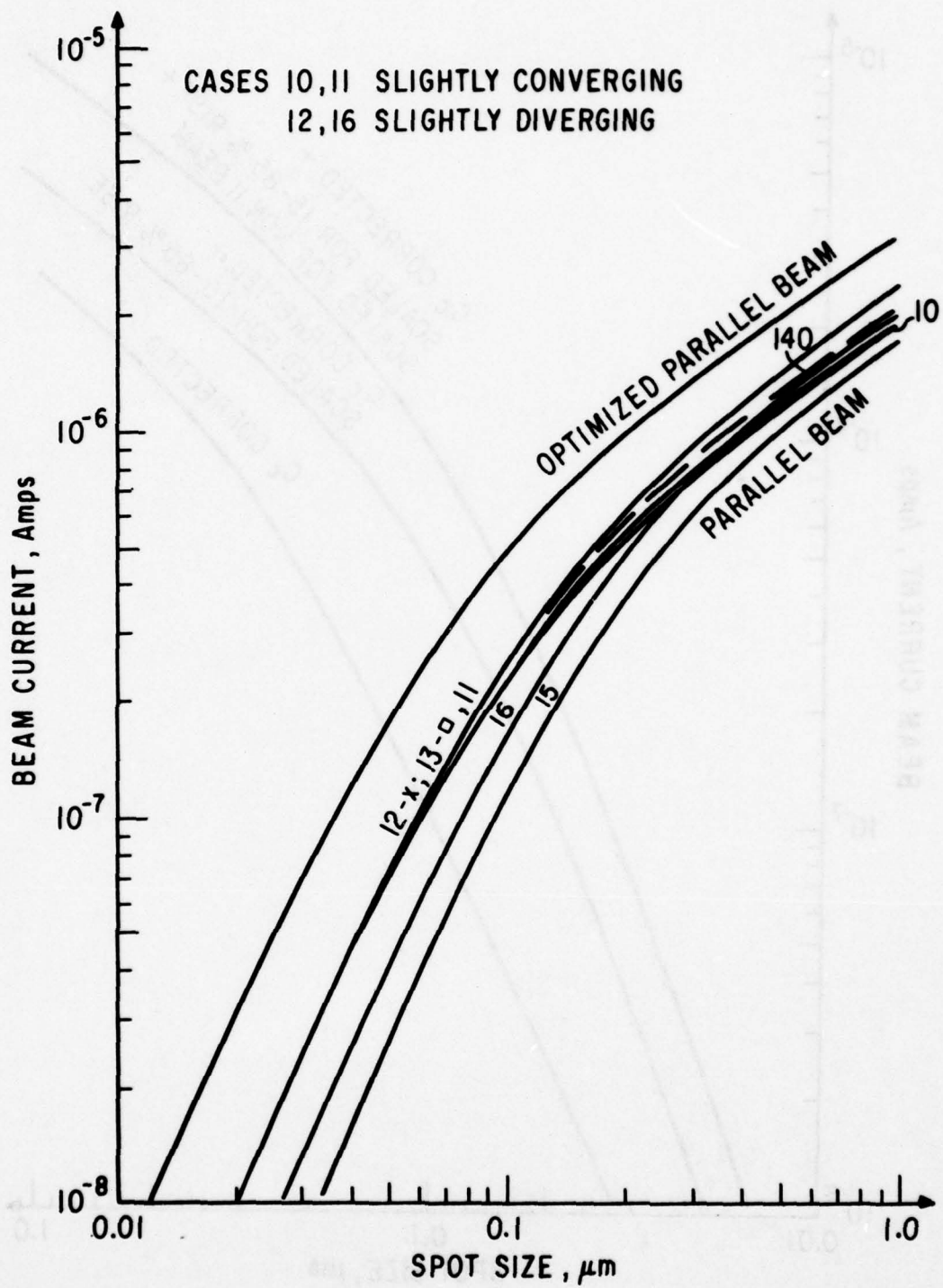
Figure 63.   Beam Current vs Spot Size Calculated for ETEC Probe with Full Corrections to Optics Program

114

shown in Figure 63. The first curve shows the resulting correction due to the factor of two in the chromatic aberration coefficient. The next higher curve shows this factor for C_c along with the scaling for the 15-85% rise time definition of spot size. Finally, the maximum current curve shows 11 of the corrections incorporated; that is, the factor of two in chromatic aberration coefficient, correction for the 15-85% rise time, and finally the scaling of the factor of two for a nonparallel beam operation. As can be seen from this curve, approximately one microamp of current is obtained in a tenth micron spot. This is in excellent agreement with the experimental data previously shown in Figure 59 for the Veneklassen probe.

SUMMARY

During this reporting period negotiations began with ETEC Corporation for a high current, thermionic-aided field emission microprobe. Analytical studies were made in order to better understand the column specifications and performance claims. The first analytical attempts were grossly in error with ETEC's published experimental results. Investigations of these discrepancies showed that they were the result of differences in definitions of spot size, chromatic aberration coefficient, and a different operating mode (i.e., noncollimating between lenses). Once these differences were recognized and incorporated in the analysis, the experimental and calculated beam current versus spot size curves were in excellent agreement. As a result of these calculations we have extended our confidence in the electron optical analytical techniques.

115

Also, we have a clear picture of the specifications, expected performance, and potential for further improvement in the ETEC column. Based on the optics specifications, and the confidence that these will be met or exceeded through the use of the analytical techniques, an order was placed with ETEC for the high current TFE microprobe.

APPENDIX

HOTSPOT3

DESCRIPTION AND USER'S GUIDE

<u>INTRODUCTION</u>

HOTSPOT3 is a finite difference type computer program designed to permit the study of heat production and flow in any solid material in which the assumption of radial symmetry for both the material and temperature distribution is valid. It is physically a three-dimensional solution which has been reduced to two dimensions mathematically by assumption of radial symmetry. In practice, a solid object is 'constructed' of various materials whose relevant properties are described in functions. The initial conditions are described by the user along with the manner in which heat will be added. The program then prints on an output file an array showing the temperature distribution everywhere in the solid object: that is, the temperature of each cell at any future time chosen by the user.

The program described here is written in the BASIC language of the General Electric ISBD time sharing (Mark 3) system.

117

Program Description

1. Mesh Dimensions

Since the problem is solved in cylindrical coordinates, the mesh is shaped accordingly. Thus, the volume of cells at small values of R is smaller than that at large R. The user must decide how many cells are needed for the problem. There are R9 cells in the radial direction and Z9 in the axial direction. These values are set in lines 1200 and 1300 and the dimension statement of line 900 may need changing. The cell lengths are R1 and Z1 in units of (cm) and are set in lines 1600 and 1800 (cm). This version of HOTSPOT is intended to model a substrate with up to two uniform surface layers. The top layer consists of cell row numbers 1 through (Z2-1). The second layer begins with row Z2 and ends with row (Z4-1). The substrate rows are Z4 through Z9. Z2 and Z4 are set in lines 1700 and 1750. It is generally wise to first try a problem with rather a coarse mesh with small R9 and Z9 until the sort of flow pattern and time scale is understood. The cost increases rapidly with these parameters.

2. Image Matrix

The image matrix $I(R,Z)$ is an array corresponding to the cells of the mesh. The elements of $I(R,Z)$ are integers denoting the material each cell is made of. The matrix is formed beginning on line 3000.

118

3. Power Input

The total input power, P, is set in line 1100. P is given as a function of EO, the beam energy in kilovolts, with a one micro-ampere beam current assumed. This may be changed at the discretion of the user. The only remaining parameter left to the user is the beam radius (Gaussian width at the surface), Al, set in line 1030. Even though the beam power function is defined in absolute terms, the result is renormalized so that the sum of the blocks of power supplied to all the cells is equal to the specified input power. The power density function FNP(R,Z) is formed beginning at line 12900.

4. Time Scale

Each time increment must be chosen small enough so that only a relatively small change occurs in the temperature of the cells or the program will not give correct results. This minimum time interval Tl is set in line 2100 and its optimal value depends on the physical size of the volume being heated and the thermal con-ductivity of the materials. The way the program operates is to form an increment cell matrix D(R,Z) whose elements consist of the net temperature change for each cell that occurs during a time Tl based on its temperature and that of its neighbors. This matrix is then added to the temperature matrix U(R,Z). This process con-tinues until a time T9 (set in line 2000) is reached when the ma-trix U(R,Z) is stored on an output file with suitable headings.

119

The program will then ask for a new value of 'T MAX' (T9) and if given it, will proceed as before. If it is desired to stop the calculation but retain the option of continuing later, respond with a carriage return and all of the data will be saved in the file 'HEAT2'. To continue, copy 'HEAT2' into the input file 'HEAT1' and RUN. If for any reason you do not wish to have HEAT2 altered at the conclusion of a run, type 'S' and the program will stop. At each stop, the results at that time (T9) will be printed in the output file 'HEATOUT'. This file is always appended (never destroyed) by the program. When run, the program first asks 'NEW OR OLD?'. If the answer is 'NEW', it will start with a clean slate from time T=0. Otherwise it will read 'HEAT1' and use those data for starting conditions.

5. *Boundary Conditions*

As the program stands at present, all of the outermost side and bottom cells are maintained at the substrate temperature (set in line 5200) which is also the initial temperature when a 'NEW' case is run. These are all cells with R=R9 or Z=Z9. At present, the Z=1 cells are not influenced by the outside environment (except, of course, by the input power function). Provision is made, however, to allow heat to flow in or out of the top surface (e.g., radiation) in line 8400.

120

6. Volume Specific Heat

The volume specific heat function FNC(T,I) allows a temperature dependent specific heat. I is the material index for a particular material specified originally in the image matrix. Each cell of the mesh is assigned a number which specifies the material the cell volume is made of (see Image Matrix).

7. Thermal Conductivity

This function FNK(T,I) is defined following line 16500. Again, provision is made for temperature dependence.

8. Density

The material density is used in defining electron range in materials when one is constructing the power input function. This function FNR(I) is a table of values whose definition begins in line 19600.

9. Material Label

This is a string function FNL$(I) that returns the name of the material designated by the index number I. Its use is for automatic printouts of materials used in each calculation.

121

10. Output

The output to the file HEATOUT begins with the writing of
the temperature matrix U(R,Z) as it would appear after a time T1
in the absence of heat flow. This is useful to help visualize
the effect of the pattern of input power. Just preceding this,
and in every printing of U(R,Z), is a set of headings written by
lines 9300-10000 and alterable at the discretion of the user.
The first of these lines prints the comment string C$ defined in
line 800. The others help identify the case being run.

In addition to the output file, there is output to the ter-
minal which is useful for observing progress as time increases.
This printout is due to lines 10900-11500 and at present is part
of the first row and column of U(R,Z); enough to guide selection
of time intervals without taking excessive time at a slow termi-
nal. These lines are also alterable according to the wishes of
the user.

HOTSPOT3 USER'S GUIDE

1. Preliminaries

The first step is to set the values of the various parameters
in the program to match the case being run. For most parameters
this is simple, but a few are tricky. The most difficult is T1,

122

the time of one iteration. It appears from our studies that one
should use the largest possible value of T1 for which the process
is stable. Use of a smaller value does not substantially change
the result. A good first try would be about 1% of the cell area
divided by the diffusivity although this can vary widely with the
geometry of the problem. It is our practice to first estimate
T1 in the manner described, setting T9 to ten times this value,
and then run the program. If the process is unstable as evidenced
by wild oscillations in the cell temperatures, reduce T1 by half.
Otherwise double it, repeating this procedure until the largest
stable value is found. Decreasing the cell size R1 and Z1 gener-
ally requires decreasing T1. It is recommended that the cell size
be made as large as reasonable at least for preliminary runs.
It is necessary, however, that each separate material layer have
at least two cell rows. The following is an alphabetic listing
of all of the simple parameters which would normally be changed
by the user (with line number):

A1 (1030) Beam Radius (cm)

E0 (1010) Beam Energy (kilovolts)

P (1100) Beam Power Input (watts)

R1 (1600) Radial Cell Dimension (cm)

R9 (1200) Number of Cells in the Radial Direction

R9 (900) Check DIM of V,M,U,P,D,I

T1 (2100) Time of One Iteration (sec)

T9 (2000) Time of First Program Stop (sec)

Z1 (1800) Axial Cell Dimension (cm)

Z2 (1700) Index # of First Row of Second Layer

Z4 (1750) Index # of First Row of Substrate

Z9 (1300) Number of Cells in the Axial Direction

Z9 (900) Check DIM of V,U,P,D,I

Next, the image matrix I(R,Z) must be constructed to agree with the configuration being modelled. At present, the program has a knowledge of 7 materials. To discover what number corresponds to a given material, read the function subprogram for the label function, FNL$(I), beginning on line 18500. If the desired material is not listed, it will be necessary to add it as described below. If the program is to be used with only one layer over the substrate, give the middle layer the number of the substrate or delete line 3720.

Line 3300: defines top layer material #

Line 3720 defines middle layer material #

Line 3600 defines substrate material #

The string C$ defined in line 800 is an identifying comment which will be printed with the output.

When it becomes necessary to add a new material, change a material, or vary the data for an existing material. The material

related function subprograms must be changed. The arguments T and I are temperature and material number. The four functions are:

FNC(T,I) (14600) Volume specific heat (joules/cc-deg K)

FNK(T,I) (16600) Thermal conductivity (watts/cm-deg K)

FNL$(I) (18500) Name of material

FNR(I) (19700) Density (gm/cc)

2. Program Output

As discussed earlier, the program writes results on the file HEATOUT as well as the terminal. An enormous quantity of information is calculated but usually only a limited amount is preserved. The full array of temperatures is calculated at each interval of time, T1. This is the principal output of the program and gives the temperature of each cell at that time. The two rows of temperatures printed below the array are the temperatures at the interface of each of the layers. In alloy studies, these are the most important results. It is up to the user to decide at which times the temperature array should be recorded. The first record is made at time T9 set by the user. After that, the program will ask for the next time that a temperature record should be made (NEW T MAX?). Even if only a 'final' temperature is desired, it is useful to plot temperature as a function of time to verify that a near final temperature has been reached. Normally, frequent

125

stops should be made. It is the last opportunity to obtain these data.

3. Operation

The effective use of the data storage files HEAT2 and HEAT1 requires some thought. At every stopping point, all current data are written into the file HEAT2 unless the character 'S' is used as a response to a request for the next time (NEW T MAX?). The purpose of this feature is to permit recovery of data in the event that, after a long calculation, the time interval T1 should need to be shortened (as occasionally happens). If this should happen, the temperature data at that time would be useless and typing 'S' would prevent the destruction of the previously stored data. The program would then stop permitting a change in the value of T1 and could then be run again. At this running, the word 'OLD' should be typed in response to 'NEW OR OLD?'. The last leg of the calculation will be repeated using the new value of T1. In the event of a normal termination, the final data will be stored in HEAT2 where it may be used to extend the calculation or it may be stored under a different name for possible future use. Remember, as discussed earlier, the contents of HEAT2 must be moved to HEAT1 to be used. HEAT2 is always an output file and HEAT1 is always an input file.

126

The following is a listing of the program.

```
10 '    P.GRAY/HOTSPOT3

20 '

30 '    SPECIAL VERSION OF HOTSPOT.  FIXED R1,Z1, TWO UNIFORM FILMS

40 '    ON SUBSTRATE.  COMPLETE ELECTRON BEAM ALGORITHM BUILT IN.

50 '    FOR INFORMATION CALL

60 '    PETER V GRAY

70 '    8*235 8369        OR     (518) 385 8369

80 '

100 CALL WARN(0)

300 FILES HEATOUT

400 APPEND#1

500 MARGIN#1,124

600 FILES HEAT1:HEAT2

700 RESTORE#2

800 C$="COMMENT LINE"

900 DIM V(15,15),W(15,2),U(15,15),P(15,15),D(15,15),I(15,15)

910 DIM L(20)

1010 E0=4   'BEAM KILOVOLTS

1020 F1=1   'FLAG FOR FNP

1030 A1=500E-8   'BEAM RADIUS

1100 P=E0*1E-3

1200 R9=15

1300 Z9=15

1400 R9=R9-1

1500 Z9=Z9-1
```

```
1600 R1=200E-8

1700 Z2=4

1750 Z4=6

1800 Z1=200E-8

1900 T=0

2000 T9=2.5E-11

2100 T1=2E-12

2200 PRINT"NEW OR OLD";

2300 INPUTAS

2400 IFAS="NEW"THEN3000

2600 MATREAD#2,U,P,D,I

2700 READ#2,T

2750 READ#2,CS

2800 GOTO11700

2900 '

3000 'FORM IMAGE MATRIX

3100 FORR=1TOR9+1

3200 FORZ=1TOZ2-1

3300 I(R,Z)=6        'TOP LAYER

3400 NEXTZ

3500 FORZ=Z2TOZ9+1

3600 I(R,Z)=1        'SUBSTRATE

3700 NEXTZ

3710 FORZ=Z2TOZ4-1

3720 I(R,Z)=7        'MIDDLE LAYER
```

128

```
3730 NEXTZ

3800 NEXTR

3900 '

4000 'FORM POWER DENSITY MATRIX

4100 P1=0

4200 FORR=1TOR9

4300 FORZ=1TOZ9

4400 P(R,Z)=FNP((R-.5)*R1,(Z-.5)*Z1)

4500 P1=P1+P(R,Z)*3.1416*Z1*R1*R1*(2*R-1)

4600 NEXTZ

4700 NEXTR

4800 MATP=(P/P1)*P

4850 PRINT"P1="P1

4860 PRINTCS

4864 PRINT"A"(Z2-1)*Z1*1E8;"ANGSTROM ";FNLS(I(1,1));" FILM ON ";

4868 IF I(1,Z2)=I(1,Z9+1) THEN4880

4872 PRINT

4876 PRINT"A"(Z4-Z2)*Z1*1E8;"ANGSTROM ";FNLS(I(1,Z2));" FILM ON ";

4880 PRINTFNLS(I(1,Z9+1));" SUBSTRATE."

4884 PRINT"TIME="T

4888 PRINT"EO="EO"KV,  POWER="P"WATTS"

4892 PRINT"BEAM RADIUS="A1"CM"

4896 PRINT"VOL SP HEAT="FNC(T,I(1,1));FNC(T,I(1,Z2));

4897 PRINTFNC(T,I(1,Z9+1))

4900 PRINT"TH COND="FNK(T,I(1,1));FNK(T,I(1,Z2));FNK(T,I(1,Z9+1))
```

```
4904 PRINT"DR=";R1;"DZ=";Z1
4903 PRINT
5000 'THERMAL BIAS
5100 MATU=CON
5200 MATU=(300)*U
5300 '
5400 'FIRST POWER TO U(R,Z)
5500 FORR=1TOR9
5600 FORZ=1TOZ9
5700 U(R,Z)=U(R,Z)+T1*P(R,Z)/FNC(U(R,Z),I(R,Z))
5800 NEXTZ
5900 NEXTR
6000 PRINT#1,"HEAT ADDED DURING FIRST";T1;"SECONDS"
6100 PRINT"HEAT ADDED DURING";T1"SEC"
6200 GOTO9300
6300 T=T1
6400 '
6500 'FORM INCREMENT MATRIX D(R,Z) INCLUDE FLOW AND POWER
6600 FORR=1TOR9
6700 FORZ=1TOZ9
6800 U=U(R,Z)
6900 M=I(R,Z)
7000 K=FNK(U,M)
7100 C=FNC(U,M)
7200 A2=K/C
```

130

```
7300 D=T1*F(R,Z)/C
7400 IFR=1THEN7700
7500 D=D+A2*T1*((R-1)*U(R-1,Z)-(2*R-1)*U+R*U(R+1,Z))/((R-.5)*R1*R1)
7600 GOTO7900
7700 'R=1 CASE
7800 D=D+A2*T1*2*(U(2,Z)-U)/(R1*R1)
7900 IFZ=1THEN8200
7910 IFI(R,Z)<>I(R,Z+1)THEN8020
7920 IFI(R,Z)<>I(R,Z-1)THEN8040
8000 D=D+A2*T1*(U(R,Z-1)-2*U+U(R,Z+1))/(Z1*Z1)
8010 GOTO8500
8020 D=D+A2*T1*(U(R,Z-1)-2*U+V(R,Z+1))/(Z1*Z1)
8030 GOTO8500
8040 D=D+A2*T1*(V(R,Z-1)-2*U+U(R,Z+1))/(Z1*Z1)
8100 GOTO8500
8200 'Z=1 CASE--CONSIDER RADIATION LOSS
8300 D=D+A2*T1*(U(R,2)-U)/(Z1*Z1)
8400 'D=D+RADIATION LOSS
8500 F(R,Z)=D
8600 NEXTZ
8700 NEXTR
8800 '
8900 T=T+T1
9000 MATU=U+D
9005 'FORM MIRROR MATRIX
```

```
9010 FORR=1TOR9
9015 K1=FNK(U(R,Z2-1),I(R,Z2-1))
9020 K2=FNK(U(R,Z2),I(R,Z2))
9025 U1=U(R,Z2-1)
9030 U2=U(R,Z2)
9035 M(R,1)=(U1*K1+U2*K2)/(K1+K2)
9040 V(R,Z2-1)=2*M(R,1)-U2
9042 V(R,Z2)=2*M(R,1)-U1
9055 K1=FNK(U(R,Z4-1),I(R,Z4-1))
9060 K2=FNK(U(R,Z4),I(R,Z4))
9065 U1=U(R,Z4-1)
9070 U2=U(R,Z4)
9075 M(R,2)=(U1*K1+U2*K2)/(K1+K2)
9080 V(R,Z4-1)=2*M(R,2)-U2
9085 V(R,Z4)=2*M(R,2)-U1
9090 NEXTR
9095 IFT=0THEN6300
9100 '
9200 IFT<T9-T1/2THEN6500
9300 PRINT#1,C$
9400 PRINT#1,"A"(Z2-1)*Z1*1E8;"ANGSTROM ";FNL$(I(1,1));" FILM ON ";
9420 IF I(1,Z2)=I(1,Z9+1) THEN9460
9440 PRINT#1,
9450 PRINT#1,"A"(Z4-Z2)*Z1*1E8;"ANGSTROM ";FNL$(I(1,Z2));
9451 PRINT#1," FILM ON ";
```

```
9400 PRINT#1,FNLS(I(1,Z9+1));" SUBSTRATE."

9500 PRINT#1,"TIME="T

9600 PRINT#1,"EO="EO"KV,   POWER="P"WATTS"

9650 PRINT#1,"BEAM RADIUS="A1"CM"

9700 PRINT#1,"VOL SP HEAT="FNC(T,I(1,1));FNC(T,I(1,Z2));

9701 PRINT#1,FNC(T,I(1,Z9+1))

9800 PRINT#1,"TH COND="FNK(T,I(1,1));FNK(T,I(1,Z2));

9801 PRINT#1,FNK(T,I(1,Z9+1))

9900 PRINT#1,"DR="R1;"DZ="Z1

10000 PRINT#1,

10100 FORZ=1TOZ9

10200 FORR=1TOR9

10300 PRINT#1,TAB(8*(R-1));STR$(U(R,Z));

10400 NEXTR

10500 PRINT#1,

10600 NEXTZ

10700 PRINT#1,

10710 FORZ=1TOZ2

10720 FORR=1TOR9

10730 PRINT#1,TAB(8*(R-1));STR$(M(R,Z));

10740 NEXTR

10750 PRINT#1,

10760 NEXTZ

10770 PRINT#1,

10800 PRINT#1,
```

133

```
10900 FORR=1TOR9

11000 PRINTU(R,1);

11100 NEXTR

11200 PRINT

11300 FORZ=2TOZ9

11400 PRINTU(1,Z)

11500 NEXTZ

11510 PRINT"BOUNDRY TEMPERATURES="M(1,1);M(1,2)

11600 IFT=0THEN9005

11700 PRINT"T="T;", NEW T MAX";

11800 MATINPUT TS

12000 IFTS(1)="S"THEN12700

12300 SCRATCH#3

12500 MAT WRITE #3,U;P;D;I;

12600 WRITE#3,T

12650 WRITE#3,CS

12660 IFNUM=0THEN12700

12670 T9=VAL(TS(1))

12680 GOTO6500

12700 STOP

12800 '

12900 'POWER DENSITY FUNCTION (UNNORMALIZED)

13000 DEFFNP(X,Y)     'WATTS/CC

13010 'VERTICAL FUNCTION

13015 IF F1=0THEN13090
```

```
13020 'FIRST TIME THROUGH
13030 FORI=0TO13
13040 READ L(I)
13050 DATA .75,1.05,1.27,1.4,1.4,1.31,1.08,.82,.55,.32,
13051 DATA .18,.08,.02,0
13060 NEXTI
13070 Z3=(Z2-1)*Z1    'METAL THICKNESS
13080 Z0=Z3*(FNR(I(1,1))/FNR(I(1,Z2))-1) 'DISPLACEMENT OF ORIGIN
13082 Z5=Z0+Z3+(Z4-Z2)*Z1
13084 Z6=Z5*(FNR(I(1,Z2))/FNR(I(1,Z9))-1)
13085 F1=0   'RESET FLAG
13090 'EVERY TIME THROUGH
13095 A=A1+Y*TAN(3.14159*30/180)   'WIDTH AT I/E POINT
13100 IFY<Z3THEN13120
13110 Y=Y+Z0   'FORM EFFECTIVE Y
13112 IFY-Z0<(Z4-1)*Z1THEN13120   'MIDDLE LAYER CASE
13114 Y=Y+Z6                       'SUBSTRATE DISPLACEMENT
13120 R0=E0^1.75*4E-6/FNR(I(R,Z))    'GRUN RANGE
13125 Y=Y/R0
13130 L=0
13140 IFY>=1.3THEN13180
13150 Y1=INT(10*Y)
13160 Y2=10*Y-Y1
13170 L=L(Y1)+Y2*(L(Y1+1)-L(Y1))
13180 V=L*E0*1E-3/R0  'VERTICAL PART
```

135

```
13190  'HORIZONTAL FUNCTION

13210  H=EXP(-X*X/(A*A))/(A*A*3.14159)

13220  FNP=H*V

13230  FNEND

14400  '

14500  'VOLUME SPECIFIC HEAT

14600  DEFFNC(T,M)    'JOULES/CC-DEG K

14700  IFM=1THEN15100'SI

14800  IFM=2THEN15400'GE

14900  IFM=3THEN15700'AL

15000  IFM=4THEN16000'AU

15010  IFM=5THEN16210'TE

15020  IFM=6THEN16225  'SELENIUM

15030  IFM=7THEN16240  'SI02

15100  'SILICON

15200  FNC=1.63

15300  GOTO16300

15400  'GERMANIUM

15500  FNC=1.65

15600  GOTO16300

15700  'ALUMINUM

15800  FNC=2.43

15900  GOTO16300

16000  'GOLD

16100  FNC=2.5
```

```
16200 GOTO16300
16210 'TELLURIUM
16216 FNC=2.39
16220 GOTO16300
16225 'SELENIUM
16230 FNC=.941
16235 GOTO16300
16240 'SIO2
16244 FNC=1.63
16250 GOTO16300
16300 FNEND
16400 '
16500 'THERMAL CONDUCTIVITY
16600 DEFFNK(T,M)   'WATTS/CM-DEG K
16700 IFM=1THEN17100'SI
16800 IFM=2THEN17400'GE
16900 IFM=3THEN17700'AL
17000 IFM=4THEN18000'AU=3.0
17010 IFM=5THEN18210   'TE
17020 IFM=6THEN18225   'SE
17030 IFM=7THEN18240   'SIO2
17100 'SILICON
17200 FNK=.83
17300 GOTO18300
17400 'GERMANIUM
```

```
17500 FNK=.64
17600 GOTO18300
17700 'ALUMINUM
17800 FNK=.48
17900 GOTO18300
18000 'GOLD
18100 FNK=3
18200 GOTO18300
18210 'TELLURIUM
18215 FNK=.06
18220 GOTO18300
18225 'SELENIUM
18230 FNK=.005
18235 GOTO18300
18240 'SIO2
18245 FNK=.015
18250 GOTO18300
18300 FNEND
18400 'MATERIAL LABEL
18500 IEFFNLS(I)
18600 ON I GOTO 18700,18900,19100,19300,19410,19420,19430
18700 FNLS="SILICON"
18800 GOTO19500
18900 FNLS="GERMANIUM"
19000 GOTO19500
```

138

```
19100 FNLS="ALUMINUM"

19200 GOTO19500

19300 FNLS="GOLD"

19400 GOTO19500

19410 FNLS="TELLURIUM"

19415 GOTO19500

19420 FNLS="SELENIUM"

19425 GOTO19500

19430 FNLS="SILICON DIOXIDE"

19435 GOTO19500

19500 FNEND

19600 'DENSITY FUNCTION

19700 DEFFNR(I)    'GM/CC

19800 ON I GOTO 19900,20100,20300,20500,20610,20620,20630

19900 FNR=2.42    'SI

20000 GOTO20700

20100 FNR=5.36    'GE

20200 GOTO20700

20300 FNR=2.699   'AL

20400 GOTO20700

20500 FNR=19.32   'AU

20600 GOTO20700

20610 FNR=6.24   'TE

20615 GOTO20700

20620 FNR=4.79   'SE
```

```
20625 GOTO20700
20630 FNR=2.20  'SIO2
20635 GOTO20700
20700 FNEND
20800 END
```

REFERENCES

1. S.K. Ghandi, *The Theory and Practice of Microelectronics*, John Wiley and Sons, Inc., New York, New York, 1968.

2. *Advanced Archival Memory* 1st Quarterly Report, April 15, 1976-July 15, 1976, AFAL-TR-76-213 under Contract Number F33615-76-C-1322.

3. *Advanced Archival Memory* 3rd Quarterly Report, October 16, 1976-January 15, 1977, in Press, under Contract Number F33615-76-C-1322.

4. V.E. Coslett and R.N. Thomas, *Brit. Journal of Applied Physics*, Vol. 15, p. 1283, 1964.

5. M.A. Omar, *Elementary Solid State Physics*, Addison Wesley Publishing Company, 1975.

6. Masaaki Kuriyama, "Thermal Conductivities of As-Se Glasses," pp. 302-3, 1975.

7. I.A. Rozov, A.F. Chudnovskii, and V.F. Kokorina, *Sov. Phys. Semicond.* 1, p. 969, 1968.

8. Richard Flasck and Howard K. Rockstad, "The Thermal Conductivity of Some Chalcogenide Glasses," *J. of Non-Crystalline Solids*, 12, pp. 353-6, 1973.

9. B.T. Kolomiets, L. Payasova, and L. Stourac, Sov. Phys. -Solid State 7, p. 1285.

10. L. Stourac, B.T. Kolomiets, and V.P. Silo, Czech. J. Phys. B18, p. 92, 1968.

11. M.D. Tabak and W.J. Hillegas, "Preparation and Transport Properties of Vacuum Evaporated Selenium Films," *J. Vac. Science and Technology* 9, pp. 387-90, 1972.

12. A.G. Sigai, "Open Boat Evaporation of Low Arsenic-Selenium Alloys," *J. Vac. Sci. and Tech.*, 12, pp. 753-77, 1975.

13. John C. Schottmiller, "Structure-Property Relationships in Xerographic Selenium-Alloy Films," *J. Vac. Sci. and Technol.*, 12, pp. 807-10, 1975.

14. H.P.D. Lanyon, "Crystallization and Viscosity of Vitreous Selenium," in Int'l Symp. on The Physics of Selenium and Tellurium, ed. W. Charles Cooper, Pergamon Press 1969.

15. A.L. Renninger and B.L. Averbach, "Atomic and Radial Distribution Functions of As-Se Glasses," Phys. Rev. B8, pp. 1507-14, 1973.

141

16.	M. Cukierman and D.R. Uhlmann, "Viscous Flow Behavior of Selenium," J. Non-Cry. Solids, 12, pp. 199-206, 1973.

17.	R.A. Fortland, J. Appl. Phys., 35, p. 1558, 1960.

18.	J. Neyhart, Phot. Sci. Eng. 10, p. 126, 1966.

19.	M.B.I. Janjua, J.M. Toguri, and W.C. Cooper, Can. J. Phys., 49, p. 475, 1971.

20.	W. Charles Cooper and R.A. Westbury, "The Structure of Selenium," in Selenium, ed. Ralph A. Zingaro and W. Charles Cooper, Van Nostrand Reinhold Co., New York 1974.

21.	Handbook of Military Infrared Technology, ed. William L. Wolfe, US Government Printing Office p. 331, 1965.

22.	Thermophysical Properties of Matter, Vol. 1, Y.S. Touloukian, Cy. Ho. eds. - IFI/Plenum, N.Y. 1970.

23.	CRC Handbook of Chemistry and Physics, 48 Edition (Chemical Rubber Co., Cleveland, Ohio), 1967.

24.	Handbook of Tables for Applied Engineering Science, Chemical Rubber Co., Cleveland, Ohio.

25.	H.E. Bishop, "Some Electron Backscattering Measurements for Solid Targets," X-Ray Optics and Microanalysis IV Congress, ed. R. Castaing, P. Deschamps, J. Philibert, Orsay Sept. 1965. HERMANN Paris pp. 153-58, 1966.

26.	P. Palluel, Compt. rend. 224, p. 1492, 1947.

27.	Ernest J. Sternglass, "Backscattering of Kilovolt Electrons from Solids," Phys. Rev. 95, pp. 345-58, 1954.

28.	Joseph F. Dettorre, Thomas G. Knorr and Elton H. Hall, "Evaporation Process," in Vapor Deposition, ed. Carrol F. Powell, Joseph H. Oxley and John M. Blocher, Jr., John Wiley and Sons, pp. 62-101, 1966.

29.	Raymond J. Ackermann, Robert J. Thorn and George H. Winslow, "Some Fundamental Aspects of Vaporization," in The Characterization of High-Temperature Vapors, ed. John L. Margrave, John Wiley and Sons, pp. 427-452, 1967.

30.	IBID Appendix A by Richard E. Honig, pp. 475-494.

31.	Janjua, M.B.I., Toguri, J.M., and Cooper, W.C., Can. J. Phys. 49, 475, 1971.

32.	Saul Dushman, Scientific Foundations of Vacuum Technique, 2nd Edition John W. Wiley and Sons, p. 740, 1972.

33. A.H. Goldenberg, "A Problem in Radial Heat Flow," _Brit. J. Appl. Physics_, _2_, pp. 233-37, 1951.

34. G.E. Possin, "Bit Packing Density of the BEAMOS Target," _JAP_ _48_, pp. 5245-61, 1977.

35. T.E. Everhart and P.F. Hoff, "Determination of Kilovolt Electron Energy Dissipation vs. Penetration Distance in Solid Materials," _J. Appl. Phys._ _42_, pp. 5837-5846, 1971.

36. J.W. Wolfe, G.E. Ledges, H.H. Glascock, U.S. Patent No. 3,760,385, September 18, 1973.

37. J.E. Wolfe, _J. Vac. Sci. Technol._, Vol. _12_, No. 6, Nov./Dec., 1975.

38. L. Veneklasen, N. Yew, and J. Wiesner; Proceedings of the 8th International Conference on Electron and Ion Beam Science and Technology, Seattle, Washington, May 1978.

39. L.H. Veneklasen and B.M. Siegel, _J. Appl. Phys._, Vol. _43_, No. 4, April 1972.

143